Picosecond acoustics in giant magnetostrictive Galfenol

Dissertation

presented to the Faculty of Physics of the
TU Dortmund University, Germany,
in partial fulfillment of the requirements
for the degree of

Doktor rer. nat.

by
Jasmin Viktoria Jäger

technische universität
dortmund

Dortmund, May 2015

Accepted by the Faculty of Physics of the TU Dortmund University, Germany.

Day of the oral examination: 10th December 2015

Examination board:
Prof. Dr. Manfred Bayer
Prof. Dr. Metin Tolan
Prof. Dr. Kevin Kröninger
Dr. Bärbel Siegmann

Contents

1 Motivation

The work in hand is dedicated to the experimental studies on the magnetization dynamics induced by picosecond strain pulses in ferromagnetic Galfenol. It is the first attempt to investigate the dynamical magnetic properties of this novel functional material considered as a prospective candidate for nanoscale applications.
The interest in magnetism dates back to ancient civilizations. Starting with the discovery of magnetized magnetite, a natural iron oxide attracting small pieces of iron more than 10.000 years ago, the various applications of magnetism in science and everyday life increased rapidly. Magnetic materials are nowadays widely used in navigation, medical science or technical data storage and sensing and actuating devices [1, 2]. Popular representatives of data storage technology are magnetic memory disks and magnetic shape memory alloys [3]. During technological progress in the last decade operation standards and fabrication of mechanical compounds increased. Instead, efficient operation- and recording speed bear a great challenge so far. To cope with this increased rate of technological progress providing new technical achievements on a nearly monthly basis requires the frequent and fundamental research of new materials and improved methods operating at ultrafast timescales. The focus in the research field of magnetic materials is thus, drawn to ultrafast magnetization control.
A very recently developed ferromagnetic alloy of iron and gallium called Galfenol provides excellent and very specific magnetic properties [4]. The structure possesses giant magnetostrictive parameters at low saturation fields and a Curie temperature exceeding 600 °C. Future applications of Galfenol may focus on sensor and actuator technology for example in automobile industries [5]. In contrast to other giant magnetostrictive materials, Galfenol features also outstanding practical advantages. In contrast to the giant magnetostrictive Terfenol-D, the compound of Terbium, Iron and Dysprosium [6, 7], Galfenol does not contain any rare earth elements and is therefore, technologically accessible. It is not brittle and the structure is easily attached to various substrates. And because of the high Curie temperature Galfenol serves as an ideal candidate for investigations at ambient temperatures.
Classical methods of magnetization modulation include the application of external magnetic fields and microwave radiation but they are limited in frequency and therefore hardly applicable for ultrafast modulation. Thus, alternatives providing ultrafast access to magnetization dynamics are required. Recent studies include the perturbation of magnetization in metal, semiconductor and dielectric ferromagnetic materials via ultrashort light pulses [8, 9, 10, 11, 12] and external electrical fields [13]. An al-

ternative non-destructive method is the picosecond acoustics technique which is used to generate ultrafast strain pulses that couple to magnetic excitations in ferromagnetic thin films. The concept of picosecond acoustics comprehends the generation of ultrashort strain pulses containing coherent acoustic phonon wave packages [14]. Acoustic strain pulses cover a broad frequency range up to THz frequencies and high amplitudes reaching 10^{-3} at spatial extension up to 100 nm. It is nowadays widely used as a prodigious source to analyze structural properties and physical processes in various materials [15, 16, 17]. The concept of ultrafast acoustics is non-destructive [15] since the material is not heated and there is no modification of the material's electronic properties. A variety of applications of this technique includes resonant control of the emission of microcavity laser systems [18, 19], high frequency modulation of surface plasmon-polariton resonances in plasmonic nanodevices [20] and exciton resonances in semiconductor quantum wells [21]. Moreover, picosecond strain induced magnetization rotation in the Mn-doped semiconductor GaAs and Ni films has been realized [22, 23, 24]. Therein, strain pulses perturb the magnetic anisotropy of the sample layer. This leads to a tilt of the magnetization out of its equilibrium orientation resulting in a precessional motion of the layer magnetization. It is expected that this method is much more effective in Galfenol due to its outstanding properties. This work is aimed at examining this assumption.

This work is organized as follows: Chapter 2 introduces the structure and characteristic features of Galfenol. A brief overview of essential magnetostriction and magnetic anisotropy parameters is given, providing the basis for all physical processes studied in this material.
Chapter 3 is dedicated to the basics of picosecond acoustics. Ultrafast acoustic strain pulses induced by femtosecond optical laser pulses are used as the tool to excite magnetization modulation of the ferromagnetic layer in this study. Starting from the theory of elasticity describing elastic wave propagation in solids this chapter provides a condensed overview of the conversion of optical energy into longitudinal acoustic strain in a metal transducer. The strain pulse propagation through solid media is discussed in the linear and anharmonic regime including the formation of solitons.
The experimental realization of strain induced magnetization modulation in Galfenol is the topic of chapter 4. First, the experimental concept will be discussed on a general phenomenological basis. The experimental realization follows in a second part of this chapter, introducing the required laser systems and sample environment integrated in a time-resolved pump-probe setup. Precession signals are monitored by means of the polar magneto-optical Kerr effect which is explained in the last section. Former experiments in ferromagnetic semiconductors stated the enhancement of magnetization tilt using shear strain instead of longitudinal strain [23]. Therefore, high index semiconductor substrates are used to inject different quasi-longitudinal and quasi-transverse strain pulses. Before the presentation of magnetization experiments, the different propagation modes are studied in a [311]-GaAs substrate in chapter 5.

The magnetization precession dynamics induced by acoustic strain pulses are compiled in chapter 6. Different samples with high and low crystallographic symmetry are investigated in different geometries regarding the external field. One of the main results is the first observation of magnetization precession at GHz frequencies in Galfenol at low and ambient temperatures.
The last part of this study deals with the resonant driving of the magnetization precession by localized phonons in a Galfenol acoustic nanocavity (chapter 7). The layer is therefore embedded in an acoustic resonator with superlattice structures forming Bragg mirrors for the selective confinement of acoustic cavitiy modes. Magnetization precession frequencies coinciding the resonant cavity frequencies lead to a significant enhancement of the precession dynamics.
A conclusion and outlook to the experimental studies presented in this work is found in the last chapter.

2 Galfenol

The novel ferromagnetic alloy of iron and gallium $Fe_{100-x}Ga_x$ (Galfenol) has been developed at the Naval Surface Warfare Center by Clark et al. in 1998 [25]. It has been created for specific applications in sensor and actuator devices. This material displays typical characteristics attributed to common ferromagnetic materials. A remarkable feature that distinguishes Galfenol from other ferromagnetic materials is the enhanced magnetostriction parameter measured for this material. Magnetostriction defines the coupling of a structure's magnetic properties to elasticity. This relation is enormously enhanced in Galfenol at a specific Ga content. Therefore, Galfenol belongs to the group of giant magnetostrictive materials.
This chapter contains a brief discussion on the main static properties of Galfenol that state the important physical background to the experimental studies on magnetization modulation presented in this work.

2.1 Magnetic anisotropy

Every ferromagnetic material is characterized by a saturation magnetization M_0 and the spontaneous orientation of magnetic moments below the *Curie* temperature T_C. Compared to common ferromagnetic materials, Galfenol yields strong ferromagnetic properties. The saturation magnetization and Curie temperature display very high values of $M_0 = 1,8$ T and $T_C \geq 600$ °C. Below T_C, magnetic properties are characterized by the magnetic anisotropy - the directional dependence of magnetization. A demonstrative example shall illustrate this intrinsic property. A cylindric slab of iron can be magnetized much easier along the direction of its long side than along its plane surface. This contribution to the anisotropy energy of a ferromagnetic structure is called the demagnetization- or shape anisotropy. It relates to the internal demagnetization field, sensitive to the shape of the crystal. The demagnetization field caused by the magnetization reads $\vec{H}_d \propto -N\vec{M}$ with N as the demagnetizing factor determined by the outer shape. In general, a magnetically anisotropic material displays an easy axis (EA) of magnetization meaning an energetically favourable direction of spontaneous magnetization. The direction along which high external magnetic field strength is needed to magnetize the material is called the hard axis (HA) of magnetization. In crystalline structures with an underlying atom lattice the term 'magneto-crystalline anisotropy' (MCA) is more specific, taking into account that the directions of easy and hard magnetization axes strongly correlate with the

crystallographic axes. MCA is an intrinsic material property caused by the spin-orbit coupling [26]. In an early work approaching magneto-crystalline anisotropy in a cubic crystal of iron, magnetization curves measured along different crystallographic axes have been presented, emphasizing the concept of easy and hard magnetization axes [27]. Figure 2.1 presents the measured magnetization along the [100], [110] and

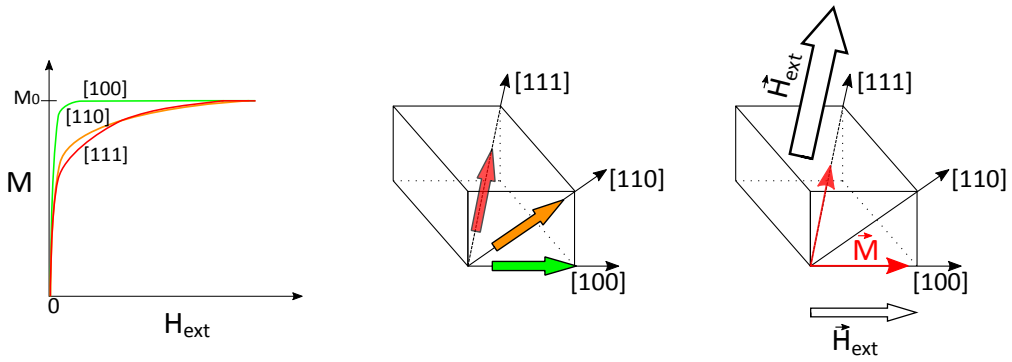

Figure 2.1: Left panel: Magnetization curves of a single cubic crystal of iron dependent on an external magnetic field H_{ext} and on different crystallographic orientations of $\vec{M}$ after [27]. Right panels: Illustration of easy (green), medium (orange) and hard (red) magnetization axes and relative strength of $\vec{H}_{\text{ext}}$ which has to be applied in order to direct the magnetization along the easy (hard) magnetization axis.

[111] crystallographic axes in dependence of the external field H_{ext}. The saturation magnetization M_0 is reached for relatively low values of $\vec{H}_{\text{ext}}$ along the [100] direction. This axis thus, corresponds to the easy axis of magnetization in iron while [110] and [111] display the medium and hard magnetization axes as it is shown in the first right sketch of figure 2.1. The second sketch on the right illustrates that the strongest field is required to align $\vec{M}$ along the [111] crystallographic direction. This demonstration emphasizes one of the contribution to the anisotropy energy of a crystal, the cubic MCA: In this case, the EA coincides with the equivalent main crystallographic axes. The perpendicular or in-plane uniaxial MCA usually describes favourable magnetization orientation along the main symmetry axis of a crystal. All contributions to the anisotropy energy are stated in the free energy density F of a structure. Assuming the layer to consist of a single magnetic domain the free energy density may be expressed as the sum of the Zeeman energy, shape anisotropy and magneto-crystalline anisotropy energies [28]. It is convenient to write F in dependence of the magnetization orientation $\vec{M} = M_0(m_x, m_y, m_z)$ wherein M_0 denotes the saturation magnetization (see figure 2.2 for coordinate axes and orientation of

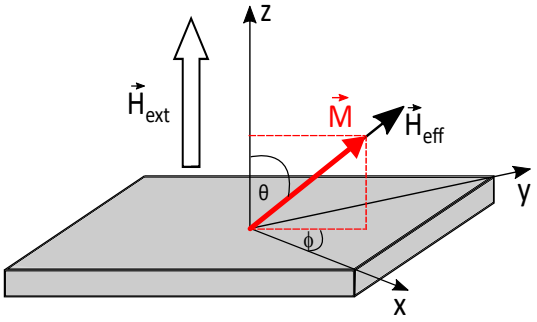

Figure 2.2: Equilibrium position of the effective field $\vec{H}_{\text{eff}}$ governed by the balancing of the external magnetic field $\vec{H}_{\text{ext}}$ and the magnetic anisotropy of the ferromagnetic material. The layer magnetization $\vec{M}$ aligns along the direction of $\vec{H}_{\text{eff}}$.

$\vec{M}$). Thus, the energy landscape of a ferromagnetic thin layer in an external field $\vec{H}_{\text{ext}}$ may be characterized as [29, 30, 31]

$$\begin{aligned} F(m_i, \eta_{ij}) = (-\vec{m} \cdot \mu_0 \vec{H}_{\text{ext}}) + \frac{\mu_0}{2} M_0 m_z^2 + K_c(m_x^4 + m_y^4 + m_z^4) \\ + A_{2\eta}(\eta_{xx} m_x^2 + \eta_{yy} m_y^2 + \eta_{zz} m_z^2) \\ + 2A_{4\eta}(\eta_{xx} m_y^2 m_z^2 + \eta_{yy} m_x^2 m_z^2 + \eta_{zz} m_x^2 m_y^2) \\ + A'_{4\eta}(\eta_{xx} m_x^4 + \eta_{yy} m_y^4 + \eta_{zz} m_z^4) \\ + A_{2xy}(\eta_{xy} m_x m_y + \eta_{xz} m_x m_z + \eta_{yz} m_y m_z). \end{aligned} \tag{2.1}$$

The first two terms describe the Zeeman energy and the shape anisotropy. The third term defines the cubic anisotropy energy with the cubic anisotropy parameter K_c. The remaining contributions contain the uniaxial anisotropy terms dependent on the strain η_{ij} in the material. Any artificial strain is given by the altered spacing of the lattice atoms $\eta_{ij} = \frac{1}{2}(\frac{\partial u_i}{\partial j} + \frac{\partial u_j}{\partial i})$ where $u_{i,j}$ denotes the displacement in $i, j = x, y, z$. The strength of this magneto-elastic anisotropy is characterized by the magneto-elastic anisotropy coupling coefficients $A_{2\eta}$, $A_{4\eta}$, $A'_{4\eta}$ and A_{2xy}. For the Galfenol structure $K_c = -25$ mT indicates the magnetization orientation in-plane in the absence of an external field. The magneto-elastic coefficients read $A_{2\eta} = -9$ T and $A_{2xy} = 5$ T, whereas the values for higher order coefficients $A_{4\eta}$ and $A'_{4\eta}$ are unknown in Galfenol [32].
The derivative of $F(m_i, \eta_{ij})$ with respect to the magnetization orientation is given by an effective field $\vec{H}_{\text{eff}}(m) = \nabla_m F(\vec{M})$. The orientation of $\vec{H}_{\text{eff}}$ is therefore governed by the balancing of $\vec{H}_{\text{ext}}$ and the magnetic anisotropy parameters of the layer. The effective field is "felt" by the layer magnetization which aligns parallel to $\vec{H}_{\text{eff}}$.

The orientations of $\vec{H}_{\text{eff}}$ and $\vec{M}$ of a ferromagnetic layer in case of an external magnetic field applied perpendicular to the layer surface can be withdrawn from figure 2.2. In the absence of any external magnetic field, the favourable orientation of the layer magnetization i.e. the easy axes of magnetization, is determined by minimizing the free energy function of system. Therefore, $\vec{H}_{\text{eff}}$ refers to EA whereas, the hard magnetization axis is associated with the maximum of $F(m_i, \eta_{ij})$. In the spherical coordinate system where the orientations of the external field $\vec{H}$ and the magnetization $\vec{M}$ are specified by the in-plane and out-of-plane angles ϕ and θ as $H(\phi_H, \theta_H)$ and $M(\phi, \theta)$, F states [33]

$$\begin{aligned} F(\phi, \phi_H, \theta, \theta_H) = \frac{1}{2}M[&-2H(\cos\theta\cos\theta_H + \sin\theta\sin\theta_H\cos(\phi - \phi_H)) + 4\pi M\cos^2\theta \\ &- H_{2\perp}\cos^2\theta - \frac{1}{2}H_{4\perp}\cos^4\theta \\ &- \frac{1}{2}H_{4||}\frac{1}{4}(3 + \cos 4\phi)\sin^4\theta - H_{2||}\sin^2\theta\sin^2(\phi - \frac{\pi}{4})]. \end{aligned} \tag{2.2}$$

Again, the first two contributions are the Zeeman term and the shape anisotropy. The magnetic anisotropy parameters are represented by means of the cubic perpendicular and cubic in-plane anisotropy fields $H_{4\perp}$ and $H_{4||}$, the perpendicular uniaxial $H_{2\perp}$ and in-plane uniaxial field $H_{2||}$. They directly relate to the anisotropy energies as $H_4 = \frac{2K_c}{M}$, $H_{2\perp} = 2A_{2\eta}\eta_{zz}$ and $H_{2||} = A_{2xy}\eta_{xy}$.
From both expressions of the energy landscape important magnetic layer properties may be derived. The magnetic anisotropy and therefore the direction of EA (HA) may be changed by the application of external strain to the layer. The modulation efficiency depends on the values of the magneto-elastic coupling constants and magnetostriction parameters of the material.

2.2 Magnetostriction

The interaction of magnetization $\vec{M}$ and the strain η_{ij} contributes to the free energy density of a ferromagnetic thin layer in form of the magneto-elastic anisotropy. Two effects can be characterized as a consequence of this property. The change of shape or dimensions of a ferromagnetic material when subjected to an external magnetic field is known as magnetostriction. J. Joule, first identified the magnetostriction in bulk iron in 1842. Later, the inverse magnetostriction effect or '*Villari* effect' has been discovered by E. Villari in 1862. Inverse magnetostriction characterizes the effect of strain causing a change in the magnetic susceptibility of the ferromagnetic material which is related to a change of the sample magnetization. The magnetostriction coefficient λ is used to characterize the relative change in shape in the direction of an applied external magnetic field written in terms of a change in length l, $\lambda = \Delta l/l$ [34]. The fractional length change attains either positive or negative values. In case

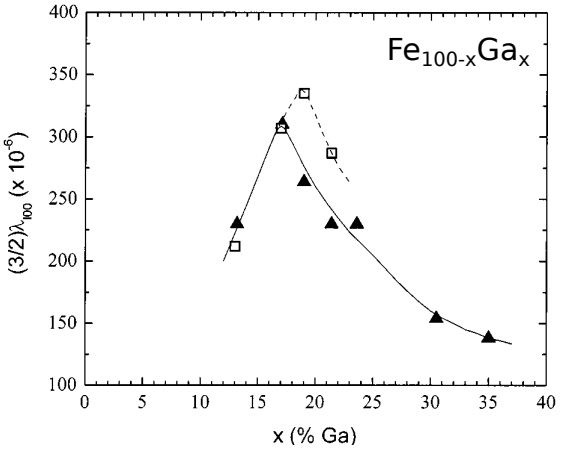

Figure 2.3: (a) Room temperature magnetostriction $3/2\lambda_{100}$ as a function of the Ga content in $Fe_{100-x}Ga_x$ alloys [35]. (Note that the data has been measured from different fabrication types. Squares refer to Galfenol films used in this work, triangles show results from Galfenol samples were the quenching procedure in fabrication has been skipped.)

of $\lambda > 0$, the material expands in the direction of the applied field, while $\lambda < 0$ indicates shrinking. The range of relative extention reaches from $\Delta l/l = 10^{-6}$ to 10^{-2} m/m (alternatively, the unit 'parts per million' (ppm) may be used). The macroscopic effect of magnetostriction originates from microscopic migration of domain wall boundaries and the rotation and re-orientation of domain magnetic moments with respect to an external magnetic field. Both processes change the energy state of the crystal lattice, which is manifested in the change of the equilibrium distances between atomic positions. As a result, the atoms are shifted and magnetostrictive deformation of the lattice takes place. This type of observed magnetostriction is anisotropic, i.e. it depends on the direction and magnitude of the magnetization $\vec{M}$. Thus, λ may be categorized as the saturation values λ_{100}, λ_{010} and λ_{001} of the longitudinal magnetostriction in [100], [010] and [001] direction. The dimensional change of a material with magnetization $\vec{M} = (m_x, m_y, m_z)$ then reads:

$$\begin{aligned}\frac{\Delta l}{l} &= \frac{3}{2}\lambda_{100}(\alpha_x^2 m_x^2 + \alpha_y^2 m_y^2 + \alpha_z^2 m_z^2 - \frac{1}{3}) \\ &\quad + 3\lambda_{111}(\alpha_x\alpha_y m_x m_y + \alpha_x\alpha_z m_x m_z + \alpha_y\alpha_z m_y m_z),\end{aligned} \tag{2.3}$$

with $\vec{\alpha} = (\alpha_x, \alpha_y, \alpha_z)$ displaying the unit vector along the direction in which Δl is measured.
Common magnetostrictive materials include elementary ferromagnetic elements such as Iron (Fe), Nickel (Ni) and Cobalt (Co). Maximum magnetization strains which have been discovered in these materials range from 10 to 20 ppm [4, 36]. Giant

magnetostrictive materials were given their names because of their characteristic enhanced magnetostriction. The compound of Terbium and Dysprosium Terfenol-D displays the highest magnetostriction of $\lambda > 1000$ ppm reported so far [37]. It has been developed at the Naval research center in 1970 by Clark et al. [7]. Initially applicated in naval sonar systems it became a commonly used material in typical transducer and applicator mechanics [38, 39]. However, this composition has a few disadvantages. Due to its brittleness it is not easy to process under robust mechanical conditions and a costly matter because of the rare earth metal content. Galfenol provides the highest magnetostriction, $\lambda = 100 - 500$ ppm at low saturation fields [40], among materials without the content of rare earth elements but with superior mechanical properties compared to other materials with large magnetostriction like Terfenol-D [25, 41].
The origin of the significantly enhanced magnetostriction in Galfenol is still unclear but it is experimentally evidenced that the value depends strongly on the concentration of gallium. Figure 2.3 displays measurements of the magnetostriction component $3/2\lambda_{100}$ in dependence of the content of gallium. With increasing the amount of gallium from zero to approx. 18 % the magnetostriction increases as x^2, reaching a sharp maximum magnetostricton peak at a chemical composition of 81 % iron and 19 % gallium. The curve levels off as the the concentration of gallium is increased further. The value of maximum magnetostriction of $Fe_{81}Ga_{19}$ reaches about $3/2\lambda_{100} = 400$ ppm. Compared to the magnetostriction values reached in pure ferromagnetic elements the magnetostriction in Galfenol tends to be more than 10 times higher than especially in pure iron. This behaviour seems remarkable since the magnetostrictive property, which is characteristic for a ferromagnetic material is amplified over one order of magnitude by doping it with non-magnetic gallium. While the exact mechanism is still a matter of debate a qualitative explanation has been provided by Clark et. al. It is assumed that the sharp magnetostriction peak at $x = 19$ % is attributed to the increase of the magnetoelastic coupling, resulting from the formation of short-range ordered gallium atom pairs along the [100] axis of the bcc structure [42, 35]. For the composition of $Fe_{81}Ga_{19}$ solute clusters of gallium atoms may act as both elastic and magnetoelastic defects in the alloy responding to the magnetization rotation. Increasing the gallium amount further, the crystallographic structure changes and thus only a few or even no clusters which act as magnetoelastic centers remain.

2.3 Structure and growth

Pure iron crystallizes in the $\alpha-$Fe structure with an underlying body-centered-cubic (bcc) lattice structure. Due to comparable sizes of iron and gallium atoms, a few positions of the iron atoms are randomly substituted by gallium atoms in Galfenol as it is schematically shown in figure 2.4. Therefore, the type of alloy is called substitutional. Gallium has a great solubility in iron. To combine both elements to a

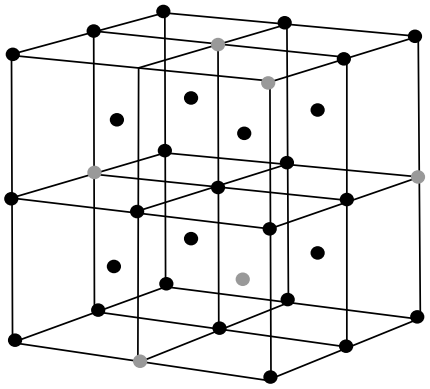

Figure 2.4: Crystallographic structure of Galfenol ($Fe_{81}Ga_{19}$): A body centered cubic crystal lattice of iron (black dots) with random substitutions of gallium atoms (grey dots).

single-phase solid solution, pure gallium and iron ingots are inserted into alumina crucibles and heated above 1600 °C. After crystal growth the ingots are annealed at 1000 °C for three days before cutting out oriented single crystal discs from the slabs. The samples are then furnace cooled and reheated to 800 °C. After this heat treatment the samples are rapidly quenched in cooled water [35, 43]. From this bulk material thin layers of nm thickness can be deposited on substrate wafers by DC magnetron sputtering. In this physical vapour deposition technique accelerated Argon ions from a plasma source sputter atoms from the bulk Galfenol (sputter target) which are deposited on the substrate. Another option to deposit nm Galfenol films on a substrate is the method of molecular beam epitaxy (MBE), an ultra high vacuum evaporation technique for the deposition of single crystals [44]. Galfenol thin films grown on GaAs substrates by MBE reveal a small lattice mismatch between the sample and substrate crystals. This leads to a cubic anisotropy of the film. Moreover, an in-plane uniaxial anisotropy term is confirmed for this composition [45]. Magnetostriction coefficients yielded in Galfenol thin films are as large as in bulk single crystal material [45]. The bcc-like crystal structure of $Fe_{81}Ga_{19}$ is confirmed by X-ray diffraction measurements [35]. Depending on the gallium content in Galfenol the material crystallizes in different crystallographic structures. For gallium concentrations higher than 20 % ordered $D0_3$ or B_2 crystallographic structures may form [46]. If the amount of gallium is below 20 % the disordered bcc-crystallographic lattice is obtained at room temperature (see figure 2.4). Unit cells with gallium substitutions appear rectangular rather than cubic as in the remaining iron cells. Small congregations of these stretched cells appear like "raisins in a cake" especially for a regime of 18 % to 20 % of gallium content [6] leading to specific magnetic properties of Galfenol discussed in the last section.

3 Basics of picosecond acoustics

The application of strain as a powerful tool in order to change the magnetic properties of a ferromagnetic structure has been already demonstrated in some works [22, 23]. Especially in Galfenol, the effect of strain on the magnetic properties is expected to be large due to the enhanced magnetostriction. The modulation of the static magnetic states in Galfenol has been recently demonstrated in a couple of experimental studies involving non-volatile strain-mediated electrical control of magnetization [47] and electrically induced magnetization reversal processes [48]. The studies reported in the present work enhance this approach by scaling the strain-governed manipulation in Galfenol down to nanometers and up to GHz frequencies. The dynamical modulation of magnetization in thin Galfenol films is realized by means of ultrashort strain pulses. The basics of the generation and detection of ultrashort strain pulses in solids has been developed by Thomsen et al. in 1984-1986 [14, 49]. In an opaque material the energy of a femtosecond laser pulse can be converted into a strain pulse. This pulse consists of lattice vibrations that form a coherent wave package of acoustic phonons propagating at sound velocity in the material. Typical frequencies of phonons in the picosecond strain pulse lie in the GHz and sub-THz range. Since the development, picosecond acoustics significantly extend acoustic diagnostics and microscopy, which have been limited by the frequencies of several GHz and thus, in resolution. The same extension is expected in conventional magneto-acoustics [50] by applying picosecond acoustic methods to strain-sensitive magnetic materials.
This chapter gives a brief introduction to principles of picosecond acoustics and general methods of the excitation and generation mechanism of ultrashort strain pulses. In section 3.1, the origins of stress will be introduced within the theoretical background of elasticity. The fundamentals of the generation of acoustic strain pulses will be discussed in section 3.2, followed by section 3.3 where the linear and nonlinear properties of strain pulse propagation will be reviewed.

3.1 Particle displacement and strain

An arbitrary particle at an equilibrium position definded as $\vec{r} = (x, y, z)$ may be shifted to the position $\vec{r}'$. The displacement $\vec{u}$ is written as

$$\vec{u} = \vec{r}' - \vec{r}. \tag{3.1}$$

In order to describe the deformation of a material it is convenient to consider the relative distance between two particles. This distance before and after deformation may be given as $dl = \sqrt{dx^2 + dy^2 + dz^2}$ and $dl' = \sqrt{dx'^2 + dy'^2 + dz'^2}$ with the relation of the corresponding connecting vectors $d\vec{r}$ and $d\vec{r'} = d\vec{r} + d\vec{u}$. It follows that

$$dl^2 = dr_i^2 \tag{3.2}$$

for the initial length and

$$dl'^2 = (dr_i + du_i)^2 = dl^2 + 2\eta_{ij} dr_i dr_j \tag{3.3}$$

for the deformation, wherein η_{ij} denotes the elastic strain tensor components:

$$\eta_{ij} = \frac{1}{2}\left(\frac{\partial u_i}{\partial r_j} + \frac{\partial u_j}{\partial r_i} + \frac{\partial u_j}{\partial r_i}\frac{\partial u_i}{\partial r_j}\right). \tag{3.4}$$

In soft and elastic materials like for example rubber high displacement gradients are reached. Solid crystalline materials are rigid that, in order to avoid permanent deformation, the static displacement gradient is limited to the range of $10^{-4} - 10^{-3}$ [51]. For displacement derivatives in this range the second order term in equation (3.4) is negligible. Thus the strain tensor components for small deformations reduce to:

$$\eta_{ij} = \frac{1}{2}\left(\frac{\partial u_i}{\partial r_j} + \frac{\partial u_j}{\partial r_i}\right). \tag{3.5}$$

The complete strain tensor η is written as:

$$\eta = \begin{pmatrix} \eta_{xx} & \eta_{xy} & \eta_{xz} \\ \eta_{yx} & \eta_{yy} & \eta_{yz} \\ \eta_{zx} & \eta_{zy} & \eta_{zz} \end{pmatrix} \tag{3.6}$$

$$= \begin{pmatrix} \frac{\partial u_x}{\partial x} & \frac{1}{2}\left(\frac{\partial u_x}{\partial y} + \frac{\partial u_y}{\partial x}\right) & \frac{1}{2}\left(\frac{\partial u_x}{\partial z} + \frac{\partial z}{\partial x}\right) \\ \frac{1}{2}\left(\frac{\partial u_y}{\partial x} + \frac{\partial u_x}{\partial y}\right) & \frac{\partial u_y}{\partial y} & \frac{1}{2}\left(\frac{\partial u_y}{\partial z} + \frac{\partial u_z}{\partial y}\right) \\ \frac{1}{2}\left(\frac{\partial u_z}{\partial x} + \frac{\partial u_x}{\partial z}\right) & \frac{1}{2}\left(\frac{\partial u_z}{\partial y} + \frac{\partial u_y}{\partial z}\right) & \frac{\partial u_z}{\partial z} \end{pmatrix}. \tag{3.7}$$

Diagonal elements represent volume compression or tension of the material while off-diagonal elements represent shear strains.

Each infinitesimal volume element ΔV of the material is exposed to inner body forces $d\mathscr{F} = \sigma df$ by surrounding volume elements. It is defined by σ, the symmetric stress tensor with the dimension of pressure and df denoting a surface element. In the limiting case of long phonon wavelength compared to the lattice constants, the

discrete atomic structure becomes negligible. In terms of the continuous displacement field u and the mass density $\rho(r)$ (depending on the atomic mass and volume of the unit cell) this relation turns into

$$\rho \frac{\partial^2 u_i}{\partial t^2}(r,t) = \sum_j \frac{\partial}{\partial r_j}\sigma_{ij}(r), \tag{3.8}$$

the well known Hook's Law [52]. Strain is induced when a body is stressed. This implies a linear relation between stress σ and strain η:

$$\sigma_{ij} = C_{ijkl}\eta_{kl}. \tag{3.9}$$

Both quantities are coupled by C_{ijkl}, the fourth-order tensor of elastic constants. Inserting this relation in (3.8), leads to

$$\rho \frac{\partial^2}{\partial t^2}u_i(r,t) = \sum_{jkl} C_{ijkl}\frac{\partial^2}{\partial r_k \partial r_l}u_j(r,t), \tag{3.10}$$

the wave equation as a function of the displacement $u(r,t)$. The optical excitation of picosecond strain pulses in thin metal films leading to the displacement field described by the dynamics above, will be theoretically explained in the following section.

3.2 Strain pulse generation

A sub-picosecond light pulse incident on a thin opaque film is absorbed at the surface. The light absorption leads to a thermal stress which results in an acoustic strain pulse launched into the material [49]. The generation method considered in the following refers to the excitation of picosecond strain pulses in a thin metal film deposited on a GaAs substrate as this is the option of strain pulse generation relevant to the experiments in this work.

Figure 3.1 provides a general overview of the geometrical configuration for the acoustic strain pulse generation. A thin metal film (aluminum) of thickness d deposited on the surface of a semiconductor (GaAs) substrate serves as an opto-elastic transducer[1]. A laser pulse of sub-picosecond duration and energy Q incident on the surface of the metal film along the z direction illuminates the area $\tilde{A}$. Assuming $\tilde{A}$ to be large compared to the thickness d and ζ, the penetration depth of the light, the total energy deposited per unit volume reads

$$W(z) = (1-R)\frac{Q}{\tilde{A}\zeta}\exp\left(\frac{z}{\zeta}\right), \tag{3.11}$$

[1] Aluminum/GaAs is one possible choice from a variety of transducer/substrate combinations currently in use for strain pulse generation [53, 54].

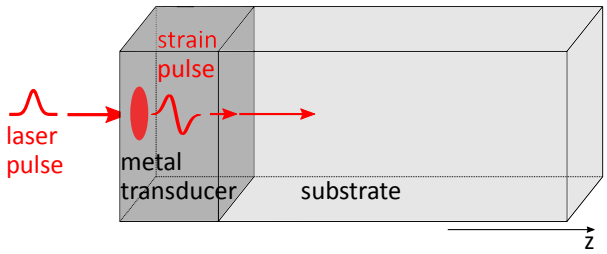

Figure 3.1: Scheme of the strain pulse generation in a thin metal film deposited on a semiconductor substrate.

with R denoting the back-reflection coefficient of the light at the metal surface. The heating of the film is indicated by a temperature rise $\Delta T(z) = W(z)/\tilde{C}_v$ wherein $\tilde{C}_v$ denotes the specific heat of the material. Thus, Hook's Law (3.9) is expanded by the influence of the isotropic thermal stress:

$$\sigma_{ij} = C_{ijkl}\eta_{kl} - 3B\tilde{\alpha}\Delta T(z), \tag{3.12}$$

with $\tilde{\alpha}$ denoting the linear expansion coefficient and B the bulk modulus. Thus, the only motion can be considered to be parallel to z (see fig. 3.1). Therefore, the only non-vanishing component of the elastic strain tensor is η_{zz} and the stress-strain relation (3.12) remains

$$\sigma_{zz} = 3B\frac{(1-v)}{(1+v)}\eta_{zz} - 3B\tilde{\alpha}\Delta T(z), \tag{3.13}$$

with v being the Poisson's ratio. Thus, the equations of motion to solve (3.10) read:

$$\rho\frac{\partial^2 u_z}{\partial t^2} = \frac{\partial \sigma_{zz}}{\partial z}, \tag{3.14}$$

$$\eta_{zz} = \frac{\partial u_z}{\partial z}. \tag{3.15}$$

with u_z defining the displacement along the z direction. A solution under the conditions of zero initial strain and $\sigma_{zz} = 0$ at the open surface has the form

$$\eta_{zz}(z,t) = (1-R)\frac{Q\alpha}{A\zeta\tilde{C}_v}\frac{1+v}{1-v}\left(e^{(-z/\zeta)}(1-\frac{1}{2}e^{-\nu t/\zeta}) - \frac{1}{2}e^{-(z-\nu t)/\zeta}sgn(z-\nu t)\right). \tag{3.16}$$

This expression describes a bipolar strain pulse consisting of a wave package of coherent acoustic phonons. The strain pulse propagates at longitudinal speed of sound ν in the material along the z direction involving a discontinuity at $z = \nu t$. The width

of the strain pulse is given by the penetration depth ζ. The first part includes the time independent strain due to the thermal expansion near the surface where the energy is absorbed. The pulse profile includes a compressive part where $\eta_{zz} < 0$ and a tensile part with $\eta_{zz} > 0$. So far, the discussed strain pulse profile is an approxima-

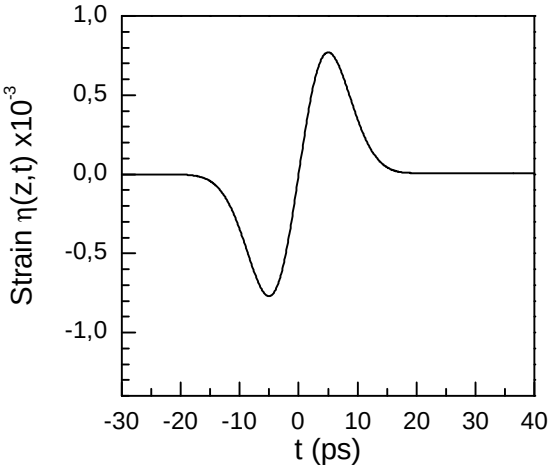

Figure 3.2: Bipolar strain pulse profile $\eta_{zz}(z,t)$ after excitation in a thin metal transducer at a propagation distance z larger than the penetration depth but still near the surface.

tion. For strain pulses observed in the experiments additional effects such as thermal conductivity and electron diffusion that modulate the shape of $\eta_{zz}(z,t)$ have to be considered. When the light pulse is absorbed, a thin layer of hot electrons is produced near the film surface. The energy of these hot electrons is not instantaneously transferred to the lattice system but the electrons diffuse into the film before losing their energy to the lattice via phonon emission. A detailed theoretical model of the process of electron diffusion in form of a two-temperature model can be found in Ref. [55]. These effects lead to a broadening of the shape of $\eta_{zz}(z,t)$ and the discontinuity is smoothed out. The result is a shape which is modeled by the derivative of a Gaussian function [55, 53] as shown in figure 3.2. With respect to the topics of this work, the strain characteristics apparent from equation (3.16) adequately describe the profile of the strain pulse. Inclusion of the effects of electron- and thermal diffusion mainly lead to smoothing and stretching of the strain pulse shape.

After being launched, the strain pulse $\eta_{zz}(z,t)$ propagates towards the interface between the metal film and the substrate. Due to the mismatch of acoustic impedances at the interface, the strain pulse is partially reflected at the discontinuity and propagates back into the metal film while the other part is transmitted into the substrate. The back-traveling pulse in the metal film is reflected at the open surface. The tem-

poral evolution of $\eta_{zz}(z,t)$ injected into the substrate is shown in 3.3 a). It displays the main bipolar pulse shape with a compressive part followed by tensile part followed by a ringing with a smaller amplitude. This tail originates from the back-traveling strain pulse reflected at the open surface. The typical amplitude of $\eta_{zz}(z,t)$ may reach 10^{-3} with a duration of 100 ps.
The nonlinear properties of acoustic wave propagation at higher amplitudes and after propagation distances of more than $10\mu m$ will be discussed in the next section. In this case the approximation for $\eta_{zz}(z,t)$ is no longer valid and anharmonic properties have to be taken into account.

3.3 Formation of solitons

The limits of linear elasticity are reached when the strain pulse amplitude is close to 10^{-3}. Anharmonic wave propagation with non-linear dispersion may result. Elastic nonlinearities can have strong effects on the propagation of acoustic waves in media. Under these circumstances picosecond acoustic solitons may form at propagation distances about $z = 50$ μm in GaAs, see for example Ref. [56]. A soliton is known as a stable wave packet, the result of the balancing between non-linearity and dispersion in the material propagating faster than sound velocity. A first experimental observation of solitonic wave propagation in Si, MgO and sapphire can be found in [57]. Theoretically described by solutions of the Korteweg-de-Vries equation, solitons have been demonstrated in a lot of physical systems [58, 59].
At this point, the wave equation governing the anharmonic propagation of the acoustic strain pulse over long distances is derived. Furthermore, the effect of the formation of solitons on the time evolution of $\eta_{zz}(z,t)$ in a GaAs substrate will be examined.
Taking into account nonlinearities, the wave equation (3.10) for a longitudinal wave with displacement in direction of the wave propagation is modified to

$$\rho_0 \frac{\partial^2 u_z}{\partial t^2} = \left(C_2 + C_3 \frac{\partial u_z}{\partial z} \right) \frac{\partial^2 u_z}{\partial z^2}. \tag{3.17}$$

C_2 and C_3 are combinations of the second and third order elastic constants of tensor C_{ijkl}. Further details on the values of the coefficients are given in [57]. The non-linear dispersion relation due to the finite spacing of lattice atoms which have to be taken into account for very short wavelengths may be given as

$$\omega = ck - \gamma' k^3 + ..., \tag{3.18}$$

wherein $c = (C_2/\rho_0)^{1/2}$ and γ' is a constant [57]. As a consequence, equation (3.17) has to be extended in order to receive the dispersion relation given above:

$$\rho_0 \frac{\partial^2 u_z}{\partial t^2} = \left(C_2 + C_3 \frac{\partial u_z}{\partial z} \right) \frac{\partial^2 u_z}{\partial z^2} + 2\rho_0 c\gamma' \frac{\partial^4 u_z}{\partial z^4}. \tag{3.19}$$

Instead of using the displacement u_z, the wave equation will be considered in terms of the strain $\eta_{zz} = \frac{\partial u_{zz}}{\partial z}$ [eq. (3.15)] in the following. The derivative of (3.19) with respect to z thus yields

$$\rho_0 \frac{\partial^2 \eta_{zz}}{\partial t^2} = C_2 \frac{\partial^2 \eta_{zz}}{\partial z^2} + C_3 \frac{\partial}{\partial z}\left(\eta_{zz} \frac{\partial \eta_{zz}}{\partial z}\right) + 2\rho_0 c\gamma' \frac{\partial^4 \eta_{zz}}{\partial z^4}. \tag{3.20}$$

Comparison of this equation of motion of η with an equation of the Korteweg-de-Vries form

$$\frac{\partial \eta_{zz}}{\partial t} = -B_1 \frac{\partial \eta_{zz}}{\partial z} - B_2 \eta_{zz} \frac{\partial \eta_{zz}}{\partial z} - B_3 \frac{\partial^3 \eta_{zz}}{\partial z^3}, \tag{3.21}$$

shows that with the right relation between B_1, B_2 and B_3 and the constants C_2, C_3 and γ' the solutions of (3.21) are also solutions of the wave equation (3.20).
Figure 3.3 shows the strain pulse profile and the corresponding frequency spectra for different strain pulse amplitudes after the pulse has traveled a propagation distance of 110 μm in a GaAs substrate. The calculation data based on solutions of eq. (3.20) has been provided by P. Capel[1]. Panel (a) displays $\eta_{zz}(z,t)$ at an amplitude of $4 \cdot 10^{-5}$. The temporal profile shows that the strain excitation is still in the linear regime. The corresponding frequency spectrum (right panel (d)) covers frequencies in the subteraherz range. As the amplitude of $\eta_{zz}(z,t)$ increases nonlinearities come into play and the wave propagation becomes anharmonic at long travel distances. Due to the increase of velocity the compressive (negative) part of the strain propagates fast while the tensile (positive) part slows down. Thus, a formation of a N-shaped pulse can be obtained as shown in figure 3.3 (b). As a consequence of the sharpening of the N-shape function higher frequency components reaching up to several THz appear (plot (e)). Because of dispersion, the velocity of these high frequency components is slowed down. A balancing of the anharmonicity and dispersion leads to the formation of acoustic solitons traveling faster than the longitudinal wave and which can be observed as a trail of oscillations in the leading edge of the time evolution of $\eta_{zz}(z,t)$ at a propagation distance $z = 110$ μm and strain amplitudes of $4 \cdot 10^{-4}$ and $8 \cdot 10^{-4}$ (see 3.3 (b) and (c), respectively). Although the main solitonic characteristics are successfully described by the Korteweg-de-Vries equation, the behavior of solitons is still a matter of intensive research but beyond the scope of this work. Due to remarkable spatial and temporal dimensions down to a few nm and ps, acoustic solitons are supposed to find application in alternative studies of the optical response of nanostructures [21].

[1] P. van Capel, Universiteit Utrecht, Netherlands

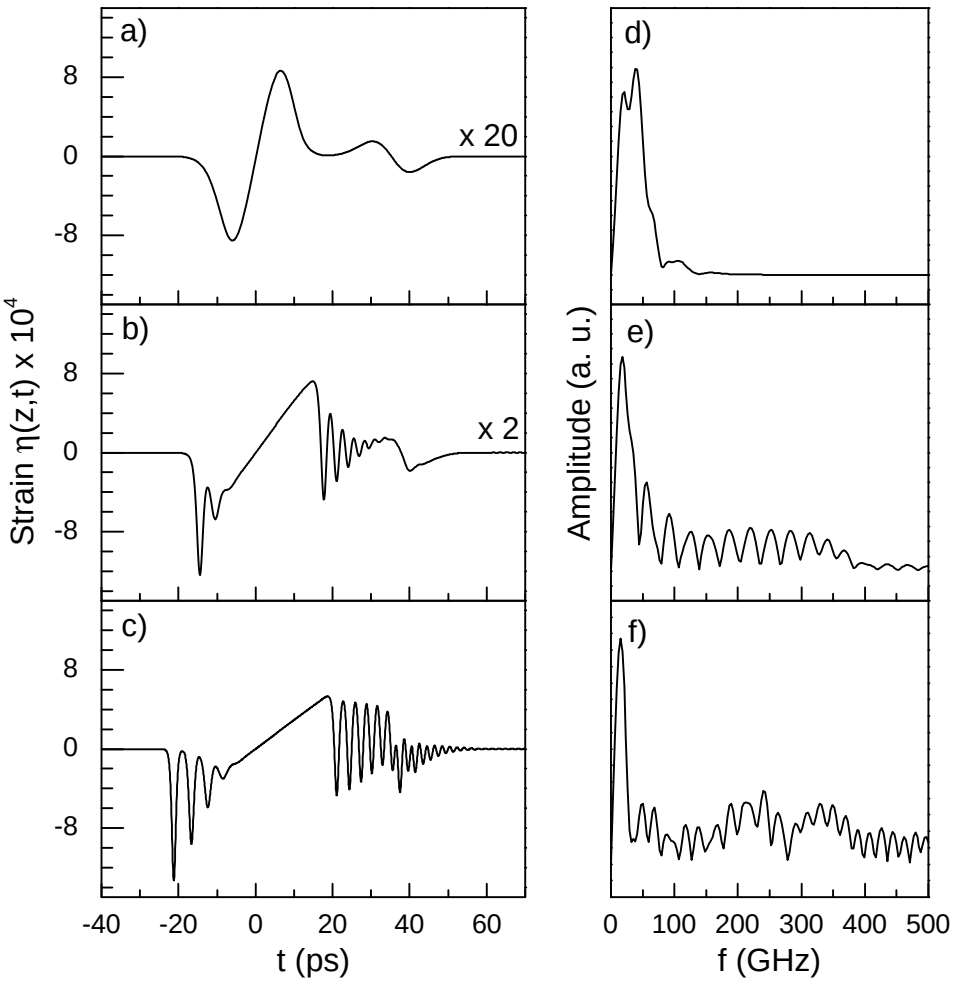

Figure 3.3: Left panels (a)-(c): Temporal evolution of $\eta_z(z,t)$ at a propagation distance of $z = 110$ μm and strain amplitudes of $4 \cdot 10^{-5}$, $4 \cdot 10^{-4}$ and $8 \cdot 10^{-4}$. Right panels (d)-(f): Corresponding frequency spectra of $\eta_z(z,t)$, Calculations based on the Korteweg-de-Vries equation [56], data provided by P. Capel.

4 Experimental concept

The parameters of picosecond strain pulses in combination with the properties of Galfenol described in the previous chapters allow the realization of ultrafast strain-induced modulation of magnetization. This chapter presents the experimental realization of such a modulation. This chapter is devided into two parts. The first part introduces to the physical basis of the expected coherent response of the magnetization on the ultrafast acoustic impact in a phenomenological way. The second part is dedicated to the certain experimental realization used for the studies in this work. Since the results of the studies presented here have been prepared in a mostly experimental work, some important issues of experimental techniques are not only an integral part of this thesis but also essential for the entire insight into the work. Because strain-induced signals in ferromagnetic thin films are measured in the time domain, special attention is drawn to the used laser system and to the detection scheme in which the probe laser light intensity and polarization is monitored.

4.1 Principles of ultrafast magnetization manipulation induced by picosecond strain pulses

The experimental study of strain induced magnetization modulation investigated in this work, is based on the injection of optically generated picosecond strain pulses into the ferromagnetic layer which disturb the magneto-crystalline anisotropy of the material. This ultrafast acoustic method has been recently reported for the ferromagnetic semiconductor GaMnAs [22, 23]. In contrast, electrical and optical methods of magnetization control have also been demonstrated by optical heating, increasing of the carrier density or via application of electric fields [60, 61, 62, 63]. These applications have disadvantages as the generation of nonequilibrium carriers and thermal phonons limiting operation speeds and the frequency ranges.

To provide an easy access to the general phenomenological approach of strain induced magnetization modulation discussed here the following conditions shown in figure 4.1 are used. The sample structure contains a metal transducer for strain pulse generation (see section 3.2) evaporated on one side of a GaAs substrate and the ferromagnetic layer on the opposite side of the substrate. Figure 4.1 only displays the GaAs substrate and the Galfenol layer on top. An external magnetic field

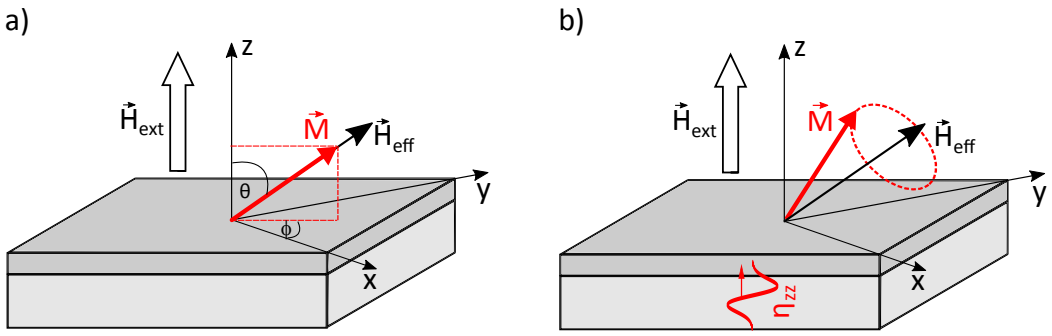

Figure 4.1: Schematic demonstration of strain-induced magnetization modulation in a thin ferromagnetic layer grown on a GaAs substrate. An external magnetic field $\vec{H}_{\text{ext}}$ is applied along the z-direction normal to the sample surface: a) At static conditions, the equilibrium orientation of the effective field $\vec{H}_{\text{eff}}$ governs the direction of the layer magnetization $\vec{M}$ which aligns parallel to $\vec{H}_{\text{eff}}$. (b) Magnetization precession of $\vec{M}$ around $\vec{H}_{\text{eff}}$ after injection of the strain pulse η_{zz}.

$\vec{H}_{\text{ext}}$ of moderate strength is oriented along the $\vec{z}$ direction[1] i.e. normal to the sample surface. The layer magnetization aligns parallel to the effective field $\vec{H}_{\text{eff}}$, that is governed by the balancing of the external field $\vec{H}_{\text{ext}}$ and the intrinsic magnetic anisotropy determined by the ferromagnetic layer parameters [see figure 4.1 a)].
A picosecond strain pulse generated in the metal transducer opposite to the ferromagnetic film propagates through the intermediate GaAs substrate towards the film. Reaching the ferromagnetic layer, the strain pulses changes the magnetic anisotropy [see eq. (2.1)] by coupling of the external strain to the magneto-elastic parameters, and thus, changing the direction of $\vec{H}_{\text{eff}}$ out of its equilibrium position which was governed by $\vec{H}_{\text{ext}}$ and the magnetic anisotropy under static (unstrained) conditions. This short but intense impact on $\vec{H}_{\text{eff}}$ results in a precessional motion of $\vec{M}$ around $\vec{H}_{\text{eff}}$ [see figure 4.1 b)] . Due to the finite duration of the strain pulse inside the layer, the direction of $\vec{H}_{\text{eff}}$ changes continuously while the strain pulse propagates through the film. Thus, the precessional motion of $\vec{M}$ follows a variable position of $\vec{H}_{eff}$ leading to a trajectory which is not easy to trace. But, the magnetization tilt efficiency is assumed to be governed by the material-dependent strength of the magneto-elastic coupling parameters $A_{2\eta}$, $A_{4\eta}$ and A_{2xy} in eq. (2.1) relating to the coupling of exter-

[1]Several experiments reported in this thesis have been performed at different orientations of $\vec{H}_{\text{ext}}$, either directed normal to the sample surface or in-plane (see chapters about experimental results). But in order to provide a structured overview of the relevant physical method at this point the shown concept is restricted to the application of $\vec{H}_{\text{ext}}$ perpendicular to the sample surface.

nal longitudinal or shear strain to the magnetization. When the strain pulse has left the layer, $\vec{H}_{\text{eff}}$ changes back to its equilibrium position while $\vec{M}$ remains precessing until it finally relaxes back to the equilibrium state. The magnetization precession dynamics governed by the strain- and thus, time-dependent effective field $\vec{H}_{\text{eff}}(t)$ can be described by the *Landau-Lifshitz-Gilbert* equation [26]. Whereas the derivative of the free energy density F derived in chapter 2.1 determines value and direction of $\vec{H}_{\text{eff}}$. Thus, the equation of motion of the magnetization is given by [64]

$$\frac{1}{\gamma}\frac{d\vec{M}}{dt} = -\vec{M} \times \vec{H}_{\text{eff}}(\vec{M}, t) - \frac{G}{(\gamma M_0)^2}\left[\vec{M} \times \frac{d\vec{M}}{dt}\right], \tag{4.1}$$

with the gyromagnetic ratio $\gamma = g\mu_B/\hbar$ and μ_B as the *Bohr* magneton. The second term takes into account the precession damping of the magnetization with G denoting the *Gilbert* damping parameter. The frequency of the resonant magnetization precession (Ferromagnetic resonant frequency, FMR) dependent on the applied external field can be obtained from [45, 65]:

$$\left(\frac{\omega}{\gamma}\right)^2 = \frac{1}{M^2 \sin^2(\theta_0)}\left[\frac{\partial^2 F}{\partial\theta^2}\frac{\partial^2 F}{\partial\phi^2} - \left(\frac{\partial^2 F}{\partial\theta\partial\phi}\right)^2\right], \tag{4.2}$$

wherein ω defines the resonant angular frequency. θ and ϕ denote the polar and in-plane azimuthal angles of the magnetization direction [see figure 4.1] which corresponds to the minimum of the free energy density, $\frac{\partial F}{\partial\theta}$ and $\frac{\partial F}{\partial\phi}$ at equilibrium. The damping parameter is neglected for simplicity.

4.2 Experimental realization

This section provides a general overview of the experimental setup used to carry out the experiments presented in this study. The focus lies on the time resolved pump-probe technique with respect to important technical key features relevant to the strain pulse generation, signal detection and measurement. A detailed plot of the experimental setup is shown in figure 4.2. Specific modifications of a few technical parts of the setup will be highlighted in the chapters later on when it is required. The experimental setup is built around three major components, a high energy laser system, a bath cryostat equipped with superconducting magnets and a detection system.

For the generation of ultrafast acoustic strain pulses a femtosecond laser system which is able to generate high energy pulses in the μJ range is used. Thereby, excitation densities up to 40 mJ/cm^2 in front of the metal transducer on the backside of the sample can be realized. The laser system provided by *Coherent* consists of a regenerative amplifier (*RegA 9000*) which amplifies MHz-pulses supplied by a Titanium-Sapphire

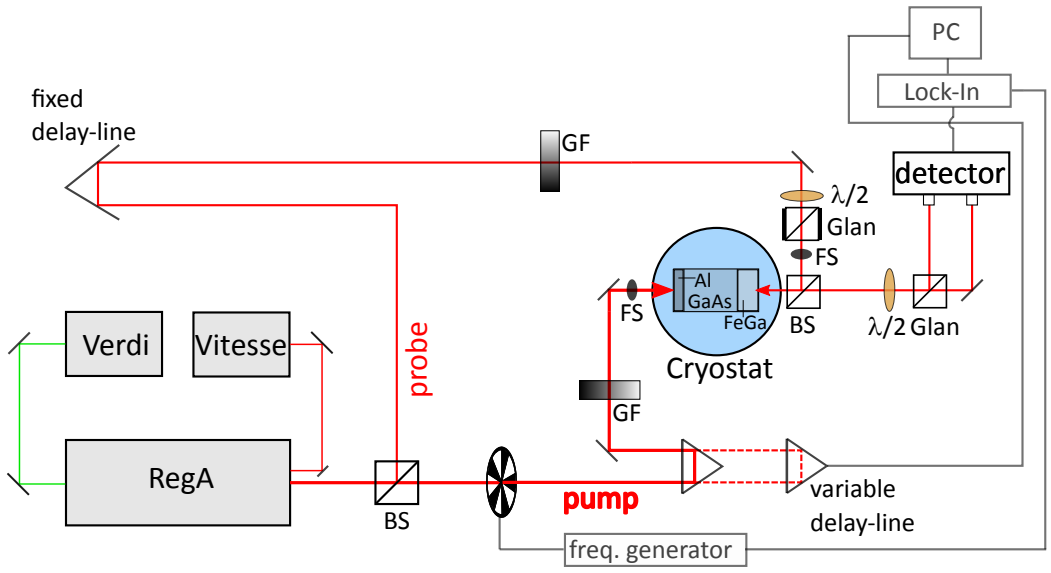

Figure 4.2: General experimental realization. Red lines: Optical path ways of the pump (thick lines) and the probe (thin lines) beams of $\lambda = 800$ nm wavelength generated in the RegA-laser-system. Components of the electronic synchronization and data acquisition are coloured in light grey. Optical components for beam polarization and focusing: BS (Beam Splitter), GF (Grey Filter), FS (Focusing lens), $\lambda/2$ (half-wave plate), Glan (Glan-Taylor prism).

(Ti:Sa) laser (*Vitesse Duo*). This so called seed-laser, pumped by an integrated Neodymium-Vanadate-($Nd : YVO_4$)-laser, produces sub-100 fs laser pulses at a repetition rate of 80 MHz and a wavelength of $\lambda = 800$ nm. The Vitesse-output beam with an averaged power of 200 mW is injected into the RegA-cavity. An injected seed pulse from the Vitesse laser passes through the RegA cavity until it is coupled out. The active medium, also a Ti:Sa crystal, inside the RegA cavity is pumped by an external diode-pumped Neodymium-Vanadate($Nd : YVO_4$) continuous wave laser ($\lambda = 532$ nm). To the benefit of a higher pulse power up to 4 μJ the repetition rate of the RegA output pulses is lower than the repetition rate of the seed-laser. The average output power of the RegA-cavity is about $1,0$ W at a repetition rate of 200 kHz. Single pulses provide a radial distribution close to a Gaussian shape.
The laser beam that leaves the cavity is split into two perpendicular beams by a Beam Splitter (BS, figure 4.2). 90 % of the beam passes through the beam cube without being reflected. This main part, called *pump* beam in a time resolved pump-probe scheme is used to excite the acoustic strain pulses in the metal transducer deposited on the GaAs substrate at the sample backside. The spot size is 100 μm (full width at half maximum of the Gaussian-shaped radial power distribution) in front of the metal transducer. The excited strain pulse travels through the GaAs substrate and reaches

the ferromagnetic film after certain propagation times of 20 to 30 ns. Magnetization modulation signals from the Galfenol film are probed opposite to the transducer side where the strain pulse is excited. Therefore, the *probe* beam, about 10 % of the RegA output, is reflected at 90° in the beam splitter in front of the RegA system and used for the detection of the measurement signals at the sample surface. In order to temporally align the incidence of the strain pulse arrival and the probe at the sample the probe beam has to travel an extended optical path way calculated to the time the strain pulse needs to travel through the substrate to the ferromagnetic film. This is realized by a fixed delay line (retro-reflector) in the probe beam way.The probe beam is linearly polarized by a Glan-Taylor prism (and a preceding $\lambda/2-$plate) and then focused onto the sample surface by a focusing lens with a spot size of 50 μm in diameter. A variable delay line (*Aerotech*) integrated in the pump beam way varies the time delay between strain excitation and detection thus providing time-resolved measurements in a detection time window covering 4 ns at a temporal resolution of $0,1$ ps.
The investigated sample structure is mounted in a bath cryostat (*Oxford Instruments*) which allows measurements Helium temperatures down to a few K. Additionally, the cryostat is equipped with superconducting magnet split coils generating magnetic fields up to $\mu_0 H_{\text{ext}} = 7$ T in perpendicular ($\vec{H}_{\text{ext}} \perp \vec{z}$) and in-plane ($\vec{H}_{\text{ext}} || \vec{z}$) geometry. Measurements that require high external magnetic fields at ambient temperatures become possible through integrated heating elements in the cryostat warming up the sample chamber up to room temperature. The sample may be manually rotated around its vertical, horizontal and around its azimuthal axis in order to ensure perfect alignment of the back reflected probe beam along the optical axis of the setup.
The modulation of the reflected probe pulse is monitored throughout the following detection scheme. The detector apparatus consists of a balanced photoreceiver with two silicon photodiodes (*Nirvana, New Focus*). The physical background of two different types of signal detection based on monitoring the (i) intensity via one single diode and (ii) the polarization rotation of the reflected probe beam via a balanced scheme will be introduced in the section below.
Additional electronics are used to minimize the effect of external noise sources and to improve the signal to noise ratio. The frequency of the pump beam is modulated by a mechanical chopper (*Stanford Research*). This reference signal is multiplied with the measured signal from the balanced detector diodes in a Lock-In amplifier. Contributions from signal components with frequencies beyond the reference frequency are suppressed. The Lock-In transmits the output signal locked to the reference frequency to a computer where the measurement data is acquired.

4.3 Monitoring of strain induced magnetization modulation

The signal detection is based on the measurement of the modulation of the probe light intensity $I(t)$ and polarization $\Delta\psi(t)$ as a function of the time delay between the pump and probe beam. After reflection from the sample surface, the probe beam is directed to the detection system consisting of a set of polarization optics in front of the balanced photo detector. To set the polarization plane, the beam travels through a $\lambda/2$ wave plate and a Glan-Taylor polarizing prism afterwards. The Glan-Taylor prism splits the incoming beam ray in a part which is transmitted straight ahead and the other part deflected in the prism. Both beams of perpendicular polarization are directed to the photodiodes of the detector (see figure 4.2). The laser intensity on the diodes is altered by the $\lambda/2$ wave plate in front of the polarizer by rotation of the polarization orientation of the probe beam.
To monitor the intensity signal, the whole intensity of the reflected probe beam is directed to only one photodiode by rotation of the $\lambda/2$ wave plate. The second diode is blocked. Thereby, the intensity modulation of the probe is monitored which provides characteristic features of the strain pulse propagation inside the sample. This detection scheme based on the elasto-optical effect leads to a typical interference signal that will be examined more detailed in section 5.2.

The polarization rotation of the reflected probe light is monitored by means of the polar *Magneto-optical Kerr effect*. In a balanced detection scheme the two orthogonally polarized beam rays components leaving the Glan-Taylor polarizer are balanced to equal intensities onto the photodiodes. The magneto-optical Kerr effect (MOKE) or 'Kerr rotation' is analogous to the well-known *Faraday* effect describing the rotation of the polarization plane of light propagating through a crystal in an external magnetic field. Instead, the MOKE describes the rotation of the polarization plane of light reflected from a magnetic surface. While the Faraday effect is restricted to transparent media, the MOKE can be measured from any magnetized smooth surface [66]. Different configurations of the MOKE, dependent on the orientation of the sample magnetization, are distinguished. The description given here is restricted to the discussion of the polar MOKE which is monitored when the magnetization is oriented normal to the surface. A detailed macroscopic description of the MOKE is based on the dielectric tensor theory that can be found in Ref. [67]. Microscopically, the coupling between the electric field of the light and the magnetization originates from the spin-orbit interaction [68]. While the detailed analysis may be found elsewhere, the MOKE may be also illustrated in a phenomenological approach using the intuitive picture of a Lorentz force acting on perturbed electrons. Figure 4.3 displays a sketch of the polar MOKE geometry with arbitrary orientation of the sample magnetization displaying the M_z component normal to the surface. $\vec{E}_\mathrm{I}$ indicates the vector

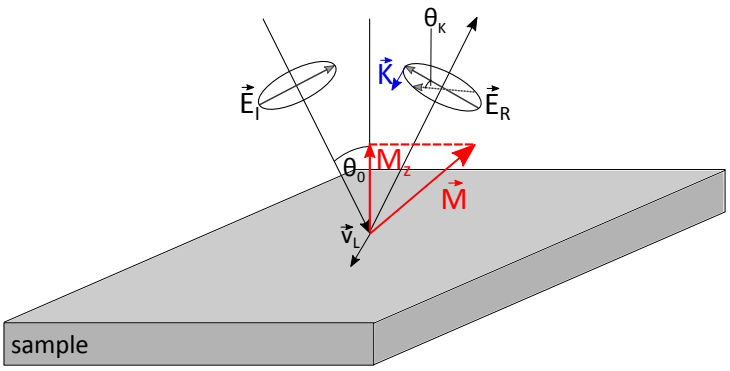

Figure 4.3: Scheme of the polar magneto-optical Kerr effect: The magnetization $\vec{M}$ with arbitrary orientation displays a M_z component normal to the sample surface. $\vec{E}_\mathrm{I}$ denotes the electric field vector of the probe light incident on the sample surface. The regularly reflected electric field amplitude is $\vec{E}_\mathrm{R}$. $\vec{K}$ results from the changed direction of electron oscillation induced by the Lorentz force $\vec{v}_\mathrm{L}$. The new direction of the rotated $\vec{E}_\mathrm{R}$ is illustrated as the dashed vector. The Kerr rotation angle is defined as Θ_K and the angle of the incident light beam is given by Θ_0.

of the polarization plane of the incident light given by the electric field component and $\vec{E}_\mathrm{R}$ the regular electric field component of the emerging light which initially has the same polarization direction as $\vec{E}_\mathrm{I}$. The linearly polarized light beam incident on the surface induces electrons to oscillate parallel to the light polarization plane. The Lorentz force $v_{\vec{L}}$ acting perpendicular to the initial oscillation and the magnetization direction induces an additional component that changes the direction of the oscillatory motion of electrons denoted by $\vec{K}$. As a result, the plane of the emerged light $\vec{E}_\mathrm{R}$ rotates. The new direction of the polarization plane of $\vec{E}_\mathrm{R}$ is illustrated as the dashed vector in figure 4.3. At normal incidence $\Theta_0 = 0$ as realized in the reported experiments the polar MOKE has the strongest effect while other magneto-optical configurations may be neglected.
In essence, the strain induced changes of the magnetization component M_z normal to the sample surface may be monitored by means of the polar MOKE. Thereby, the rotation of the polarization plane of the reflected probe beam defined as the Kerr angle Θ_K relates directly to changes of M_z.

5 Picosecond strain pulses in high-index GaAs

In chapter 3 the general overview of the method to generate picosecond strain pulses has been given. While only longitudinal (compressive) strain pulse has been considered before, the described technique may be also used for the generation of picosecond shear strain pulses. Shear strain pulses are assumed to manipulate the layer magnetization of nanometer films more effectively, because, contrary to longitudinal pulses, they contain a strain component in the film plane. They also may provide a better spatial resolution due to the lower sound velocity. Until now, the generation of picosecond shear strain pulses remains challenging. In general, the reduction of the system's symmetry is required for the generation [69]. This is realized by a strain pulse propagating along the low-symmetry direction of a crystal lattice. This concept has been approved in several works [69, 70, 71, 72], but with the signal detection and strain pulse generation at the same side of the sample. In this work, a low-symmetry [311]-GaAs substrate is used to fulfil the broken-symmetry condition. But as shown in the experimental setup in the previous chapter, the detection of the strain pulse at the substrate surface is realized opposite to the strain generation at the sample backside. The methods of investigation is the picosecond acoustic interferometry introduced by Thomsen et al. [49]. In addition to this traditional technique based on the detection of the intensity modulation of the reflected probe pulse, the method of method of picosecond acoustic polarimetry is introduced in this chapter, which utilizes the modulation of the probe pulse polarization. This provides a much better sensitivity in detection of shear strain pulses. As a result, it is shown that both compressive and shear pulses may be generated and separately detected in such a scheme.
This chapter first introduces to the physical basics of the generation of shear strain pulses in a low-symmetry GaAs structure. Then the principle of monitoring the strain propagation by picosecond opto-acoustic interferometry and polarimetry will be discussed. Finally, the results will be presented together with model calculations of the strain-induced signals, substantiating the experimental findings.

5.1 Acoustic modes in low symmetry systems

By now, the principles of strain pulse generation and propagation has been considered only for longitudinal acoustic (LA) phonons. But beside the longitudinal excitation mode also transverse acoustic (TA) phonons can be generated by the methods of picosecond acoustics. The different acoustic modes are sketched in a simple model in

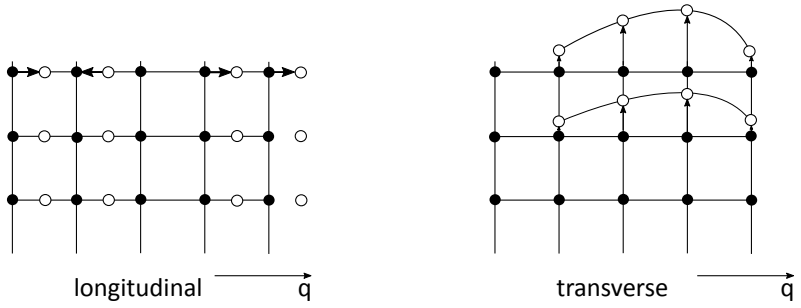

Figure 5.1: Schematic illustration of longitudinal and transverse lattice displacement. Equilibrium positions of the lattice atoms are displayed as black dots and displaced lattice atoms as circles.

figure 5.1. In case of LA phonons, the lattice displacement occurs along the propagation direction of the acoustic wave, denoted by the wave vector q. In the TA mode, the lattice atoms are displaced perpendicular to q. The propagation and detection depends on the symmetry conditions of the substrate the strain pulse is propagating through. The excitation of TA strain requires a reduction of the system symmetry [69]. In case of high-symmetry conditions, that means, the lattice structure grown along the high-symmetry axes ([100], [010], [001], [111]), and a large laser excitation spot, only pure longitudinal acoustic modes are excited [22]. The lattice distortions along the strain pulse propagation direction contain only longitudinal components. One option to break the symmetry is to reduce the symmetry of the lattice structure. Therefore, so-called high-index substrates are used. In these structures the plane of the crystal is oriented at an oblique angle to the main crystallographic axes. Figure 5.2 illustrates the sample geometry of a high-index [311]-GaAs substrate with respect to the orientation of the crystallographic axes as it is used in the samples in this work. Acoustic strain pulses propagating in this structure contain mixed modes of compressive and shear strain components. They are called quasi longitudinal (qLA) and quasi transverse acoustic (qTA) strain pulses. The detailed injection and detection characteristics in the experimental scheme will be shown in section 5.3.

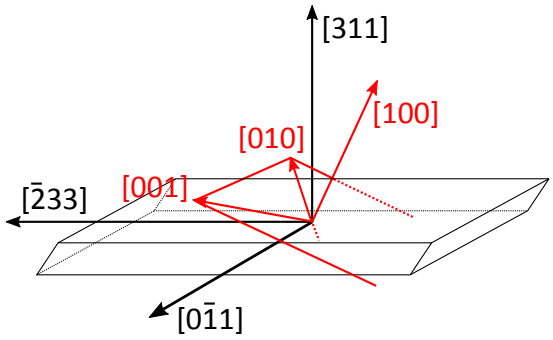

Figure 5.2: Illustration of the sample geometry of a high-index [311]-GaAs substrate with the orientation of the crystallographic axes [73].

5.2 Opto-acoustic interferometry

The optical detection of strain pulses is based on the elasto-optical effect. In case of a GaAs substrate it describes the acousto-optical coupling of the absorbed light in the near surface region of the sample and the strain pulse propagating inside. The strain pulse injected into the GaAs substrate perturbs the dielectric permittivity of the structure, leading to a change in the material's refractive index n. This is manifested in a change of reflectivity of the probe light. The change of the refractive index Δn is given by [49]

$$\Delta n(z,t) = \frac{\partial n}{\partial \eta}\eta(z,t). \tag{5.1}$$

The calculation of the change in the probe light reflectivity $\Delta R(t)$ is based on the solution of the *Maxwell* equations inside the film for a variation of the optical properties in z [49]:

$$\Delta R(t) \propto \cos\left(\frac{4\pi n\nu t}{\lambda} - \delta\right) e^{-z/\zeta}. \tag{5.2}$$

Here, λ denotes the probe beam wavelength, ν the strain pulse propagation velocity of either qLA or qTA strain pulses, $n = 3,6$ the refractive index of GaAs and δ terms a phase shift. The probe light incident on the sample surface is partly reflected from the surface and partly absorbed in the sample with a certain penetration depth. As the strain pulse travels towards the surface the transmitted part of the probe beam will be reflected from the discontinuity caused by the strain pulse [74] as it can be seen from the descriptive model figure 5.3. Both, the beam reflected from the sample surface and the part reflected from the discontinuity interfere with each other leading to a time dependent spectrum of intensity oscillations. The corresponding oscillation

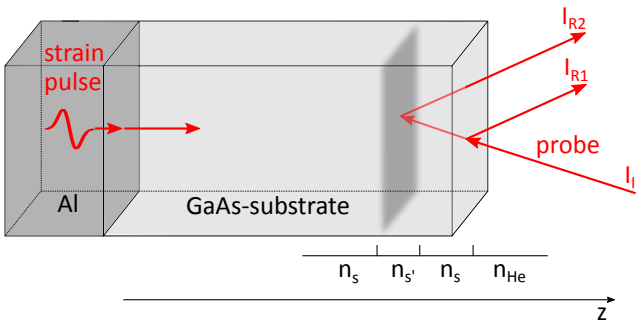

Figure 5.3: Generation of Brillouin oscillations of the reflected probe beam. n_s and n_{He} denote the different refractive indices of the GaAs substrate and the cryogenic (Helium) environment of the sample in the sample chamber. $n_{s'}$ is the modulated substrate refractive index due to the propagating strain pulse.

frequency[1] is calculated from

$$f = \frac{2\nu n}{\lambda}, \tag{5.3}$$

as the probe hits the sample under normal incidence, which is the case in all experiments reported in this thesis. The strain-modulated reflectivity is detected by the intensity modulation scheme described in section 4.3.

5.3 Experiment

A general overview of the experimental setup and technical essentials used for the studies is given in chapter 4. At this point, the attention should be drawn to the experimental modifications relevant to the investigation of qLA and qTA strain pulses in a high-index [311]-GaAs substrate. The sample consists of a 100 μm thick GaAs substrate cut along the [311] crystallographic axes. One side is covered with a 100 nm Aluminum film serving as the opto-elastical transducer. A scheme providing the currently discussed sample structure with experimental geometry is shown in figure 5.4. The optical axis z is set along the [311] direction of the GaAs substrate. The experiment is carried out at cryogenic temperatures ($5 - 10$ K). A femtosecond laser pulse serving as the pump beam is focused onto the Aluminum film. The local spot diameter on the transducer surface is 100 μm at full width at half maximum (FWHM) of the Gaussian shaped radial power distribution of the output laser beam. Here, excitation densities of $W = 4$ mJ/cm^2 are reached [75]. According to the picosecond

[1] The intensity oscillations are also called *Brillouin* oscillations because of the analogous calculation of the frequency shift in Brillouin scattering experiments.

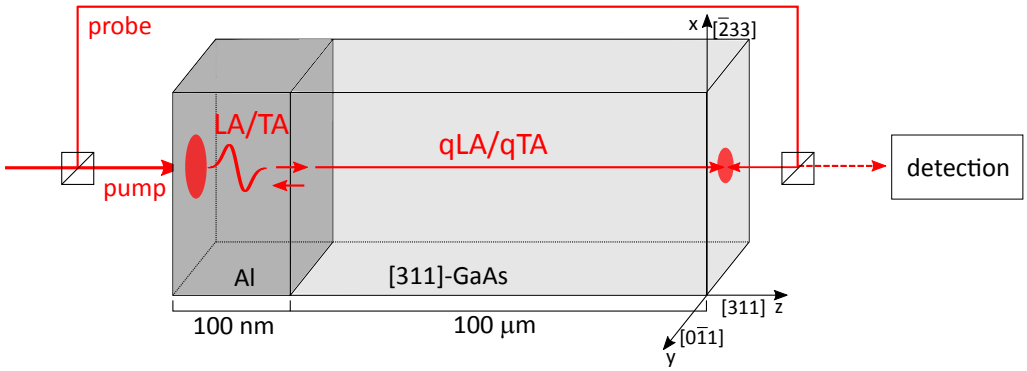

Figure 5.4: Experimental scheme of the propagation and detection of qLA and qTA strain pulses in [311]-GaAs. Pump and probe beam are split from the same laser source and directed onto the sample from opposite sides.

acoustics generation fundamentals demonstrated in chapter 3, a LA strain pulse is launched into the Aluminum film and propagates towards the opposite side of the film. The initial strain pulse launched into the Aluminum film is purely longitudinal propagating at the sound velocity $\nu_{\mathrm{LA}} = 6,3$ km/s. The bipolar strain profile can be approximated by the derivative of a Gaussian function [76]:

$$\eta_0(t - z/\nu_{\mathrm{LA}}) = \sqrt{e}\eta_{zz}^{\max}\frac{(t - z/\nu_{\mathrm{LA}})}{\tau} \cdot \exp\left(-\frac{(t - z/\nu_{LA})^2}{2\tau^2}\right). \tag{5.4}$$

The parameter τ defines the characteristic strain pulse duration and and e denotes the base of the natural logarithm. $\eta_{zz}^{\max}$ gives the maximum value of the η_{zz} component along the propagation direction z. It may be determined in dependence of the applied pump power W as $\eta_{zz}^{\max} = a_{\mathrm{W}} \cdot W$ with the coefficient $a_{\mathrm{W}} \approx 10^{-4}$ cm^2/mJ [21]. Figure 5.5 (a) displays the calculated temporal profile of the initial LA strain pulse $\eta_0(t)$ generated in the Aluminum film. The LA pulse travels through the isotropic transducer towards the interface of the transducer and the acoustically anisotropic [311]-GaAs substrate. The propagation of pure LA modes is not allowed along the [311] direction of the high index substrate. But contrary, mixed modes of qLA, qTA and a pure TA mode with different sound velocities $\nu_{\mathrm{qLA}} = 5,1$ km/s, $\nu_{\mathrm{qTA}} = 2,9$ km/s and $\nu_{\mathrm{TA}} = 3,5$ km/s [77] exist. Both qLA and qTA modes propagating in the substrate contain a shear component. Because of the continuity of the strain at the aluminum/GaAs interface this shear mode is also required in the aluminum film. Together with the initial LA pulse, the TA pulse travels through the aluminum film towards the open surface where they are reflected and propagate back through the

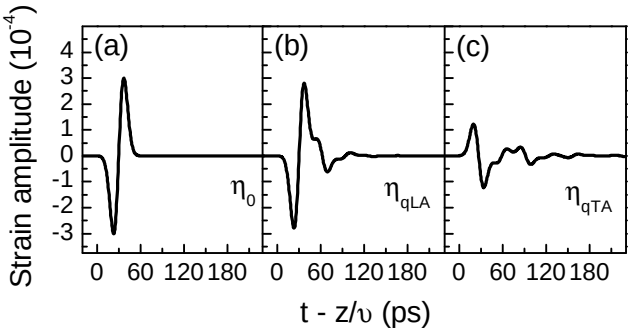

Figure 5.5: Temporal profiles of (a) the pure LA strain pulse $\eta_0(t)$ launched into the Aluminum transducer, (b) the qLA strain pulse η_{qLA} and (c) the qTA strain pulse η_{qTA} propagating along the [311] crystallographic direction in the GaAs substrate.

film towards the aluminum/GaAs interface with their individual sound velocities. At the interface both modes again contribute to the qLA and qTA pulses injected into the [311]-GaAs substrate. The unit displacement vectors of the different permitted polarizations in the [311]-GaAs read $\vec{e}_{\mathrm{qLA}} = \left(u_0, 0, \sqrt{1-u_0^2}\right)$, $\vec{e}_{\mathrm{qTA}} = \left(\sqrt{1-u_0^2}, 0, -u_0\right)$ and $\vec{e}_{\mathrm{TA}} = (0,1,0)$ with $u_0 = 0,165$ [77]. The mixed character of the qLA and qTA modes each consisting of LA and TA modes is obvious. They are both coupled to the pure longitudinal strain pulse initially generated in the Aluminum film. Since there is no coupling between the pure TA mode in [311]-GaAs and the initial LA mode, the pure TA strain pulse is not excited in the [311]-GaAs substrate. The related strain pulse components of the excited qLA and qTA strain pulses may be given as

$$\eta^p_{zz}(t,z) = e^p_z \eta_p(t - z/\nu_p), \tag{5.5}$$

$$\eta^p_{xz}(t,z) = \frac{1}{2} e^p_x \eta_p(t - z/\nu_p) \tag{5.6}$$

with p = qLA, qTA and $\eta_p(t - z/\nu_p)$ describing the temporal evolution of the strain pulses determined by the initial strain pulse. The calculated temporal profiles of the qLA and qTA strain pulses in the GaAs-substrate η_{qLA} and η_{qTA} are plotted in figure 5.5 (b) and (c)[1]. The amplitude of the longitudinal component of the qLA strain pulse reaches $2,8 \cdot 10^{-4}$. Both profiles display irregular additional features appearing as a tail in each signal. These features originate from the multiple reflections of the LA and TA strain pulses in the Aluminum transducer. The resulting temporal evolution governing the qLA strain pulse profile is determined by the initial pure LA pulse. In contrast, the qTA profile displays a much more mixed character resulting from a contribution of the shear component. The amplitude of the qTA strain

[1]Numerical calculations have been provided by T. Linnik, National Academy of Sciences of Ukraine, Kiev, Ukraine in [75].

pulse is approx. $1 \cdot 10^{-4}$ and 3 times smaller than the amplitude of the qLA pulse. Although, both acoustic modes are created simultaneously in one strain pulse the propagation of qLA and qTA pulses is separated in time because of their different sound velocities.
For the detection, a linearly polarized probe beam is focused to a spot of 50 μm-diameter at the substrate surface opposite to the metal transducer spatially overlapping with the pump beam spot. Due to the traveling time of the excited strain pulse the optical path way of the probe beam is adjusted by a retro-reflector in order to ensure temporal overlap of the strain pulse arriving time and the probe beam. Additionally, this path delay has to be adjusted related to the smaller sound velocity of the qTA strain pulse trailing the preceding qLA pulse in the substrate. From the difference in the traveling times the separated detection of the modes is ensured by the adjustment of the probe path way. For the sub-picosecond time resolution of each measurement a variable delay line is implemented in the pump beam path (see chapter 4).
In the experiments the modulation of the reflected probe pulse intensity $\Delta I(t)/I_0$ and the strain induced rotation of probe polarization plane $\Delta\psi(t)$ is measured. The intensity signal from the strain pulse $I(t)$ is normalized to the reflected probe intensity I_0 in absence of the strain pulse. The intensity of the reflected probe light is directed to one single photodiode of the balanced detector (see chapter 4). The traveling qLA and qTA strain pulses change the dielectric permittivity of the substrate so that the material becomes optically anisotropic [78]. Therefore, the signal detection depends on the polarization plane of the reflected probe beam. To monitor the strain induced rotation of the probe polarization plane the reflected probe beam is split into two orthogonally $s-$ and $p-$polarized beams which are focused to both photodiodes (see chapter 4) in order to record the differential signal. Both signals are measured for different polarization orientations $\psi_0 = 0, \frac{\pi}{4}, \frac{\pi}{2}, \frac{3\pi}{4}$ of the probe beam incident on the sample surface.

5.4 Theoretical analysis

This section provides an overview of the theoretical description[1] of the reflected probe intensity and polarization rotation characteristics. It substantiates the discussion of experimental results in the next section. All calculations are based on the assumption that the shape of the propagating strain pulse is constant and the strain is static. Propagating qLA and qTA pulses change the optical properties by perturbing the dielectric permittivity tensor ϵ of the GaAs substrate due to the elasto-optical effect [79]. The modification of the permittivity components ϵ_{ij} due to strain is given by

$$\delta\epsilon_{ij}(t,z) = \epsilon_0^2 p_{ijkl}\eta_{kl(t,z)} \tag{5.7}$$

[1] The theoretical framework sketched here, is provided in Ref. [75] in more details.

wherein ϵ_0 is the unperturbed dielectric permittivity and p_{ijkl} are the components of the photo-elastic tensor written in the [311]-coordinate system. Two components $\eta_{xz}(t,z), \eta_{zz}(t,z) \neq 0$ exist for the chosen geometry resulting in two permittivity components $\delta\epsilon_{xx}(t,z)$ and $\delta\epsilon_{yy}(t,z)$ with non-zero values. In high index substrates these deviations are not equal in value leading to optical anisotropy of the structure. The Maxwell equations with standard boundary conditions yield an expression for the amplitude of the electric field modulation in the reflected light wave δE according to

$$\delta E = \frac{ik_0^2}{(k+k_0)} \int_{-\infty}^{0} dz' e^{-ikz'} [\delta\epsilon_{jx}(t,z') E_x^0(z') + \delta\epsilon_{jy}(t,z') E_y^0], \quad j = x,y \tag{5.8}$$

with

$$\begin{aligned} E_{x,R}^0 &= \cos\psi_0 [\exp(-ik_0 z') + R_{\mathrm{EM}} \exp(ik_0 z')], \\ E_{x,T}^0 &= \cos\psi_0 T_{\mathrm{EM}} \exp(-ik_0 z'), \\ E_{y,R}^0 &= \sin\psi_0 [\exp(-ik_0 z') + R_{\mathrm{EM}} \exp(ik_0 z')], \\ E_{y,T}^0 &= \sin\psi_0 T_{\mathrm{EM}} \exp(-ik_0 z'), \end{aligned} \tag{5.9}$$

$$\tag{5.10}$$

for $z' > 0$ and $z' < 0$ respectively. ψ_0 denotes the angle between the incident light polarization and the x-axis, R_{EM} and T_{EM} are the complex reflection and transmission coefficients. The complex wave number of the light is given by $k = nk_0 + i\gamma$ in the substrate and $k = 2\pi/\gamma$ in vacuum with 2γ denoting the absorption coefficient. From equation (5.8) the expressions for the relative strain induced perturbation of the reflected probe-pulse intensity and the polarization plane rotation can be extracted:

$$\frac{\Delta I(t)}{I_0} \propto Re\left\{ \int_{-\infty}^{0} dz \exp(-2ikz) \left[\delta\epsilon_{xx}(t,z) + \delta\epsilon_{yy}(t,z) + [\delta\epsilon_{xx}(t,z) - \delta\epsilon_{yy}(t,z)] \cos 2\psi_0\right] \right\}. \tag{5.11}$$

and

$$\Delta\psi(t) \propto Re\left\{ \int_{-\infty}^{0} dz \exp(-2ikz) [\delta\epsilon_{yy}(t,z) - \delta\epsilon_{xx}(t,z)]. \right\} \tag{5.12}$$

Using the known parameters for the photoelastic constants in GaAs allows for the direct expressions for the dielectric permittivity perturbations [80] dependent on both, η_{xz} and η_{zz}:

$$\delta\epsilon_{xx}(t,z) + \delta\epsilon_{yy}(t,z) = -7,6\eta_{xz}(t,z) + 29\eta_{zz}(t,z), \tag{5.13}$$

$$\delta\epsilon_{xx}(t,z) - \delta\epsilon_{yy}(t,z) = 2,9\eta_{xz}(t,z) + 1,8\eta_{zz}(t,z). \tag{5.14}$$

The solutions of eq. (5.11) and eq. (5.12) using eqs. (5.13) and (5.14) lead to the form

$$\begin{aligned}\frac{\Delta I_{\mathrm{qLA}}(t)}{I_0} &= [28 - 1,5\cos(2\psi_0)]Q_{\mathrm{qLA}}(t),\\ \frac{\Delta I_{\mathrm{qTA}}(t)}{I_0} &= [-8,5 + 1,7\cos(2\psi_0)]Q_{\mathrm{qTA}}(t),\end{aligned} \tag{5.15}$$

for the intensity modulation and

$$\begin{aligned}\Delta\psi_{\mathrm{qLA}}(t) &= 0,75\sin(2\psi_0)Q_{\mathrm{qLA}}(t),\\ \Delta\psi_{\mathrm{qTA}}(t) &= -0,85\sin(2\psi_0)Q_{\mathrm{qTA}}(t),\end{aligned} \tag{5.16}$$

for the rotation of polarization. The functions Q_{qLA} and Q_{qTA} yield the absolute value and phase of the spectral amplitude at the Brillouin frequencies f_{qLA} and f_{qTA}. The pre-factors in eq. (5.15) and eq. (5.16) determine the angular dependencies of the detected signals. For $\psi_0 = \pi/2$ corresponding to the prope pulse orientation parallel to the $[\bar{2}33]$ or $[0\bar{1}1]$ direction the polarization rotation signal should be zero whereas maximal signal amplitudes should be reached at $\psi_0 = (2n+1)\pi/4, n = 0, 1, 2...$.
The probe pulse intensity signal $\frac{\Delta I(t)}{I_0}$ is minimal for $\psi_0 = 0, \pi$ and reach maximum values for $\psi_0 = \pi/2, 3\pi/2$ whereas the angle dependence is presumed to be much weaker as expected for polarization rotation measurements (compare eq. (5.15)).

5.5 Results and discussion

Figure 5.6 (a) and (b) show the intensity modulation $\Delta I/I_0$ of the reflected probe beam for qLA and qTA strain pulse excitation. The time window is limited to the range when the signals are observed. $t = 0$ corresponds to the time when the pump pulse hits the the aluminum transducer. Both signals show pronounced sinusoidal Brillouin oscillations with a symmetric envelope function. The maximum amplitude in both signals corresponds to the time when the center of the strain pulse traveling from the Aluminum transducer reaches the open GaAs substrate surface. At the substrate/air interface, the strain pulse is reflected with a phase shift of $\pi/2$ and propagates back into the material. The overall time duration of the signals is governed by the penetration depth (ca. 2 μm) of the probe light and the time the strain pulse needs to propagate towards the open GaAs surface and back into the substrate within the penetration depth. The total time duration of the signal corresponding to the qTA strain pulse is nearly twice longer than the qLA signal duration due to the slower qTA strain propagation velocity. The frequency spectra calculated from both signals are displayed in figure in the insets. The Brillouin frequencies are centered around 46 GHz for qLA and 27 GHz for qTA excitations. From these frequency spectra, the sound velocities for both acoustic modes can be extracted from equation

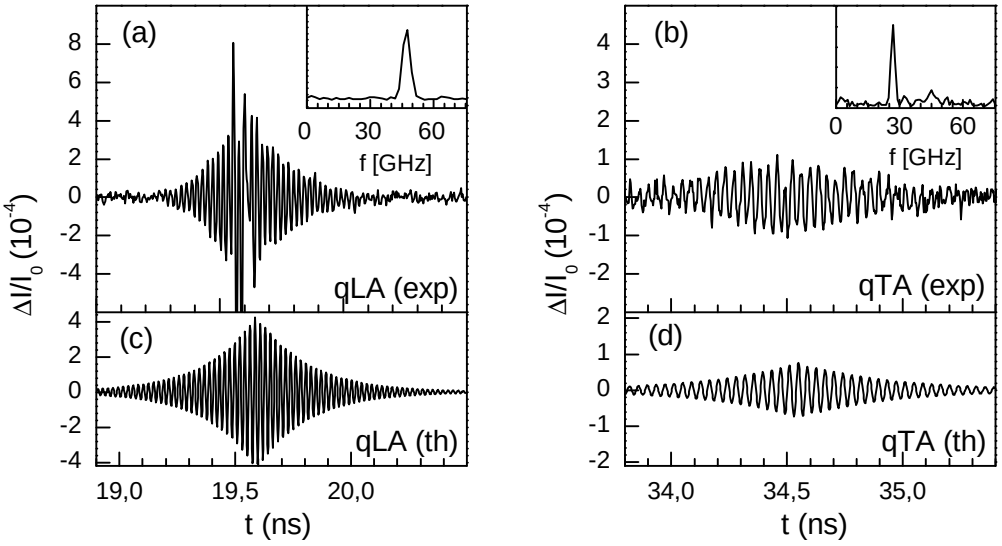

Figure 5.6: Panel (a) and (b): Intensity modulation signals $\Delta I_{qLA}(t)/I_0$ and $\Delta I_{qTA}(t)/I_0$ measured for the propagation of qLA and qTA strain pulses. Panel (c) and (d): Theoretically calculated intensity signals for both qLA and qTA.

(5.3) yielding $\nu_{\mathrm{qLA}} = 5,2$ km/s and $\nu_{\mathrm{qTA}} = 2,8$ km/s. They are in good agreement with values found in literature [77]. Therefore, the correspondence of each signal shown in figure 5.6 to one specific acoustic mode (i.e. qLA or qTA) evidences the isolated detection. The amplitude of the qLA intensity modulation signal appears to be about five times larger than the amplitude of the qTA oscillations. The panels (c) and (d) show the Intensity signals $\Delta I_{qLA}(t)/I_0$ and $\Delta I_{qTA}(t)/I_0$ calculated theoretically using the functions (5.15). For both acoustic modes, the theoretically determined curves are in good accordance with the experimentally measured signals. The experimental data for $\Delta I_{\mathrm{qLA}}(t)/I_0$ shows several peculiarities featuring narrow peaks and dips around $t = 19,6$ ps which may be attributed to non-linear effects like the formation and propagation of solitons accompanying the propagation of the compressive strain pulse. The effect of soliton formation to the strain pulse dynamics is omitted in the theoretical calculations. The calculated intensity modulation in equation (5.15) predicts a weak dependence of $\Delta I(t)/I_0$ on ψ_0 through the anisotropic polarization-dependent term. Therefore, polarization rotation measurements have also been performed in the single diode scheme, monitoring the intensity signal for different probe polarization angles. The maximal intensity modulation should be detected for $\psi_0 = \pi/2$ or $\psi_0 = 3\pi/2$. Measurements revealed a maximal amplitude changes in $\Delta I(t)/I_0$ at different angles less than $2 \cdot 10^{-5} I_0$. Therefore, the influence

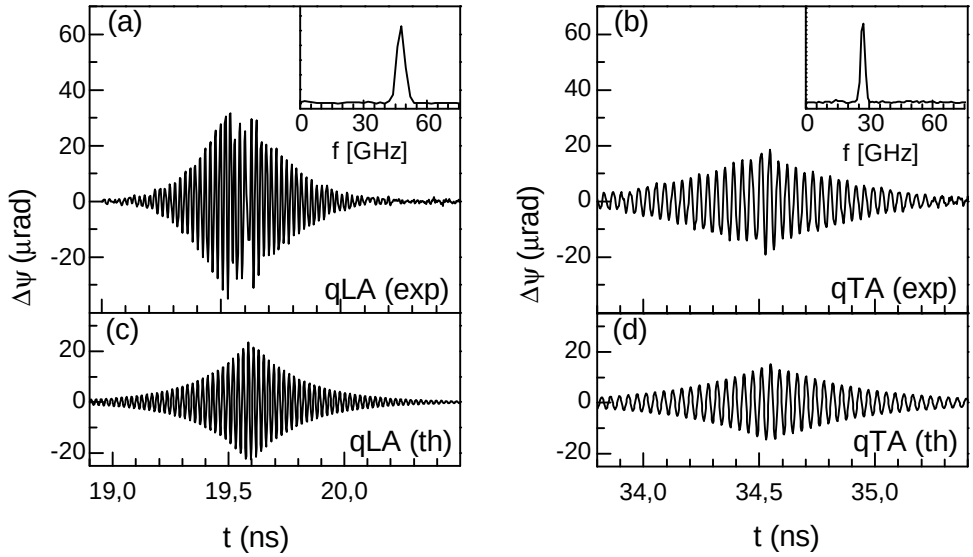

Figure 5.7: Change of the polarization angle $\Delta\psi(t)$ measured at different propagation delays for qLA and qTA strain pulses. Calculated signals for $\Delta\Psi_{qLA}$ (c) and $\Delta\Psi_{qTA}$

of the polarization rotation on the intensity modulation cannot be resolved in the detection system.

Measurements in the balanced detection scheme provide the modulation of the probe polarization plane for different delays according to qLA and qTA modes. Data plots are shown in figure 5.7 (a) and (b) for qLA and qTA respectively. The signals show the similar oscillatory behaviour as observed in the intensity modulation measurements. Both plots show Brillouin oscillations at $f_{\mathrm{qLA}} = 46$ GHz and $f_{\mathrm{qTA}} = 27$ GHz with a signal envelope attributed to the penetration depth of the probe light. Here, the laser light is directed to both diodes. Consequently, the signal to noise ratio is improved because of the subtracted background compared to the measurements in the single diode mode. This has a large impact on the pronouncing of the qTA signal. The polarimetric signal amplitudes of qTA and qLA lie in the same order of magnitude.

In order to investigate the polarimetric signals in dependence of the probe polarization angles, figure 5.8 presents an overview of polarization rotation measurements at different ψ for both acoustic modes. The probe polarization axis parallel to the crystallographic direction of $[\bar{2}33]$ of the [311]-GaAs structure has been chosen as the reference polarization angle ψ_0. Starting from this configuration it is convenient

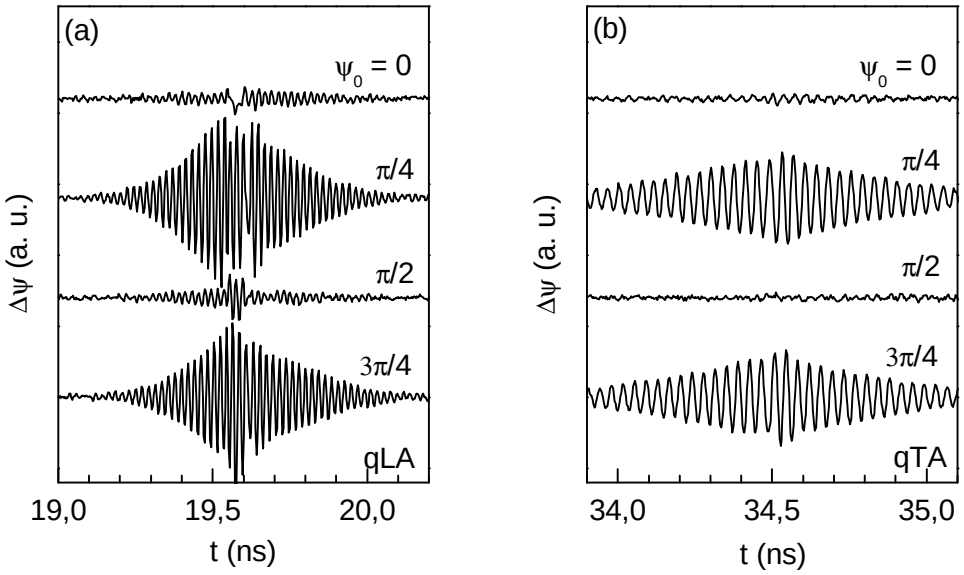

Figure 5.8: Polarimetric Brillouin oscillation signals $\Delta\psi(t)$ for different orientations of the probe polarization plane measured for qLA (Plot (a)) and qTA (Plot (b)) strain pulses separately.

either to turn the sample around its azimuthal axis or to rotate the polarization plane of the probe beam before incident on the sample surface. In the experimental results presented in figure 5.8 the polarization rotation of the probe beam has been measured for four different polarization angles $\psi_0 = 0(\equiv [\bar{2}33]), \pi/4, \pi/2(\equiv [0\bar{1}1])$ and $3\pi/4$. The Brillouin scattering signals for qLA and qTA are hardly observed for the probe polarization plane parallel to the $[0\bar{1}1]$ and the $[\bar{2}33]$ crystallographic axes of the [311]-GaAs substrate. For both intermediate alignments of the polarization plane pronounced signal amplitudes are observed which are of the same magnitude for both acoustic modes. These results assume a strong dependency of the polarimetric signal on the orientation of the probe polarization plane as it has been predicted in the theoretical calculation of eq. (5.16), in the last section.

5.6 Conclusion

This chapter provided an overview of the generation and detection of quasi-longitudinal and quasi-transverse acoustic strain pulses in a high-index [311]-GaAs substrate within the scope of picosecond acoustics.
Low symmetry substrates allow the simultaneous generation of qLA and qTA strain

pulses induced by femtosecond laser pulses by means of a metallic opto-acoustic transducer. Due to their different sound velocities the acoustic modes segregate during propagation through the substrate. Thus, probing the interferometric signal opposite to the strain pulse excitation the separated detection of both modes is realized. The monitored intensity modulation $\Delta I_{\mathrm{qLA}}(t)/I_0$ and $\Delta I_{\mathrm{qTA}}(t)/I_0$ of the reflected probe beam at different time delays corresponding to the propagation time of qLA and qTA strain pulses yield Brillouin oscillations. The lower amplitude of the qTA signal may mainly be attributed to the weaker excitation of the qTA strain pulse that may be extracted from the temporal strain pulse profiles $\eta_{\mathrm{qLA,qTA}}(t,z)$ in figure 5.5 (c). The sensitivity of the qTA pulse detection is improved by using the polarimetric technique. This balanced detection scheme provides a more pronounced detection of especially qTA strain pulses due to the improved signal to noise ratio (see figure 5.7). The strong dependence of the polarimetric signal on the probe polarization plane as shown in figure 5.8 illustrates the optical anisotropy of the GaAs structure induced by the strain pulse. A detailed theoretical examination of $\Delta\psi_{\mathrm{qLA}}$ and $\Delta\psi_{\mathrm{qTA}}$ found in Ref. [75] determines the angular dependencies of the polarization rotation signals. The solutions based on numerical calculations of the Maxwell equations predict the absence of signals when the probe polarization plane is parallel to the $[\bar{2}33]$ and $[0\bar{1}1]$ crystallographic axes and strong Brillouin oscillations for intermediate orientations. These theoretical results are in accordance with the experimental observations. The excitation and increase of the qTA strain pulse induced interferometric and polarimetric signals allows for extended investigations of magnetization modulation experiments in ferromagnetic materials, shown in the following chapters of this work.

6 Strain-induced magnetization modulation in nanometer Galfenol films

This chapter provides a detailed presentation of the main experimental results of this work regarding the strain-governed magnetization modulation in nanometer Galfenol films. Recently, the strain-induced magnetization precession on picosecond time scales has been demonstrated in the semiconductor GaAs doped with Manganese atoms [22, 23] and detailed theoretical modeling of this effect has been provided by T. Linnik et al. in Ref. [29]. However, beside technical limitations, the GaMnAs structure implicates obvious disadvantages: due to its rather low Curie temperature of 60 K, experiments are restricted to cryogenic temperatures. Moreover, the saturation magnetization of approx. 10 mT in GaMnAs is rather low, and thus, the resulting dynamical effects are extremely weak for possible applications. With the development of giant magnetostrictive materials like Galfenol, that combines strong ferromagnetic properties with large magnetostriction coefficients, the coupling of external strain to the magnetic anisotropy is assumed to result in much stronger effects even at the picosecond time scales. Furthermore, displaying a Curie temperature up to 600 °C Galfenol is suitable for experimental investigation at room temperature and therefore, a promising structure in the view of future applications.
This chapter starts with the characterization of the relevant experimental properties of the sample structures under study. In the second section, the first demonstration of magnetization precession induced by LA strain pulses in high symmetry Galfenol samples at cryogenic temperatures will be presented. Dynamical signals measured in samples with different thicknesses will be compared, followed by the demonstration of spin wave excitations. In the following section, the excitation of magnetization precession will be extended via application of shear strain pulses in a high index [311]-Galfenol sample. The discussion and analysis of the experimental results is supported by the theoretical formalism established in [28]. Lastly, it will be shown that the magnetization modulation by means of picosecond acoustics in a thin ferromagnetic Galfenol layer can also be monitored at ambient temperatures.

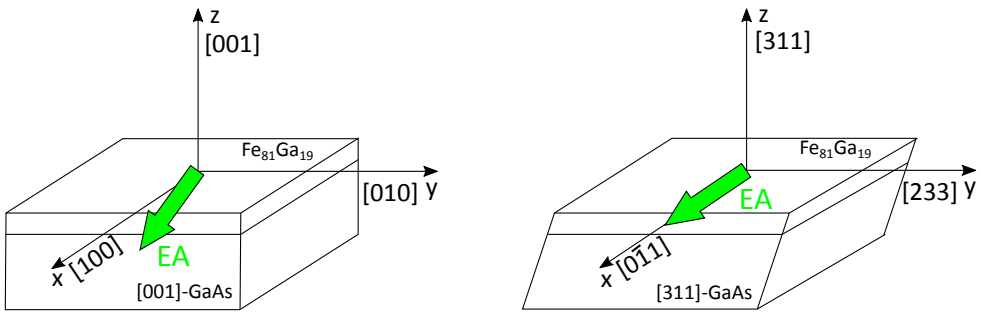

Figure 6.1: Crystal symmetry conditions of both different sample compositions used: The structure of both 20 nm and 100 nm Galfenol films deposited on 100 μm thick $[001] - GaAs$ substrate displays the EA of magnetization in the (001)-layer plane directed between the main crystallographic axes [100] and [110] (left). The EA of the 100 nm Galfenol layer grown on [311]-GaAs is oriented along the [0$\bar{1}$1] lattice direction (right).

6.1 Sample characterization

This section provides a condensed overview of all relevant experimental properties of the ferromagnetic samples under study. Beside the metrics and composition the focus will be on illustration of structural and magnetic characteristics. The $Fe_{81}Ga_{19}$ layers are grown by DC magnetron sputtering from a composite target onto the GaAs substrates as shown in chapter 2.3. Detailed X-ray diffraction studies reveal that the samples can be described by a mosaic model in which the film is formed from Galfenol crystallites, each with a cubic crystal structure, but randomly oriented. The mean size of the mosaic blocks of about (4.5 ± 0.5) nm and the root-mean square misorientation of the blocks is (7 ± 2) degrees. This small misorientation angle of the mosaic blocks leads to magnetic properties close to those observed for single crystal films, including a bulk-like magnetostriction and cubic magnetocrystalline anisotropy [45]. Three samples with different structural symmetry conditions are used for the experiments. Two samples are grown on [001]-GaAs: One layer of $Fe_{81}Ga_{19}$ with 100 nm thickness is coated with a 2 nm aluminum cap in order to protect the material from oxidation. The other layer on a [001]-GaAs substrate has a thickness of 20 nm and a cap of 120 nm SiO_2 on top. The silicon dioxide cover is fabricated onto the ultra thin layer in order to shift the open surface where the strain pulse amplitude vanishes to zero.
The third sample structure is composed of a 100 nm $Fe_{81}Ga_{19}$ layer grown on a high-index [311]-GaAs substrate. Just like the 100 nm FeGa on [001]-GaAs sample the

layer is also covered with a 2 nm aluminum cap for reasons of corroding processes. Figure 6.1 demonstrates the underlying crystallographic axes and the orientation of the easy magnetization axes of the different sample structures. (The abbreviated sample labels are defined as [001]-GaAs-substrate + Galfenol-film ≡ [001]-FeGa/Galfenol and [311]-GaAs-substrate + Galfenol-film ≡ [311]-FeGa/Galfenol in the following.) The magnetic anisotropy parameters of the Galfenol films has been determined experimentally with a superconducting quantum interference device (SQUID)[1]. All samples display the easy axes of magnetization (EA) in the layer plane. Both Galfenol layers on the [001]-GaAs substrate reveal an in-plane anisotropy i.e. a superposition of a cubic term setting the [100]/[010] direction as the energetically favourable axis and an uniaxial term favouring the [110] direction [81],[82]. For the Galfenol film deposited on the [311]-GaAs substrate the easy axis coincides with the $[0\bar{1}1]$ direction [83].
The saturation magnetization of the ferromagnetic films is determined by steady state magnetization curves under static conditions to $\mu_0 M_0 = 1,8$ T. The value of $\mu_0 M_0$ is used in the following to norm the magnetization precession signals. The underlying GaAs substrates have a thickness of 100 μm. Opposite to the Galfenol film, a 100 nm thick aluminum transducer is evaporated on every GaAs substrate. The total size of each sample cut out from a wafer is about 5x5 mm.

6.2 Magnetization precession induced by longitudinal strain pulses

A first demonstration of picosecond strain induced high frequency magnetization precession will be presented in the two high symmetry $Fe_{81}Ga_{19}$ films of 100 nm and 20 nm thickness. By means of intensity signals and magneto-optical Kerr measurements the effect of longitudinal strain pulses on the ferromagnetic layer will be characterized in regard to the phenomenological approach of magnetization excitation given in section 4.1. During the fabrication process of the Galfenol wafer, the edges are clamped to holders, so that some defined spots of the wafer remain galfenol-free. The details of the experimental setup used for the measurements reported here, have been already discussed in section 4.2. All experiments are carried out at cryogenic temperatures up to 20 K. An optical pump beam with an excitation density of 20 mJ/cm^2 is incident on the surface of the aluminum transducer opposite to the Galfenol film. The injected strain pulse propagates through the GaAs substrate towards the Galfenol film. The launched strain pulse has pure longitudinal (LA) polarization and propagates at a sound velocity of $\nu_{\mathrm{GaAs,LA}} = 4,8$ km/s through the [001]-GaAs-substrate. The ferromagnetic Galfenol layer is reached after a corresponding propagation time of 21 nm. The probe beam incident on the Galfenol film surface has an excitation

[1] All Galfenol samples with structural characterization have been provided by A. Rushforth, University of Nottingham, Nottingham

density of 20 μJ/cm^2. After being reflected from the film surface the probe light is directed to the detection scheme. In order to check the technical alignment of the experimental setup intensity signals measured from a GaAs substrate which have been already discussed in chapter 5 have been reproduced from measurements at the galfenol-free surface spots (which display only the underlying GaAs substrate) from the [001]-FeGa samples before starting the investigation of the Galfenol film. Similar Brillouin signals have been obtained from these spots as plotted in figure 5.6 (a).
The intensity signal $\Delta I(t)/I_0$ of the reflected probe beam measured from the Galfenol film is shown in figure 6.2 (a) for a long time interval and in the inset as a zoom-in. The signal displays a broad dip with a time duration of approx. 100 ps. $t = 0$ defines

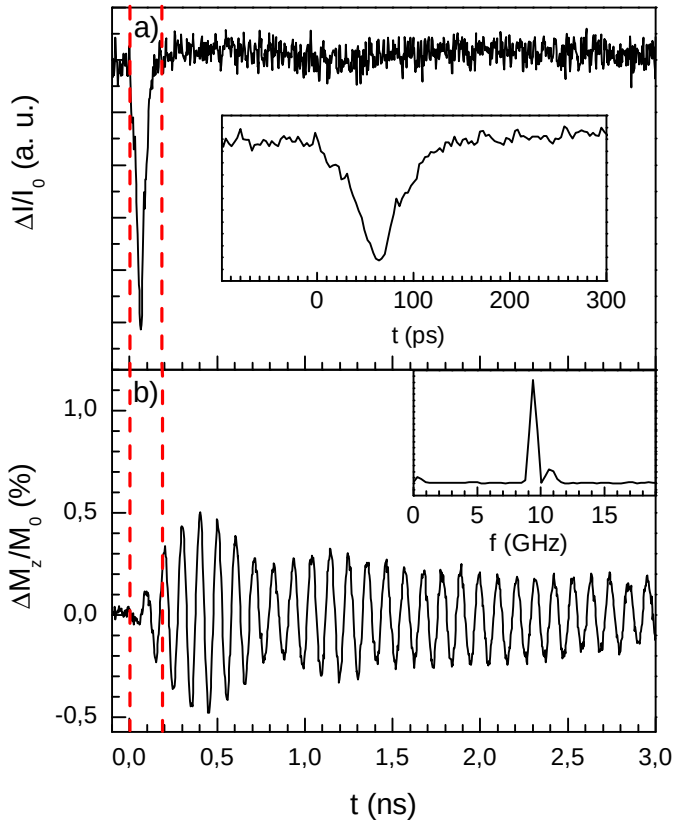

Figure 6.2: (a): Intensity signal $\Delta I(t)/I_0$ of the reflected probe beam displayed for a time range of 3 ns and zoomed into a ps time window. (b): Kerr rotation signal of the [001]-FeGa sample measured at an external magnetic field of $\mu_0 H_{ext} = 2,1$ T ($H_{\text{ext}}||z$). ΔM_z is normalized to the saturation magnetization M_0. The corresponding frequency spectrum may be extracted from the inset.

the time when the strain pulse has reached the Galfenol layer. Unlike the intensity

signals measured from GaAs spots the reflected probe intensity from the Galfenol film shows no Brillouin oscillations. The absence of the Brillouin signal mainly results from the very narrow absorption length of the laser light in the material. Nevertheless, $\Delta I(t)/I_0$ allows extracting information about the temporal evolution of the strain pulse. The duration of the acoustic wave packet in the Galfenol layer may be determined from the layer thickness d_{FeGa}, the sound velocity of the longitudinal acoustic wave ν_{LA} and twice the spatial strain pulse length of approx 40 ps to $t = \frac{d_{\mathrm{FeGa}}}{\nu_{\mathrm{LA}}} + 80\ \mathrm{ps} = 100\ \mathrm{ps}$. This time range fits well to the measured time duration of $\Delta I(t)/I_0$. This evidences that the measured intensity signal is a result of the effect of the propagating strain pulse. The signal also displays contributions from possible electron relaxation phenomena and thermal effects [49, 84]. The signal duration also serves as a reference of the time range in which strain pulse induced signals are commensurable. It is independent of the external magnetic field.

The discussion of a typical Kerr rotation signal from the [001]-FeGa sample shall emphasize the concept of magnetization modulation induced by picosecond strain pulses discussed in chapter 4.1 phenomenologically. Figure 6.2 (b) shows the polarization rotation of the reflected probe beam measured in the balanced diode system by means of the magneto-optical Kerr rotation (see chapter 4, section 4.3) at an external field of 2,1 T applied parallel to the z-direction. The Kerr rotation angle θ_{K}, meaning the angle of the rotation of the reflected probe polarization away from its initial polarization direction relates directly to changes of the component $M_z = M\cos(\theta)$ of the layer magnetization $\vec{M}$. Thus, the relative amplitude of the measured magnetization curves presented in this thesis is given by $\Delta M_z(t)$, normalized to the saturation magnetization M_0.
Ignoring detail features of the signal by now, the focus should first be drawn to the pronounced and long lasting oscillations governing the time evolution of $\Delta M_z/M_0$. No signal is observed until the strain pulse hits the layer at $t = 0$. An oscillatory motion builds up when the strain pulse hits the layer. The maximum signal amplitude reaches approx $0,5$ % of the saturation magnetization. The oscillations last for several ns until the motion damps. The signal remains much longer than the strain pulse duration in the layer itself and is also still present when the strain pulse has left the layer already. This is convincing by comparison of the signal durations in (a) and (b) where the intensity signal duration is indicated by dashed vertical (red) lines. The inset of plot 6.2 (b) displays the corresponding frequency spectrum of the oscillations with a frequency maximum around 9 GHz. This frequency value fits well to typical results found in Ferromagnetic Resonance (FMR) experiments from $Fe_{81}Ga_{19}$ structures [45, 85]. Therefore, this first observation of long lasting oscillations is indeed attributed to magnetization precession in the Galfenol layer. To ensure that the observed signal is not a result of the heat pulse (the flux of incoherent phonons) generated in the heated Aluminum film together with the coherent strain pulse generation a simple check of the experimental setup is done: Monitoring

the Kerr rotation signal when the overlap of the pump and probe laser spots from the opposite sides is slightly shifted, the signal disappears. If the tilt in magnetization would be induced by the incoherent heat pulse the coherent signal should be still observable even when both laser spots do not coincide completely due to the broad isotropic propagation of the heat pulse [86].
In the following, the spectrum of magnetization precession will be investigated for various external magnetic field strengths. Figure 6.3 (a) depicts polarization rotation signals of the [001]-FeGa sample measured at external magnetic fields with field orientation parallel to the $\vec{z}$-direction and values for $\mu_0 H_{\text{ext}}$ ranging from zero to $2,7$ T. The pump laser excitation density for the LA strain pulse excitation is $W = 20$ mJ/cm^2. At zero field almost no signal is observable. In this case the layer magnetization lies in the layer plane. In the range of $0 < \mu_0 H_{\text{ext}} < 1,8$ T, precession signals with time durations not longer than 1 ns appear. Between 1,9 and 2,4 T long lasting magnetization precession signals with increased time durations of several ns are observable. Exceeding $2,4$ T the MOKE signal vanishes. For such high fields the effective field $\vec{H}_{\text{eff}}$ is aligned almost parallel to $\vec{H}_{\text{ext}}$ and the modulation of M_z is no longer resolvable. Therefore, the tilting effect of the acoustic strain pulse on the magnetization followed by the precessional motion is monitored in the range of $0 < H_{ext} < 2,4$ T when $\vec{H}_{\text{eff}}$ is oriented along an intermediate direction between two extrema of the magnetic free energy. After the strain pulse hits the Galfenol layer it changes the parameters of the magnetic anisotropy via magneto-elastic coupling. Thus, the effective field $\vec{H}_{\text{eff}}$ is tilted from its initial equilibrium orientation and subsequently, $\vec{M}$ starts to precess around the new orientation of $\vec{H}_{\text{eff}}$. This condition is fulfilled for external field strengths large enough to turn $\vec{H}_{\text{eff}}$ away from the in-plane direction of the EA. The limit of field strength is reached when $\mu_0 H_{\text{ext}}$ is too high so that $\vec{H}_{\text{eff}}$ is aligned almost parallel to the direction of $\vec{H}_{\text{ext}}$. The maximum precession amplitude of $\Delta M_z(t)/M_0$ in dependence of $\mu_0 H_{\text{ext}}$ is plotted in figure 6.3 (b). The largest signal amplitude is reached at an intermediate field strength of $\mu_0 H_{\text{ext}} = 2,1$ T. Moreover, the precession signals at $1,8 < \mu_0 H_{ext} < 2,4$ T display pronounced beatings in the oscillatory motion. The beating seen in the time domain of magnetization modulation of these signals reflects in each corresponding frequency spectrum plotted in figure 6.3 (c). Each spectrum shows two spectral lines with a frequency splitting of 2 GHz. The appearance of the beating is attributed to the excitation of *spin wave* modes. By now, a uniform magnetization precession has been assumed. This corresponds to a collective coherent precession of the parallel aligned layer spins. Considering a minimal misorientation between neighbouring spins extended over a long range larger than the lattice constant forms an excited state of wave character called spin wave. As the parallel coherent precession of all spins in phase is referred to the ground state, the propagating disturbance in the magnetic order of the ferromagnetic structure represents the excited state of a spin wave mode also known as magnons in the picture of quasi particles. The first demonstration of spin wave excitation in a ferromagnetic GaMnAs structure via picosecond acoustics can be found

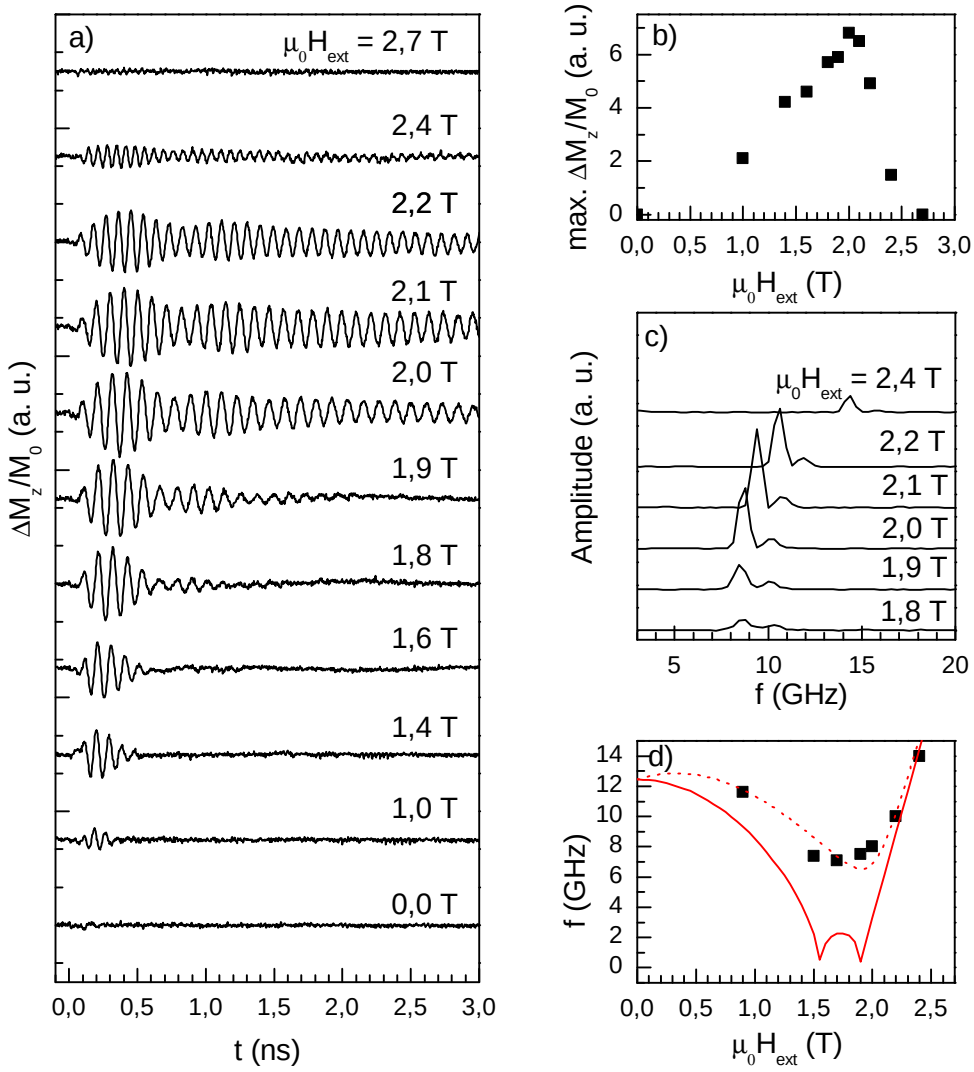

Figure 6.3: (a): Strain pulse induced changes of M_z measured at various external magnetic fields ranging from $\mu_0 H_{\text{ext}} = 0$ T to $\mu_0 H_{ext} = 2,7$ T in the [001]-FeGa sample. (b): Maximum signal amplitude of $\Delta M_z(t)/M_0$ in dependence of $\mu_0 H_{\text{ext}}$. (c): Corresponding frequency spectra calculated for the signals from 1,8 to 2,4 T. (d): Fundamental precession frequency (squares) plotted as a function of $\vec{H}_{\text{ext}}$. Solid and dashed red lines: Theoretically calculated frequency dependence.

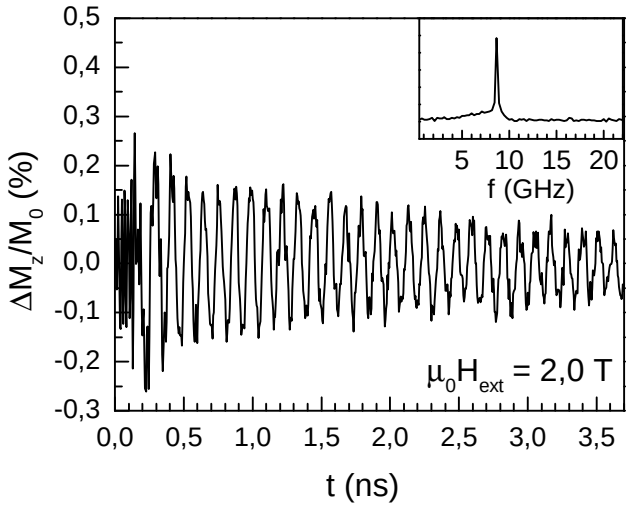

Figure 6.4: Kerr rotation signal measured from the ultra thin [001]-FeGa 20 nm thick film in an external field of $\mu_0 H_{\text{ext}} = 2$ T oriented parallel to the $\vec{z}$ axis. The frequency spectrum is shown in the inset.

in an earlier work [87]. The basic condition to excite spin wave modes via picosecond acoustics is the matching of the spatial profile of the spin wave and the spectral component of the strain pulse at the same frequency, given by their spatial overlap integral. Thus, the excitation efficiency varies with the film thickness which is modulated by the propagating strain pulse. In the magnetization modulation experiments in GaMnAs it has been shown that spin waves may be excited selectively when the broad phonon spectrum of the strain pulse matches the spin waves frequencies. The frequency spectrum and the initial phase of the spin wave excitations depend on the magnetic boundary conditions meaning the spin properties at the sample interfaces. These might be expressed by the surface magnetic energy but still a matter of debate for Galfenol and therefore, beyond the scope of this work. Precession dynamics at external fields lower than $1,8$ T display no frequency splitting. The absence of spin waves here is of an artificial nature because the signals in the time domain are very short and the frequency pattern therefore, hardly to resolve. Figure 6.3 (d) displays the frequency spectrum (squares) of the fundamental mode in dependence of H_{ext} yielded from magnetization precession curves in figure 6.3 (a). Dashed and solid red curves refer to a theoretical calculation of the spectrum which will be discussed later. The measurement points reveal a rather complicated relation of the frequency on the external field. The maximum precession frequency of 14 GHz is reached at $\mu_0 H_{\text{ext}} = 2,4$ T.

Next, the magnetization modulation in the ultrathin (20 nm) Galfenol film grown on [001]-GaAs will be examined. The Kerr rotation signal in dependence of the time delay between pump and probe in an external magnetic field of $2,0$ T oriented parallel

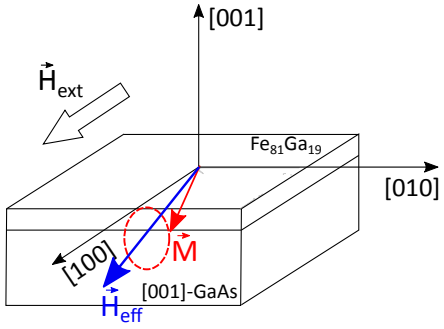

Figure 6.5: Sketch of the strain induced magnetization precession of $\vec{M}$ around $\vec{H}_{\text{eff}}$ at the in-plane orientation of ($\vec{H}_{\text{ext}} \perp \vec{z}$).

to the $\vec{z}$-axis is plotted in figure 6.4. The measurement has been taken at the same excitation density for pump and prove as in the 100 nm film. The time evolution provides an even larger decay time longer than $3ns$ compared to the 100 nm sample. In the corresponding frequency spectrum plotted in the inset of figure 6.4 only one narrow spectral line is observable. A single fundamental spin wave mode is assumed to be excited in this ultrathin film. Due to the film thickness of only 20 nm the dynamical strain pulse is supposed to be almost constant inside the layer. Thus, the spatial overlap of the higher spin wave modes modulated along the z-direction and the strain pulse frequency components becomes negligible. Excited spin wave modes are therefore not generated in this sample.

To this point, the magnetization modulation in the [001]-FeGa layer has been excited in an external field applied parallel to the $\vec{z}$ axis, perpendicular to the sample surface ($\vec{H}_{\text{ext}} || z$). Magnetization modulation experiments may also be performed in a different geometrical arrangement when the external magnetic field is applied parallel to the layer plane i.e. in-plane and perpendicular to the $\vec{z}$ axis ($\vec{H}_{\text{ext}} \perp z$). A sketch of the sample orientation and axes definition given in figure 6.5 shall illustrate the concept of magnetization modulation in this experimental geometry. Here, $\vec{H}_{\text{ext}}$ is aligned parallel to the [100] symmetry axis of the layer. The resulting effective field $\vec{H}_{\text{eff}}$, the sum of the intrinsic magnetic anisotropy field and external field $\vec{H}_{\text{ext}}$, orientates in the layer plane. The strain pulse arriving at the interface to the layer tilts $\vec{H}_{\text{eff}}$ maintaining its in-plane orientation. In this geometry, several magnetization precession signals $\Delta M_z(t)/M_0$ have been recorded and are displayed in figure 6.6 (a). The signals are measured for $\vec{H}_{\text{ext}} \perp \vec{z}$ ($\vec{H}_{\text{ext}} || [100]$) at field strengths varying from 0 to 500 mT. The longest signal duration of $t \approx 450$ ps is observed at $\mu_0 H_{\text{ext}} = 300$ mT. Plot (b) shows the precession frequency dependence on H_{ext} for this in-plane geometry. The frequency increases continuously with the ramped external field until maximum values of $30-35$ GHz are reached. Comparing the field dependences of the precession frequencies yielded for both, the perpendicular and in-plane orientation of $\vec{H}_{\text{ext}}$, twice higher precession frequencies and a totally different pattern of the spectral peak positions is observed at in-plane geometry. In section 6.4, a detailed discussion

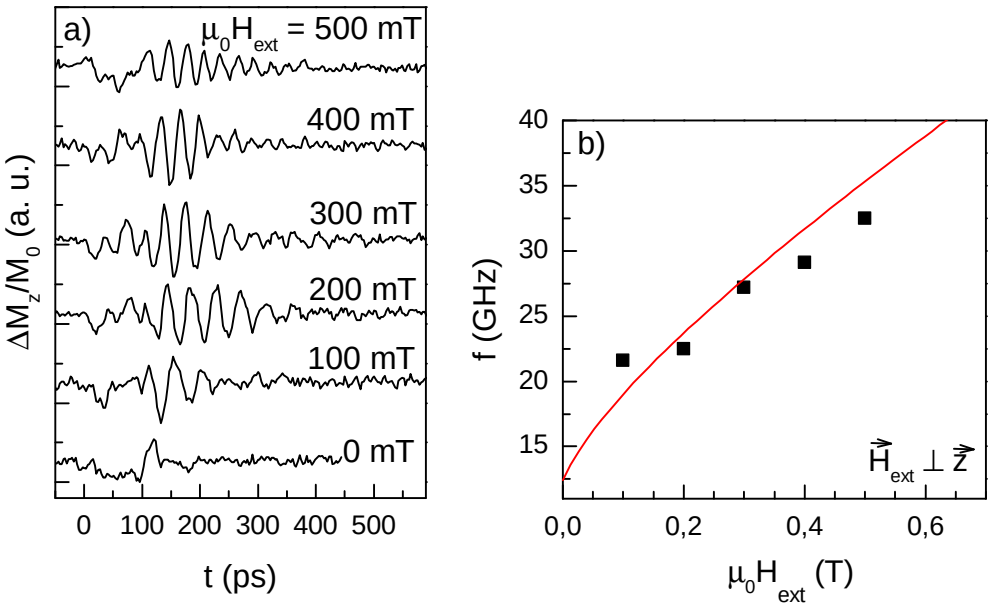

Figure 6.6: (a) Magnetization precession signals $\Delta M_z(t)/M_0$ measured at an in-plane orientation of the external field $\vec{H}_{\text{ext}}||[100]$. (b) Corresponding fundamental frequency lines in dependence of the external field strength (squares).

based on theoretical calculations of the precession frequency behaviour will underline these experimental results.

6.3 Magnetization modulation induced by shear strain pulses

In the last section, magnetization excitation in thin Galfenol layers grown on [001]-GaAs substrates by longitudinal acoustic strain pulses has been successfully confirmed. The observed magnetization precession frequencies reach values up to 15 GHz (30 GHz) at an external field orientation normal to the sample surface (parallel to the layer plane). In the following, the acoustic excitation will be extended to shear strain pulses. Due to the underlying low-symmetry substrate [311]-GaAs both quasi longitudinal and quasi transverse acoustic strain pulses are used to induce magnetization modulation in the Galfenol layer. The qLA and qTA modes injected in the high-index [311]-GaAs substrate propagate at the sound velocities of $\nu_{\text{qLA}} = 5,1$ km/s and $\nu_{\text{qTA}} = 2,9$ km/s with the corresponding propagation times of 20 ns and 35

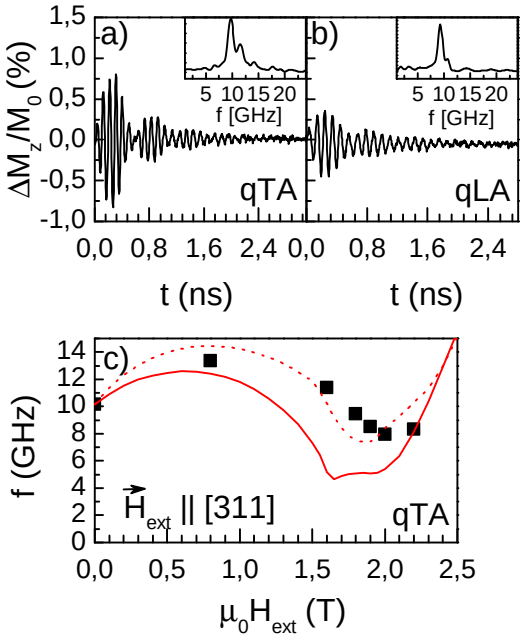

Figure 6.7: (a) and (b): Kerr rotation signals $\Delta M_z(t)/M_0$ measured at different time delays corresponding to acoustic qTA (a) and qLA (b) excitation modes in an external field of $H = 1,8$ T parallel to the $\vec{z}$-direction (Insets show the corresponding frequency spectra). (c): Positions of the fundamental precession frequency line (squares) in dependence of $\mu_0 H_{\text{ext}}$ with field orientation parallel to $\vec{z}$.

ns respectively. The different sound velocities allow the easy distinction of the effects caused by either qLA or qTA modes by adjusting the delay times in the experimental setup. The first magnetization precession signals $\Delta M_z(t)/M_0$ from this structure are measured under the same experimental conditions as in the high-symmetry sample at perpendicular geometry $\vec{H}_{\text{ext}} || \vec{z}$, with $\vec{z}$ being the [311] crystallographic axis of the sample and the pump excitation density of $W = 20$ mJ/cm^2. Figure 6.7 (a) and (b) exhibit typical polarization rotation signals $\Delta M_z/M_0$ measured from excitation with qLA and qTA pulses at an external magnetic field of $\mu_0 H_{\text{ext}} = 1,8$ T. A comparison of the signal amplitudes states the same order of magnitude for both measurements but the signal amplitude measured from the qTA excitation is about twice larger than for qLA. The signal amplitude from the Kerr signal induced by qTA strain pulses reaches $0,7\%$ of the saturation magnetization. The duration of the oscillations lasts for several nanoseconds, similar to the decay times measured from the high symmetry sample. As it has already been shown for the Galfenol film grown on the high symmetry [001]-GaAs substrate beatings in the observed Kerr rotation signals in the low symmetry structure find expression in the formation of high energy spin wave modes.

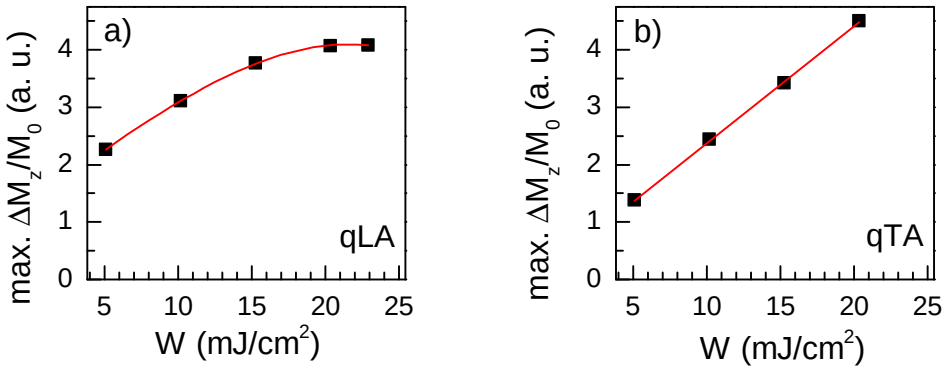

Figure 6.8: Maximum magnetization precession amplitude $\Delta M_{\mathrm{z,max}}/M_0$ for qLA (a) and qTA (b) dependent on the excitation density W of the pump laser light incident on the aluminum transducer.

Several MOKE signals induced by qLA and qTA strain pulses have been recorded for various external fields oriented perpendicular to the sample surface. Figure 6.7 (c) depicts the frequency dependence on $\mu_0 H_{\mathrm{ext}}$ (squares) for the case of the $\Delta M_z(t)/M_0$ signals induced by qTA strain pulses[1]. The relation of the spectral frequency position on $\mu_0 H_{\mathrm{ext}}$ is similar to the frequency dependence observed in the [001]-FeGa sample [figure 6.3 (d)] for the perpendicular field orientation $\vec{H}_{\mathrm{ext}} || \vec{z}$. The following passage is dedicated to the question how the precession amplitude $\Delta M_z/M_0$ is influenced by the excitation density of the pump laser. From chapter 3 it is known that the strain pulse amplitude launched into the GaAs substrate increases proportional to the raised laser power up to a certain regime before anharmonic propagation has to be considered. The precession amplitude of the magnetization signals should depend on the laser power due to the coupling of the strain to the magnetocrystalline anisotropy. The magnetization modulation signal $\Delta M_z/M_0$ for a fixed external magnetic field $\mu H_{\mathrm{ext}} = 1,9$ T has been recorded in dependence of various excitation densities W [mJ/cm^2] depending on the spot size and power of the RegA laser light incident on the aluminum transducer on the backside of the sample. The measurements have been performed for the different time delays corresponding to the propagation times of qLA and qTA strain pulses. The maximum signal amplitude of $\Delta M_z/M_0$ in dependence of the excitation density can be withdrawn from figure 6.8 (a) for qLA and in 6.8 (b) for qTA excitation. W is varied from 5 mJ/cm^2 to maximum values ≤ 24 mJ/cm^2 via a Grey Filter attenuating the pump beam in front of the cryostat.

[1]The frequency dependence on $\mu_0 H_{\mathrm{ext}}$ from the [311]-Galfenol sample has been analyzed for both, the qLA and qTA induced precession signals. As they show the same frequency behaviour the frequency plots presented in this chapter are restricted to qTA measurements for reasons of clarity.

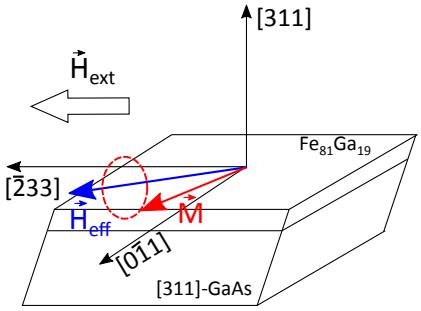

Figure 6.9: Sketch of the [311]-Galfenol sample with in-plane orientation of $\vec{H}_{ext}||[\bar{2}33]$.

For excitation densities up to $W = 15$ mJ/cm^2 the signal amplitude of $\Delta M_z/M_0$ increases almost linearly with increasing W for both acoustic modes. In the case of the qLA strain pulse injected into the Galfenol film, the maximum signal amplitude converges asymptotically until it reaches saturation values at 20 mJ/cm^2 when the laser power is increased further. The relation between the precession amplitude and the injected strain is non-linear. A different behaviour is observed when qTA strain pulses are injected. The magnetization precession signal amplitude increases linearly with increasing W thus indicating an excitation efficiency which remains constant for both low and very high laser excitation densities. The application of higher excitation densities is technically limited by the laser properties and the resistiveness/ durability of the metal transducer. Nevertheless, in the case of magnetization precession induced by qTA strain pulses these technical limitations seem to be the only challenging factors that have to be hurdled in order to reach higher signal amplitudes. In the limits of the given technical setup this pump-power series shown here already indicate that acoustic energy is much more efficiently supplied to the ferromagnetic layer by using qTA phonons.
With increasing laser excitation power anharmonic strain pulse propagation has to be considered as discussed in section 3.3. It has been shown that in the non-linear wave propagation regime the strain pulse displays high amplitudes and a frequency spectrum, also shifted to higher values. In the case of the precession signals induced by qLA strain pulses it is observed that, the spectral density of the strain pulse does no longer cover the characteristic layer magnetization excitation frequency at high laser powers. Therefore, exceeding the limit of $W \approx 20$ mJ/cm^2 the signal amplitude is not increased any further. This limiting effect of the solitonic wave propagation is not observed for qTA induced precession signals. Nevertheless, these assumptions have to be manifested in more elaborated studies in this direction and nuanced analysis of the different soliton formation for qLA and qTA strain pulses is required.
The last part of this section is devoted to the magnetization modulation of the [311]-FeGa sample in the in-plane geometry. To provide an easy access to the geometrical conditions, analogous to the in-plane measurements from the [001]-FeGa sample, the

magnetization modulation concept for $\vec{H}_{\text{ext}} \perp \vec{z}$ is sketched in figure 6.9. The orientation of the external field vector is parallel to the [$\bar{2}33$] crystallographic direction. The subsequent precession of magnetization is exemplarily shown in figure 6.10 for

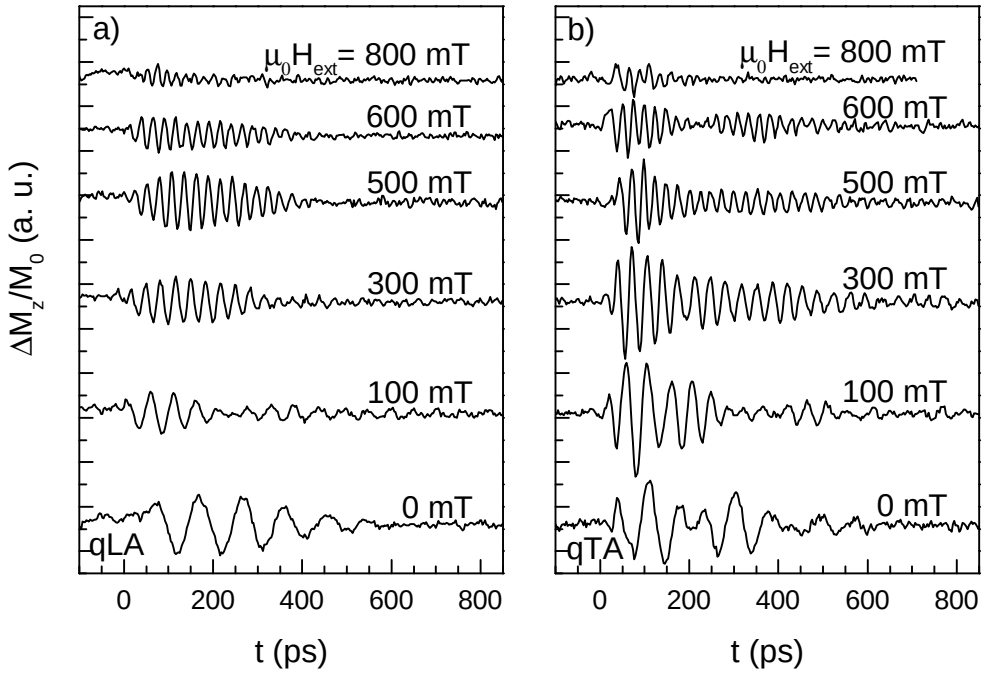

Figure 6.10: Magnetization modulation signals $\Delta M_z/M_0$ as a function of the time delay measured for various external magnetic fields. (a): Signals induced by qLA strain pulses, (b): Signals induced by qTA strain pulses.

excitation with qLA [plot (a)] and qTA [plot (b)] strain pulses for various $\mu_0 H_{\text{ext}}$ ranging from 0 to 800 mT. It is the slot of external fields where the measured signals reach maximum oscillation amplitudes at largest decay times. Analogous to the previous measurements in $\vec{H}_{\text{ext}} || \vec{z}$ geometry the oscillatory motion shows beatings of different frequencies in the time domain and split spectral lines in the corresponding FFT spectra resulting from spin wave excitations. The larger the external field, the faster the oscillatory motion damps out. The largest decay time of approx. 700 ps is observed at external fields around $\mu_0 H_{\text{ext}} = 300$ mT. The Gilbert damping term in the *Landau-Lifshitz-Gilbert* equation (4.1) reflects the intrinsic damping of the magnetization motion and can be estimated to $G \approx 3 \times 10^9\ s^{-1}$. Similar results have been reported in FMR studies in ultra thin films of iron [26]. The precession frequency dependence on $\mu_0 H_{\text{ext}}$ from magnetization signals induced by qTA pulses is shown in figure 6.11 as squared data points. As observed in the high symmetry [001]-FeGa sample and $\vec{H}_{\text{ext}} \perp \vec{z}$ geometry, the frequency dependence from the modulation of the

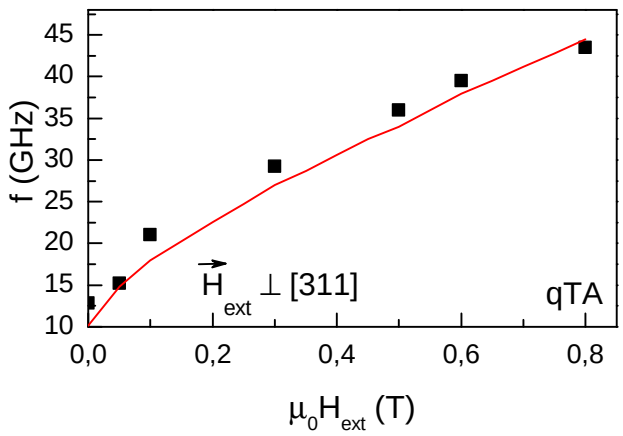

Figure 6.11: Precession frequency dependence on the external magnetic field oriented parallel to the layer plane ($\vec{H}_{\text{ext}} \perp \vec{z}$) for qTA induced magnetization modulation in the [311]-FeGa sample (squares).

high-index structure yields a similar pattern. The precession frequency seems to increase almost linearly with increasing magnetic field. The maximum value reaches 45 GHz at $\mu_0 H_{\text{ext}} \approx 800$ mT and is the largest precession frequency value observed in the magnetization modulation experiments reported here. Compared to the maximum frequencies gained from the magnetization modulation in $\vec{H}_{\text{ext}} || \vec{z}$ geometry, the precession frequency is three times larger. A detailed discussion with theoretical analysis of the frequency dependence for both sample structures and different geometries will be presented in the next section.

6.4 Theoretical discussion

This section is devoted to the more elaborated analysis of the magnetization precession frequencies provided in the picosecond magneto-acoustic measurements from both, the [001]- and the [311]-Galfenol layers. An overview of the theoretical analysis of strain induced magnetization precession presented in [29] shall underline experimental findings.
The fundamental precession frequency dependence on the external magnetic field observed from experimental data has already been discussed for both samples and different geometries in the previous sections. To provide a better overview, the different measurement plots are rearranged together in figure 6.12. Measurement points are illustrated as black symbols. Plot (a) provides the spectral peak positions at the field orientation $\vec{H}_{\text{ext}} || \vec{z}$ i.e. parallel to the [001] axis measured from the [001]-Galfenol sample. The same field orientation applied to the [311]-Galfenol layer ($\vec{H}_{\text{ext}}$||[311] axis) refers to the data set shown in (b). The plots (c) and (d) present the frequency maxima achieved from the [001]- and [311]-structures at in-plane external field orientation. Comparing the results of both different samples reveal similar trends in the

field dependence. The $\vec{H}_{\text{ext}}||\vec{z}$ field orientation provides a rather complicated relation of the frequency on H_{ext} with maximum frequencies up to 14 GHz. In contrast, for the in-plane geometry, the frequencies seem to increase linearly with increasing magnetic field, leading to maximum frequencies of 40 to 45 GHz.

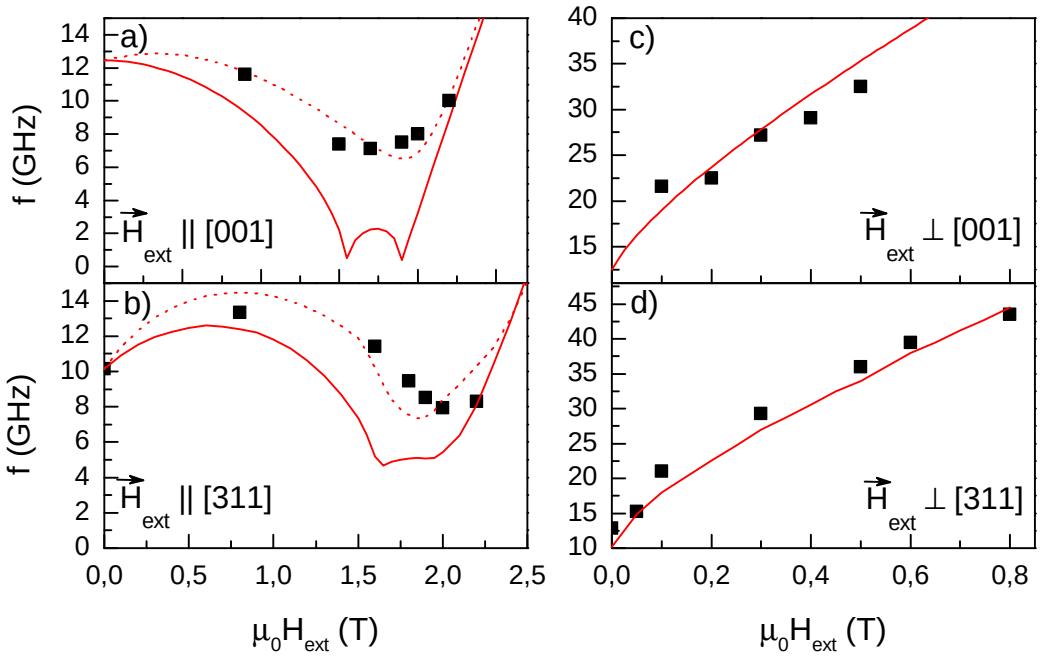

Figure 6.12: Fundamental precession frequency plotted as a function of the applied external magnetic field (squares) for both sample structures. (a) and (b): perpendicular geometry $\vec{H}_{\text{ext}}||[001]$ [[001]-Galfenol (a)] and $\vec{H}_{\text{ext}}||[311]$ [[311]-Galfenol (b)]. (c) and (d): In-plane geometry $\vec{H}_{\text{ext}}\perp\vec{z}$ for the [001]- (c) and [311]-Galfenol structure (d). Solid lines show the dependence of the frequencies on $\mu_0 H_{\text{ext}}$ ($\vec{H}_{\text{ext}}$ exactly parallel to $\vec{z}$) calculated from a theoretical approach derived in [29]. Dotted lines display the frequency dependence for $\vec{H}_{\text{ext}}$ forming an angle of $1,8°$ with the $\vec{z}$ axis.

The theory of strain induced magnetization precession discussed here, has been initially developed for a [001]-GaMnAs structure in Ref. [29] but may be analogously transferred to [311] ferromagnetic thin films as Galfenol. The free energy density of a ferromagnetic thin layer grown on a [311] semiconducting substrate introduced in

(2.1) may be rewritten as [23], [29]

$$F = F_m(m_i, \eta_{ij}) + \frac{1}{2}\mu_0 M_0 m_z^2 - (\vec{m} \cdot \mu_0 \vec{H}_{ext}) \tag{6.1}$$

with the shape anisotropy or demagnetization (2nd term), the Zeeman energy (3rd term) and the magneto-crystalline anisotropy terms

$$F_m(m_i, \eta_{ij}) = K_c[m_x^4 + m_y^4 + m_z^4] + A_{2\eta}[\eta_{xx} m_x^2 + \eta_{yy} m_y^2 + \eta_{zz} m_z^2] \tag{6.2}$$

$$+ A_{2xy}[\eta_{xy} m_x m_y + \eta_{xz} m_x m_z + \eta_{yz} m_y m_z] + A_{4\perp} \eta_{zz} m_x m_y. \tag{6.3}$$

The coefficient K_c denotes the cubic anisotropy field while $A_{2\eta}$ and A_{2xy} provide the magneto-elastic coefficients. An additional coefficient $A_{4\perp}\eta_{zz} m_x m_y$ describes the strength of a lower-order in-plane magneto-elastic coupling in Galfenol. The equilibrium orientation of the magnetization $\vec{M}$ is determined by the minimum of F, depending on the balance between all terms contributing to the free energy density. In order to determine the magnetization direction it is convenient to change to the spherical coordinate system. As $\vec{M}$ may be regarded as uniform wherein all magnetic moments are aligned parallel with an average magnetization per unit volume, a single-domain model of $\vec{M}$ is considered. The time dependent modulation of $\vec{M}$ given by the *Landau-Lifshitz-Gilbert* equation (4.1) in the spherical coordinates θ and ϕ states [88]

$$\frac{\partial \theta}{\partial t} = -\frac{\gamma}{\sin\theta} \frac{\partial F}{\partial \phi}, \tag{6.4}$$

$$\frac{\partial \phi}{\partial t} = \frac{\gamma}{\sin\theta} \frac{\partial F}{\partial \theta}. \tag{6.5}$$

Acoustic strain pulses change θ and ϕ by small deviations $\Delta\theta$ and $\Delta\phi$. These small effects on the angles may be expressed throughout the linear approximation of the time dependent angular changes[1]

$$\frac{\partial \Delta\phi}{\partial t} = \frac{\gamma}{\sin\theta_0}[F_{\theta\theta}\Delta\theta + F_{\theta\phi}\Delta\phi + F_{\theta\eta_{zz}}\eta_{zz}(z,t)], \tag{6.6}$$

$$\frac{\partial \Delta\theta}{\partial t} = -\frac{\gamma}{\sin\theta_0}[F_{\phi\phi}\Delta\phi + F_{\phi\theta}\Delta\theta + F_{\phi\eta_{zz}}\eta_{zz}(z,t)] \tag{6.7}$$

where $F_{ij} = \frac{\partial^2 F_m}{\partial_i \partial_j}$ $(i, j = \theta, \phi, \eta_{zz}(z,t))$ calculated at the equilibrium conditions θ_0, ϕ_0 corresponding to the static orientation of $\vec{M}$ at given $\vec{H}_{\text{ext}}$. From this equation,

[1] Both expressions are derived for high symmetry conditions with longitudinal strain η_{zz} but may be extended to low symmetry conditions. The results and discussion are analogous in both cases.

effective rates of the modulation induced by strain may be defined as

$$f_\phi = \frac{\gamma}{\sin\theta_0} F_{\theta\eta_{zz}} \propto -A \cdot \gamma \cos\theta_0 \tag{6.8}$$

$$f_\theta = -\frac{\gamma}{\sin\theta_0} F_{\phi\eta_{zz}} \propto -B \cdot \gamma \sin^3\theta_0 \sin 4\phi_0 \tag{6.9}$$

with A and B dependent on the magneto-elastic coefficients. f_ϕ and f_θ govern the amplitude and direction and thereby the efficiency of the tilt of $\vec{H}_{\text{eff}}$ induced by $\eta_{zz}(z,t)$ for a given static orientation of $\vec{M}$ [29]. This means that the rates represent a torque acting on the magnetization. Moreover, equations (6.8) and (6.9) state that a change of $\vec{H}_{\text{eff}}$ in θ results in a torque acting on $\vec{M}$ only in ϕ, whereas the tilt of $\vec{H}_{\text{eff}}$ in ϕ results in a torque on $\vec{M}$ in θ. The geometrical relation of the tilted $\vec{H}_{\text{eff}}$ and the effective precession rates f_θ and f_ϕ is sketched in figure 6.13. Vanishing values for the

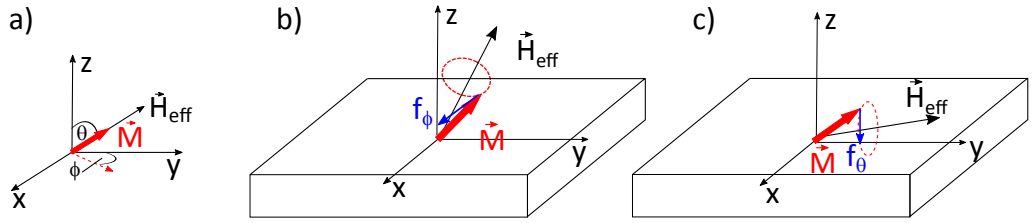

Figure 6.13: Illustration of the tilting rates f_θ and f_ϕ. (a): The equilibrium orientation of $\vec{M}$. (b) and (c): Tilt of $\vec{H}_{\text{eff}}$ in θ out of the layer plane (b) [or in ϕ (c)] and the torque f_ϕ [f_θ] acting on $\vec{M}$.

effective rates indicate that $\vec{H}_{\text{eff}}$ is not tilted by any strain pulse so no magnetization dynamics is observed. The magnetization precession frequency ω_0 depending on the static orientation of $\vec{M}$ can be calculated as

$$\omega_0 = \frac{\gamma}{\sin\theta_0} \sqrt{F_{\theta\theta} F_{\phi\phi} - F_{\theta\phi}^2} \tag{6.10}$$

analogous to the ferromagnetic resonant frequency obtained in (4.2). The precession rates f_ϕ, f_θ, modulation frequency ω_0 and the maximum magnetization amplitudes $\Delta M_{\text{z,max}}$ can be examined by numerical calculations[1] for (i) a perpendicular external magnetic field $\vec{H}_{\text{ext}} || \vec{z}$ and (ii) an in-plane orientation of external magnetic field $\vec{H}_{\text{ext}} \perp \vec{z}$ [29]. A short overview of the results with respect to the main correlations shall sustain the analysis of experimental measured data.
(i) Because $f_\theta = 0$ when $\phi = 0$, the tilting of $\vec{H}_{\text{eff}}$ is determined by f_ϕ. The stronger

[1] The theoretical background shortly traced here is extracted from a more detailed discussion which is found in Ref. [29]

the magnetization is turned away from the in-plane easy axis by $\vec{H}_{\mathrm{ext}}$, the response of $\vec{H}_{\mathrm{eff}}$ on the induced strain pulse increases. $|f_\phi|$ increases almost linearly until the magnetization rapidly turns towards the direction of $\vec{H}_{\mathrm{ext}}$ in the case when the orientation of $\vec{H}_{\mathrm{eff}}$ is almost parallel to $\vec{H}_{\mathrm{ext}}$. Contrary, the precession frequency value ω_0 decreases with increasing H_{ext}. Thus, the averaged precession amplitude $\Delta M_{\mathrm{z,max}}$ is governed by the balancing of both competing evolutions of ω_0 and f_ϕ. Therefore, the maximum amplitude of $\Delta M_{\mathrm{z,max}}$ is found at an intermediate field of H_{ext}. This has been experimentally confirmed and shown for the maximum $\Delta M_z(t)/M_0$ signal dependence on H_{ext} in the [001]-FeGa film (see figure 6.3 (c)).
(ii) At in-plane geometry the tilt of $\vec{H}_{\mathrm{eff}}$ is determined only by f_θ because f_ϕ vanishes for $\theta = 0$ [compare eqs. (6.8) and (6.9)]. The strain pulse tilts $\vec{H}_{\mathrm{eff}}$ only in the layer plane. The tilt efficiency $|f_\theta|$ decreases with increasing field H_{ext} because $\vec{M}$ is tilted towards the hard axis of the layer. In contrast to a perpendicular H_{ext} ω_0 continuously increases with the external field to higher values than calculated for (i) because the value of H_{eff} is larger for in-plane geometry. The behaviour of the maximum amplitude of the precession dynamics $\Delta M_{\mathrm{z,max}}$ is comparable to the result for the perpendicular geometry discussed in (i). As before, the dependence is governed by the tilting sensitivity of H_{eff} and the precession frequency. $\Delta M_{\mathrm{z,max}}$ reaches maximum values at low external fields and decreases continuously when H_{ext} is increased which can be observed experimentally from the magnetization dynamics shown in figure 6.10. The field dependence of $\Delta M_{\mathrm{z,max}}$ decreases asymptotically because no instant flipping to a hard axis occurs. Ref. [29] may be considered for more details.
The solid red curves in each plot of figure 6.12 display the magnetic field dependence of the frequency calculated according to the theoretical approach above concerning the different geometries. Therein, the expression for the free energy density (6.3) is used to calculate the precession frequency (6.10) at different external magnetic fields. The parameters enter the calculation as the saturation magnetization $\mu_0 M_0 = 1,8$ T, perpendicular uniaxial anisotropy field $H_{2\perp} = 100$ T, cubic anisotropy field $K_c = -25$ mT, in-plane uniaxial anisotropy field $H_{2||} = -20$ mT, the magneto-elastic coefficients $A_{2\eta} = -9$ T and $A_{2xy} = 5$ T and the lower-order in-plane magneto elastic coefficient $A_{4\perp} = 1$ T [32].
For the $\vec{H}_{\mathrm{ext}}||\vec{z}$ geometry the calculation assumes the alignment of H_{ext} being strictly parallel to the $\vec{z}$ axis for both structural symmetries. As presumed from figure 6.12 (a) and (b) the theoretically gained frequency dependences differ remarkably from the experimental data. An additional dotted curve is calculated from the same theoretical approach but for a slight angle deviation of the $\vec{H}_{\mathrm{ext}}$ orientation from the $\vec{z}$ axis about $1,8°$. In this case the theoretically modeled frequency dependence on magnetic field fits the experimental data very well indicating a slight misalignment in the direction of the external magnetic field in the experimental setup. The existence of two local minima resolvable especially in the theoretical calculation is attributed to the strong saturation magnetization $\mu_0 M_0$ and in-plane uniaxial anisotropy pa-

rameter $H_{2||}$ of Galfenol. Usually, ferromagnetic materials like pure iron or GaMnAs display a single minimum of the frequency dependent on H_{ext} as it has been explained in (i). Only the polar angle θ is modified by the external field, resulting in one single minimum of the frequency. In Galfenol, ϕ is not zero but very small. Thus, both the polar θ and azimuthal angle ϕ are modified by $\vec{H}_{\text{ext}}$ emerging in two local minima seen in the dependence of the fundamental frequency [see figure 6.12 (a) and (b)]. The magnetic field dependence observed from the Kerr rotation measurements in the in-plane $H_{ext}\perp z$ (figure 6.12 (c) and (d)) geometry has been also calculated theoretically from the same values for the free energy parameters as in the case $H_{ext}||z$. The red solid theory curve is in good agreement with the experimental data.

In conclusion, three main factors are assumed to govern the amplitude of the strain induced magnetization precession [29, 23]. First, the general frequency matching condition plays an important role. In order to excite magnetization modulation at frequencies characteristic for the Galfenol layer the spectral density of the strain pulse has to cover the frequencies of magnetic excitations. The broad spectra for the LA, qLA and qTA pulses are centered in the GHz range thus matching typical ferromagnetic resonance frequencies found in Galfenol thin layers. Second, the precession signal amplitude is determined by the competition of the tilt sensitivity of the effective magnetic field $\vec{H}_{\text{eff}}$ given by the precession rates f_θ and f_ϕ and the dependence of the precession frequency on H_{ext}. Experimentally, the maximum precession frequencies are reached for an in-plane orientation of $\vec{H}_{\text{ext}}$ [figure 6.12 (c) and (d)] where the frequency converges asymptotically to $30-35$ GHz ($40-45$ GHz). Theoretical considerations above state that while ω_0 is increasing with H_{ext}, the tilt efficiency of H_{eff} and therefore the torque acting on $\vec{M}$ decreases to zero. Therefore, maximum precession amplitudes are observed at intermediate external fields. The third factor is the synchronization condition which is fulfilled when the time interval the strain pulse needs to propagate through the magnetic layer forward and backward matches the period of the magnetic spin precession [23, 29].All three factors govern the complicated precession trajectory of $\vec{M}$.

6.5 Room-temperature measurements

After the magnetization modulation induced by ultrafast acoustic strain pulses in thin Galfenol layers has been discussed in detail, this section aims at utilizing a very important feature of the Galfenol structure: The ability to perform experiments at ambient temperatures. All experiments have been carried out at cryogenic temperatures of 4 to 10K to avoid the attenuation of the high frequency components of the strain pulse. Thereby, magnetization modulation amplitudes of $\Delta M_z/M_0 = 0,7$ % are reached. At higher temperatures, the dominant attenuation mechanism for an acoustic strain pulse through a GaAs substrate is the anharmonic interaction

with the bath of thermal phonons [89]. Although the physical concept of strain induced magnetization modulation has been successfully realized in Galfenol, heading towards realistic applications in technology requires structures performing at room-temperatures. As the Curie temperature of Galfenol exceeds 600 °C it serves as an ideal candidate for investigations at room temperature. As before, the experiments are carried out in a cryostat in order to be able to utilize the superconducting magnetic split coils of the system. The sample is first heated up from the cryogenic to near room temperatures and then the temperature is controlled to a constant value automatically. The dependence of the intensity $I(t)$ of the reflected probe beam on

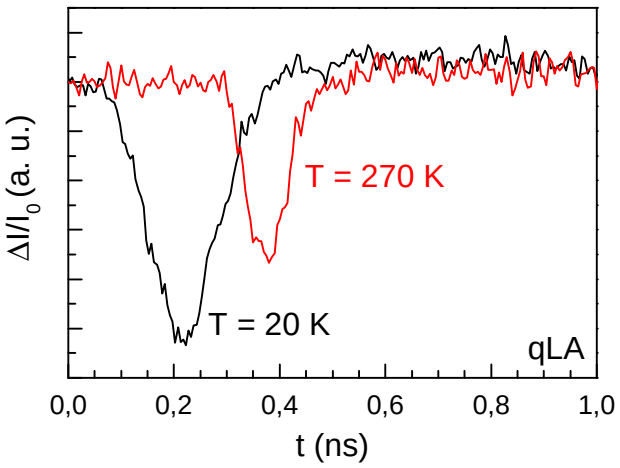

Figure 6.14: Time-dependence of the intensity $I(t)$ of the reflected probe beam measured at low temperatures (20 K, black curve) and near room temperature (270 K, red curve) from the [311] sample.

the time delay for the [311]-FeGa sample measured near room temperature (270 K) is shown in figure 6.14. The plot also contains the corresponding signal measured at cryogenic temperature. From the comparison of both signals one can observe a shift of the whole signal at 270 K in time. The strain pulse needs a longer time to propagate through the GaAs substrate because of the thermal expansion of the layer and due to the lower strain pulse velocity at higher temperatures. Possible propagation distances are also lowered at ambient conditions due to strong attenuation mechanisms related to the strain pulse interaction with thermal phonons [90]. The temporal evolution of the z-component of the magnetization measured through the polar magneto-optical Kerr effect for both [001] and [311] samples and in different experimental geometries near room temperature are depicted in figure 6.15. The left panel exhibits Kerr signals induced by LA, qLA and qTA strain pulses in $\vec{H}_{\mathrm{ext}} || \vec{z}$ geometry at $2,2$ T and $1,9$ T where maximum decay times were observed at cryogenic temperatures. As a first impression the signals are comparable to those measured

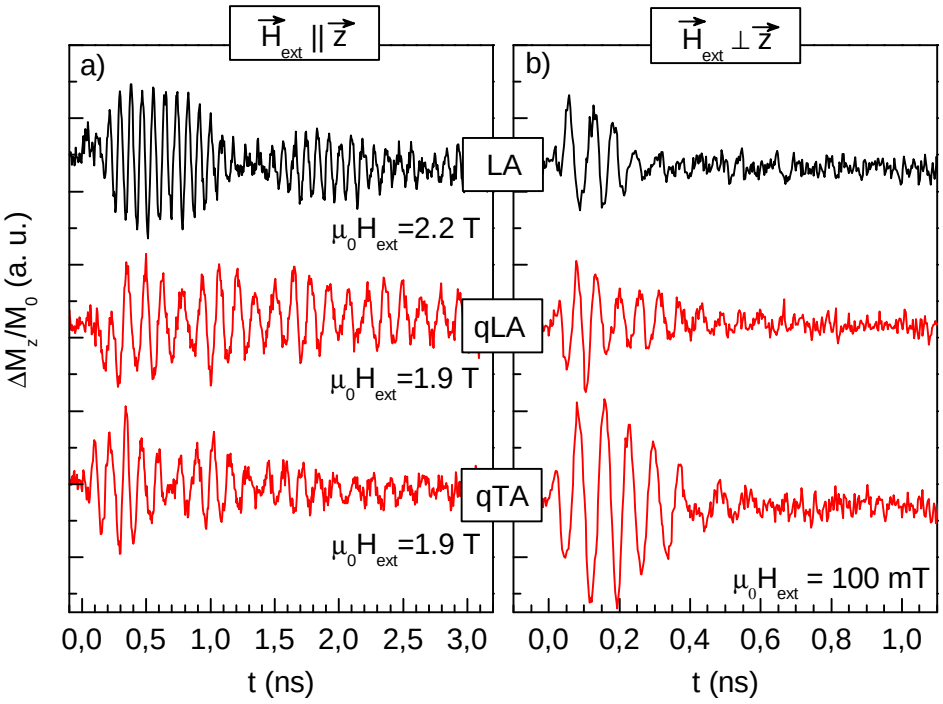

Figure 6.15: Magnetization precession signals $\Delta M_z/M_0$ in dependence of the time delay measured for Galfenol films grown on [001] and [311]-GaAs substrates at 270K: (a) Orientation of the external magnetic field $\vec{H}_{\text{ext}}$ normal to the sample surface ($\vec{H}_{\text{ext}}||\vec{z}$). (b) In-plane orientation of $\vec{H}_{\text{ext}}$. Both panels display excitation of magnetization modulation by LA ([001]FeGa sample), qLA and qTA ([311]-FeGa sample).

at low temperatures. Although, the signals at 270 K appear to be noisier (most likely due to Helium circulation) the duration of the oscillations is almost as long as obtained at lower temperatures. The signal amplitude is a bit lower reachingh about $0,3\%$ of the saturation magnetization. The fundamental precession frequency of 10 GHz (not displayed) is comparable to the frequencies measured before. Additionally, the Kerr rotation signals display beatings of the oscillatory motion indicating the excitation of several spin wave modes contributing to the frequency spectrum. The right panel of figure 6.15 displays the time evolution of $\Delta M_z(t)/M_0$ in $\vec{H}_{\text{ext}}\perp\vec{z}$ geometry with different time delay settings corresonding to LA, qLA and qTA modes. The plot depicts measurements at $\mu_0 H_{\text{ext}} = 100$ mT. The highest precession frequency measured in the in-plane geometry is nearly 30 GHz which is also comparable to the results at cryogenic temperatures.
In conclusion, the investigations presented in this section are one of the most important results of the experiment reported in this thesis. Acoustic strain pulse induced

high-frequency magnetization modulation of a thin ferromagnetic layer has been realized at ambient temperatures. So far, magnetization modulation induced by ultrafast acoustics has been reported in several structures only at cryogenic temperatures [22, 23] or close to room temperatures but with rather low precession frequencies [24]. The possibility to modulate the magnetization by strain pulses in Galfenol at sub-THz frequencies and ambient temperatures establishes the material as a promising candidate for future applications in information and communication technology actually approaching the enhancement of data storage and operating speeds.

6.6 Conclusion

In this chapter, it has successfully been shown that the conversion of acoustic energy into magnetic excitation leads to high frequency magnetization precession in nanometer layers of ferromagnetic Galfenol. The first observation of pure LA strain induced magnetization modulation in Galfenol films grown on high symmetry [001]-GaAs substrates reveal precessional motion at decay times up to 3 ns and precession frequencies in the GHz range comparable to typical FMR measurements from these structures [45]. The corresponding spectral density displays several frequency lines due to the excitation of higher spin wave modes.
In a low symmetry sample with an underlying [311]-GaAs substrate qLA and qTA strain pulses are launched and the magnetization modulation in the Galfenol layer has been measured at different time delays corresponding to each acoustic mode. The maximum precession amplitude that has been measured in these experiments relates to the magnetization excitation by qTA phonons. By means of the magneto-optical Kerr effect the z component of $\vec{M}$ perpendicular to the sample surface is monitored. Maximum amplitude values reach $\Delta M_{\mathrm{z,max}} = 0,7$ % of the saturation magnetization. Due to the shape anisotropy, the in-plane component ΔM_y is expected to reveal higher amplitudes up to 2 % of M_0 at in-plane orientation of $\vec{H}_{\mathrm{ext}}$ and 100 mT. The corresponding absolute amplitude of $\mu_0 \Delta M_y = 40$ mT is higher than tilting amplitudes yielded in similar experiments so far [23, 24]. Pump power series have shown that in principle higher precession amplitudes induced by qTA strain may be accessible in the studied Galfenol film. A linearly enhanced maximum signal amplitude $\Delta M_{\mathrm{z,max}}$ with increased pump excitation density assumes that the signal amplitude is primarily limited by technical parameters such as laser power and damage factors of the aluminum transducer. The largest precession frequencies up to 45 GHz are reached at in-plane geometry. The results are in good accordance with typical frequencies measured in FMR experiments in Galfenol.
Since Galfenol with it's giant magnetostrictive properties is supposed to be an auspicious material for future magnetization control in many technical applications, magnetization modulation experiments at ambient temperatures is highly appreciated to open the way for application-oriented science. Therefore, both Galfenol structures

[001]-FeGa and [311]-FeGa have been investigated at 270 K. Beside smaller attenuation effects the results gained at cryogenic temperatures have been reproduced. Precession frequencies up to 30 GHz have been observed in in-plane geometrical orientation as well as long signal lifetimes up to 3 ns in $\vec{H}_{\mathrm{ext}} || \vec{z}$ geometry are comparable to $\Delta M_z(t)/M_0$ signals at low temperatures.

7 Resonant driving of magnetization precession by localized phonons in an acoustic cavity

This chapter presents the resonant modulation of the strain-induced magnetization dynamics in Galfenol by localized phonon modes in an underlying phonon cavity. Expanding the concept of magnetization precession in ferromagnetic materials on picosecond time scales leads to the novel exploration of magnetic resonance phenomena on similar time and spatial scales. Although, the resonant driving and monitoring of magnetization is widely exploited nowadays and has become, for example, an established branch of clinical technology and science [91] and a hot topic in the research field of Nuclear Magnetic Resonance (NMR) quantum computing [92]. Common techniques operating at magnetic resonance frequencies in the GHz and THz regime are usually scanned by microwave techniques [93, 94]. Nevertheless, high speed operation times down to picosecond time scales remain challenging so far. Via application of picosecond strain pulses to a high magnetostrictive ferromagnetic layer magnetization dynamics on picosecond timescales at precession frequencies up to 45 GHz have been successfully demonstrated in chapter 6. In the following, it will be shown how this precession dynamics may be significantly enhanced by the interaction of the magnetic resonance with localized phonon modes in an acoustic cavity.
In this chapter, first, the sample structure composed of the previously characterized Galfenol film embedded in a phononic Fabry-Perot cavity will be introduced, followed by an overview of the experimental conditions of the measurement setup. Afterwards the experimental findings and the discussion of results will be presented.

7.1 Sample characterization

A Galfenol layer with chemical composition of $Fe_{81}Ga_{19}$ and 59 nm thickness covered with a 5 nm thick GaAs cap is deposited on a system of two Superlattices (SLs) forming acoustic Bragg mirrors. The SLs are grown on a semi-insulating [001]-GaAs substrate of 100 μm thickness via molecular beam epitaxy. A sketch of the studied sample structure is given in figure 7.1 (a). Each superlattice consists of two different

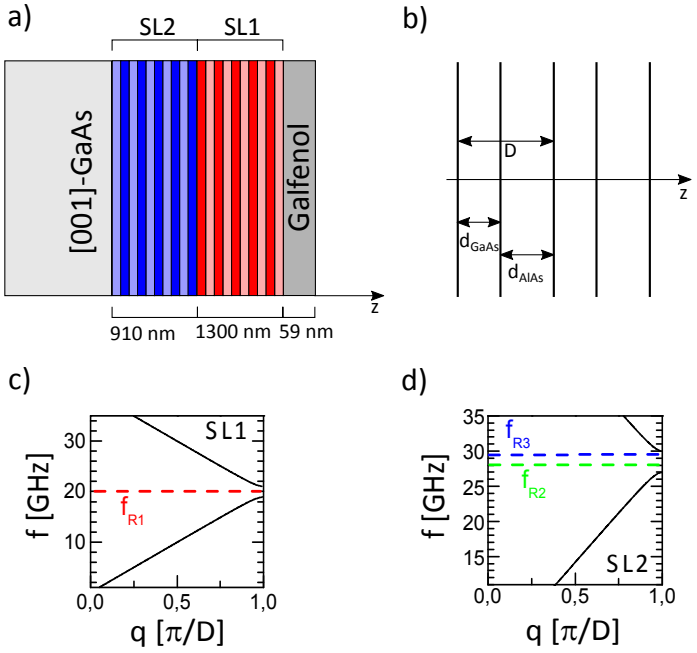

Figure 7.1: (a): Sample structure containing two superlattice structures SL1 and SL2 of 10 GaAs/AlAs bi-layers epitaxially grown on a [001]-GaAs substrate and a $Fe_{81}Ga_{19}$ film on top. (b) Zoomed sketch of the SL system. Phonon dispersion relation curves associated with the two different superlattices SL1 (c) and SL2 (d). f_{R1}, f_{R2} and f_{R3} indicate the frequency of the phonon cavity resonances.

semiconductor materials GaAs and AlAs deposited alternately on each other forming a periodic bi-layer of 10 periods in the growth direction. The layer interfaces are plane perpendicular to the z axis. The thickness of the GaAs/AlAs period is 59/71 nm for the SL1 and 42/49 nm for the SL2 structure. Beside intensive research of electronic quantum states and optical transport properties in SL structures acoustic characteristics have been investigated. These multilayer structures serve as so-called nanophononic *Bragg* mirrors: Because of the different acoustical impedances of the two semiconducting materials a propagating longitudinal acoustic phonon wave with wavelength λ_{LA} undergoes Bragg reflections in case the Bragg condition $m\lambda_{LA} = 2D\cos\theta'$ is fulfilled [95, 96]. Here, D is the SL period $D = d_{GaAs} + d_{AlAs}$, m the reflection order and θ' denotes the angle between the phonon wave vector and the z axis normal to the sample surface. In case of the experimental geometry $\theta = 0°$ and the Bragg condition reduces to $m\lambda_{LA} = 2D$ for zero incidence. As the phonon wave vector is given by $q = 2\pi/\lambda_{LA}$, phonons with $q = m\pi/D$ are reflected and do not propagate through the SL. The phonon dispersion is folded into the first Brillouin zone defined by $-\pi/D \leq q \leq \pi/D$. The selective reflection of phonon modes yield frequency gaps (i.e. phononic stop bands) in the reduced phonon dispersion relation.

A calculation model to derive the dispersion relation is shown in [97]. Therein, the center of the mth-frequency gap is calculated after

$$f = \frac{m}{2} \frac{1}{(d_{\mathrm{GaAs}}/s_{\mathrm{GaAs}} + d_{\mathrm{AlAs}}/s_{\mathrm{AlAs}})}, \tag{7.1}$$

with $s_{\mathrm{GaAs}}, s_{\mathrm{AlAs}}$ as the sound velocities of the LA phonon wave in each layer[1]. The propagation of phonon modes is impossible in these frequency intervals. Phonons with frequencies different from these gaps are transmitted through the SL whereas phonons with frequencies matching the gap frequencies are reflected. The phonon spectrum and stop bands are experimentally investigated by Raman-scattering and in phonon transmission spectroscopy studies [98, 96]. Because of this frequency selective property superlattice structures find application as phonon filters [99]. The transmission rate of the propagating phonons through a SL may be determined from the transfer-matrix formalism generally used for the calculation of the propagation of electromagnetic or acoustic waves through a periodically stacked medium [100, 101, 97]. In this approach, the acoustic properties of each semiconductor layer are expressed in terms of a characteristic matrix. The whole stack of individual layers can be represented as an equivalent layer matrix that is the product of the single characteristic matrices of the single layers. From this representation, the transmission and reflection coefficients are derived. The frequency dependence on the transmission rate yield pronounced dips centered around frequencies that satisfy the Bragg condition thus, leading to zero transmission corresponding to the stop bands. The phonon dispersion relations are shown in figure 7.1 (c) and (d) as black curves for both superlattices SL1 and SL2. Because of the chosen nm thickness of the SL periods, the phononic stop bands are localized in the GHz range at 20 GHz (SL1) and around 28 GHz (SL2).
The studied Galfenol layer is sandwiched between two phononic mirrors: The top mirror is the open surface and the other one, the SL1 or SL2 superlattice below. These components together form an acoustic planar Fabry-Perot resonator which confines sound in the sub-THz regime. The Galfenol film serves as the resonator cavity. Note that, as the SL2 mirror is grown below the SL1 mirror, SL1 is counted as a part of the cavity as well from the viewpoint of the SL2 mirror. This acoustic nanocavity is equivalent to optical Fabry-Perot resonators constituted of semiconductor microcavities between distributed Bragg reflectors for photon confinement used in experiments enhancing photonic lifetimes [102, 103]. The acoustic cavity under study possesses a discrete spectrum of frequency resonances f_{Ri}, depending on the cavity size and the acoustic wavelength. The calculation of the phonon resonances can be found in [101]. For the given structure the resonance frequencies $f_{\mathrm{R1}} = 20,0$ GHz, $f_{\mathrm{R2}} = 28,0$ GHz and $f_{\mathrm{R3}} = 29,5$ GHz are indicated as horizontal lines in

[1]Note that, because of the high symmetry structure of the sample, transverse acoustic strain pulses are not generated.

the SL dispersion relations in figure 7.1 (c) and (d). All cavity frequencies fall into the frequency gaps corresponding to SL1 (f_{R1}) and SL2 (f_{R2} and f_{R3}) respectively. Therefore, a cavity mode with a frequency in the SL stop band may be confined in the acoustic resonator.

7.2 Experimental conditions

The experimental realization of the resonant driving of magnetization dynamics by injecting acoustic strain pulses is based on the same time-resolved pump-probe technique as it has been used in the previous experiments reported in this work. But, in contrast to the previous experiments, the strain pulse excitation and the probing is realized from the same side, on the Galfenol layer surface wherein the Galfenol material itself serves as the opto-elasitcal transducer. The experimental settings are schematically shown in figure 7.2. Besides, all other technical settings and equipment

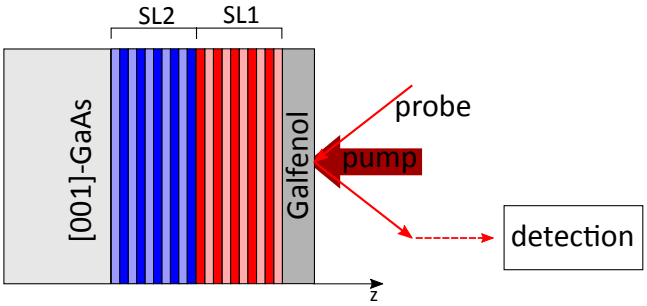

Figure 7.2: Experimental scheme of the magnetization excitation and probing of the MOKE from the Galfenol layer deposited on a GaAs/AlAs-SL system.

remain the same and can be looked up in chapter 4.2. The Galfenol layer is excited by optical pump pulses with an excitation density of $W \approx 10$ mJ/cm^2. Analogous to the previous measurements the changes in the magnetization component ΔM_z of $\vec{M}$ are monitored throughout the polar magneto-optical Kerr effect. Therefore, a probe pulse of $W \approx 20$ μJ/cm^2 energy is applied at the sample surface overlapping the pump laser spot. The reflected probe beam is directed to the balanced detection scheme. The sample is mounted in the bath cryostat where measurements at various temperatures up to ambient conditions and at different external magnetic fields are facilitated. All results shown in the next section are measured at 170 K and $\vec{H}_{ext}$ applied parallel to the [100] crystallographic axis in the layer plane, close to the easy magnetization axis [47, 45]. Acoustic strain pulses induced by femtosecond laser pulses change the magnetic anisotropy parameters of the Galfenol layer, leading to magnetization precession as shown in the previous chapter. The frequency of the

following magnetization precession can be driven by $\vec{H}_{\text{ext}}$ into the regime of the stop band frequencies of the SLs. The monitored signals and physical concept will be discussed in the next section.

7.3 Results and discussion

As the aim of this study is to investigate the interaction of resonant cavity phonons with magnetic excitation in the Galfenol layer it is worthwhile to start with measurements of the magnetization precession $\Delta M_z(t)/M_0$ at frequencies f_{M} which are expected to match the resonator modes f_{Ri}. Therefore, three magnetization precession signals from the Galfenol layer, measured by means of the polar MOKE, are compared in figure 7.3. The black magnetization curves are measured for 100 and

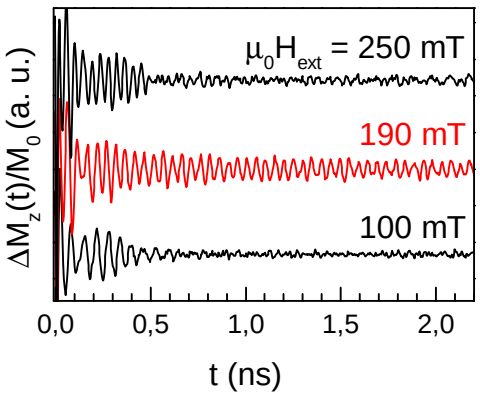

Figure 7.3: Time evolution of the $\Delta M_z(t)/M_0$ dynamics in the 59 nm Galfenol film deposited on a SL system, measured at different external magnetic fields $\mu_0 H_{\text{ext}}$.

250 mT showing decay times of the oscillatory motion around 500 ps. The signal characteristics are in full coincidence with the results obtained from the pure Galfenol samples at in-plane geometry (see chapter 6 and [45]). Instead, the signal measured at 190 T (red curve) displays a long-living oscillatory tail with an increased lifetime to more than 2 ns. The decay time is four times larger than the precession lifetime in the previous experiment. Additionally, several $\Delta M_z(t)/M_0$ data plots have been recorded for external field strengths between 100 mT to 300 mT with a step of 10 mT and 20 mT. The corresponding frequency spectra of the magnetization rotation signals are pooled in figure 7.4. Each spectrum contains two frequency peaks. The spectral line indicated by the dashed red vertical line f_1 remains localized and is centered around $f_1 = 20,5$ GHz. The spectral position of the lower peak f_{M} moves to higher values with increasing $\mu_0 H_{\text{ext}}$. The linear fit of the frequency f_{M} in dependence of $\mu_0 H_{\text{ext}}$ is plotted in figure 7.5 (a) in a range of $100 - 670$ mT. Symbols represent

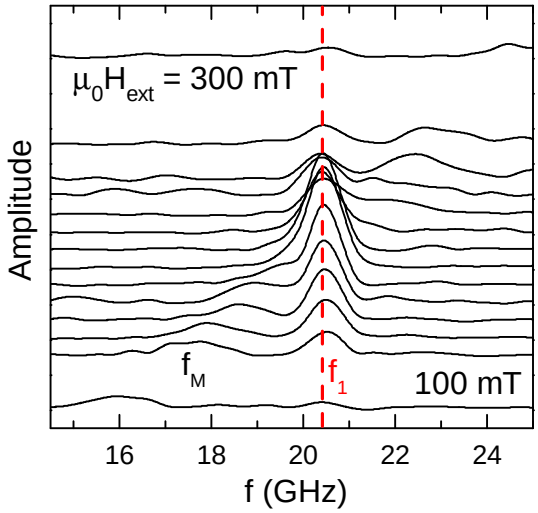

Figure 7.4: (a) Frequency spectra of the corresponding magnetization precession signals $\Delta M_z(t)/M_0$ monitored for various external magnetic fields $\mu_0 H_{\mathrm{ext}}$ ranging from 100 to 300 mT with steps of $10-20$ mT. Each curve displays two frequency peaks - the lower one indicated as f_{M} and a localized mode defined as f_1.

experimental data points whereas the solid curve is the linear fit of the data. Comparing this frequency dependence of f_{M} to the precession frequency spectra obtained in the pure [001]-Galfenol layer (see figure 6.12 (c)) emphasizes that f_{M} corresponds to the magnetization precession frequency in the Galfenol layer deposited on the SL system. Horizontal dashed lines in figure 7.5 (a) indicate the values of the calculated cavity phonon frequencies f_{Ri}. The intersections of f_{Ri} with the frequency curve f_M refer to the corresponding external fields $\mu_0 H_{\mathrm{Ri}}$ at the cavity resonance condition. Figure 7.5 (b) depicts the amplitude of the localized spectral line f_1 dependent on $\mu_0 H_{\mathrm{ext}}$ as symbols. The data is fitted by a Gaussian distribution (dotted curve). The maximum frequency amplitude is observed between 180 and 190 mT. The dashed vertical line indicated the external field $\mu_0 H_{\mathrm{R1}}$ corresponding to the resonance frequency f_{R1}.
Following conclusions can be drawn from the study so far. The magnetization precession induced by picosecond strain pulses is significantly enhanced when the precession frequency coincides with the lowest resonant cavity mode: $f_{\mathrm{M}} \approx f_{\mathrm{R1}}$. The concept of resonant driving of the magnetization dynamics by localized cavity phonons manifests on the one hand in an increased life time of the oscillatory motion of $\Delta M_z(t)/M_0$ (figure 7.3) when the resonance condition $f_{\mathrm{M}} = f_{\mathrm{R1}}$ is fulfilled. On the other hand, the amplitude of the spectral line f_1 associated with the localized cavity mode in the frequency domain reaches a maximum at H_{R1}.

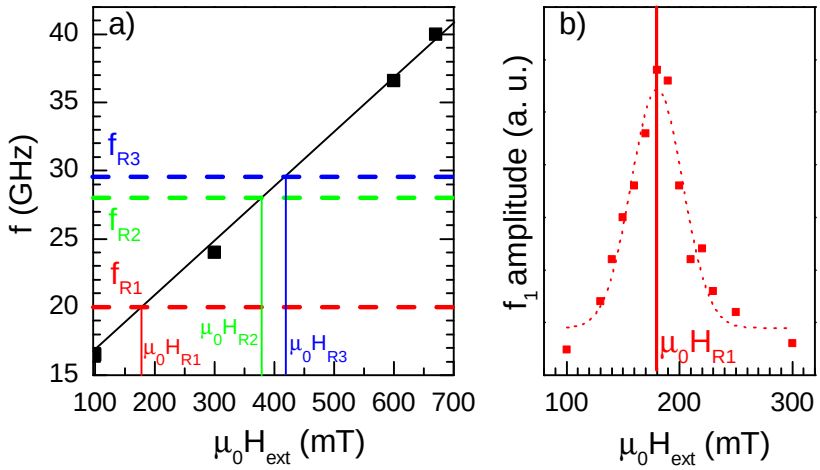

Figure 7.5: (a) Spectral position of the frequency mode f_{M} (symbols) obtained from precession signals $\Delta M_z(t)/M_0$ at external fields up to 670 mT (with solid line as linear fit). Dashed horizontal lines f_{R1}, f_{R2} and f_{R3} indicate the cavity modes of the acoustic resonator with the corresponding fields $\mu_0 H_{\mathrm{Ri}}$ as solid vertical lines. (b) Spectral amplitude dependence of the frequency f_1 on $\mu_0 H_{\mathrm{ext}}$ (symbols) and Gaussian fit of the experimental data points (dotted curve).

These observations of the enhanced magnetization precession in the Galfenol cavity may be explained as follows. The thermal expansion of the Galfenol layer when a femtosecond optical pump pulse is applied to the sample surface leads to the injection of an picosecond strain pulse containing a broad spectrum of acoustic phonons. The broad acoustic wave packet excites free magnetization precession in the Galfenol film. In the single Galfenol film the precessional motion decays within 700 ps [figure 6.10 (a)] [24, 104]. The strain pulse leaves the layer within a time range of ≈ 50 ps. The phonon modes with frequencies corresponding to the stop bands of the SLs $f = f_{\mathrm{Ri}}$ remain localized in the film because the transmission of these modes through the acoustic cavity is suppressed by the mirroring effect of the SLs. The corresponding decay time $\tilde{\tau}_{\mathrm{R1}}$ for the cavity containing SL1 as one Bragg mirror can be calculated to $\tilde{\tau}_{\mathrm{R1}} \approx 10$ ns. Compared to the signal decay times observed from the free magnetization precession in this geometry the lifetime of the localized cavity modes is two orders of magnitude larger. Within this time $\tilde{\tau}_{\mathrm{R1}}$, the localized phonons are assumed to drive the magnetization precession in case that the precession frequency is close to the resonance phonon frequency, $f_M = f_{\mathrm{R1}}$ (or in terms of the corresponding resonance field $H_{\mathrm{ext}} = H_{\mathrm{R1}}$). This resonant driving process related to the resonance condition is clearly observed in figure 7.3 by the enhancement of the decay time of the oscillatory signal tail. As the magnetization precession frequency of the layer linearly depends on the external magnetic field the precession is moved out of resonance

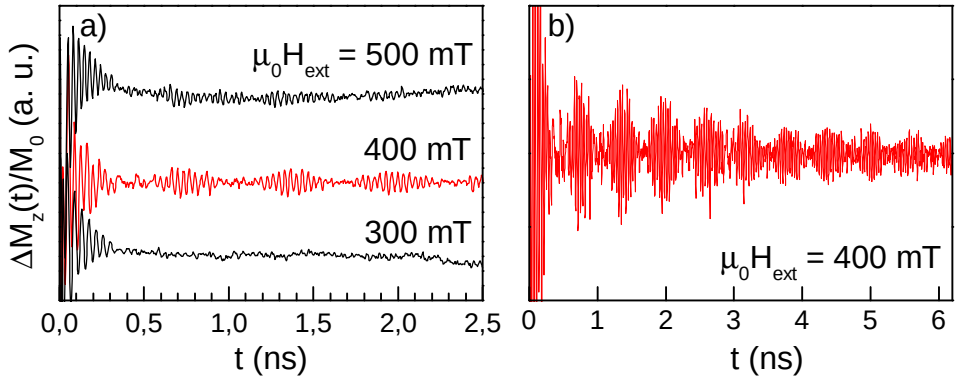

Figure 7.6: (a) Strain induced magnetization precession signals measured at $\mu_0 H_{\text{ext}} = 300, 500$ (black curves) and 400 mT (red curve) are plotted for a time window of $0 \leq t \leq 2,5$ ns. (b) Time evolution of the long-living signal $\Delta M_z(t)/M_0$ at $\mu_0 H_{\text{ext}} = 400$ from plot (a) recorded in a time range up to 6 ns.

when $\mu_0 H_{\text{ext}}$ is set to higher or lower values and $H_{\text{ext}} \neq H_{\text{R1}}$ which can be obtained from extremely shorter decay times of the $\Delta M_z(t)/M_0$ magnetization signals.

From figure 7.5 (a) external magnetic fields H_{R2} and H_{R3} located around 400 mT are indicated from the intersections of the frequency dependence on $\mu_0 H_{\text{ext}}$ and the cavity frequencies f_{R2} and f_{R3}. The acoustic Fabry-Perot resonator limited by the Galfenol/air interface and the SL2 on the opposite side embodies the Galfenol layer and the SL1 structure as the resonator cavity as SL2 is positioned below SL1. Figure 7.6 (a) presents the MOKE signal $\Delta M_z(t)/M_0$ measured at $\mu_0 H_{\text{ext}} = 300$, 400 and 500 mT. The maximum signal amplitude and -duration is recorded at an external field of 400 mT. Figure 7.6 (b) displays the time evolution of $\Delta M_z(t)/M_0$ monitored at 400 mT in an extended time range. The decay time of the long living signal tail reaches 6 ns. Pronounced beatings in the time evolution signal suggest several frequencies in the FFT spectrum. The spectral density is shown for the corresponding precession signals at $\mu_0 H_{\text{ext}} = 300$, 400 and 500 mT in figure 7.7 and displays several peaks with vertical lines indicating the maximum amplitude of the both most pronounced frequency peaks $f_2 = 28,4$ GHz and $f_3 = 30,0$ GHz. These values match the calculated resonance frequencies $f_{\text{R2}} = 28,0$ GHz and $f_{\text{R3}} = 29,5$ GHz corresponding to the cavity limited by the open FeGa surface and the Bragg mirror SL2. The frequency of the spectral lines seems to be independent of H_{ext} whereas the amplitude of f_2 and f_3 is rather low at 300 and 500 mT, yielding a pronounced maximum at 400 mT. This value of the external field fits well to the resonance condition where $H_{\text{ext}} = H_{\text{R2}}, H_{\text{R3}}$ indicated by the intersections of f_{R2} and f_{R3} with the precession frequency curve in figure 7.5 (a) between 370 mT and 420 mT. Thus, driving the

magnetization precession frequency into resonance with the cavity phonon frequencies reveals an immense increase of the precession lifetime and spectral amplitude manifesting the physical concept of the interaction of localized cavity phonons with the magnetization precession of the layer in each SL. The frequency spectrum of the cavity can be confirmed from theoretical modulations and is shown in the inset of figure 7.7 [105, 101]. The main peaks located at 20 GHz and at $28-30$ GHz coincide with the experimental observed spectrum. Both, the experimental and calculated spectra contain additional frequency peaks with lower amplitudes around f_2 and f_3 independent of H_{ext}. These features are attributed to the finite length of the superlattice.

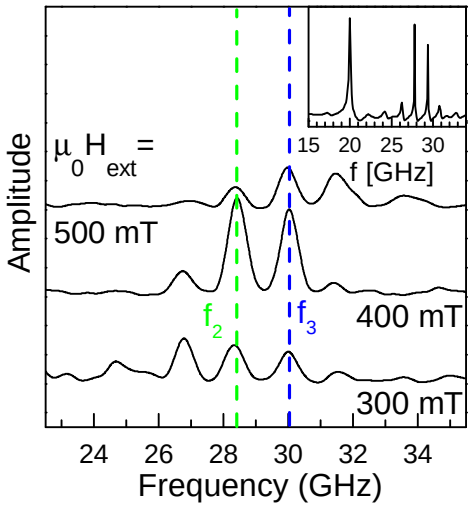

Figure 7.7: Frequency spectra derived from $\Delta M_z(t)/M_0$ signals at 100, 300 and 500 mT. Dashed vertical lines f_2 and f_3 illustrate the maximum frequency amplitudes from the precession measurements. The inset shows the frequency spectrum yielded from theoretical calculations [105, 101].

The resonant driving of magnetization precession by coherent phonons has been shown for frequencies corresponding to localized longitudinal acoustic phonon modes. Resonance effects on f_{M} from frequencies of localized transverse phonon modes are not observed in this structure. The plausible reason is that the optical pump pulse does not excite shear strain corresponding to TA phonons because of the high symmetry conditions of the sample structure [69, 72].

7.4 Conclusion

In this chapter a novel technique to enhance the magnetization modulation of a thin ferromagnetic layer induced by picosecond strain pulses resonantly via coherent phonons in the GHz regime has been introduced. Therefore, a Galfenol layer has been inserted into an acoustic cavity forming a Fabry-Perot resonator with the open surface at one side and two superlattice structures at the opposite side of the Galfenol layer serving as phonon mirrors framing the cavity. Both superlattices consist of alternating stacking of nm layers of GaAs and AlAs. The transmission of acoustic phonons through the resonator, which are generated in the Galfenol film by means of the picosecond acoustics technique, is restricted due to selective frequency filtering governed by SL-characteristic stop bands. Thus, coherent phonons with frequencies that fall into the forbidden gaps remain confined in the acoustic cavity. These phonon modes interact with the magnetization excitation of the frequency f_M matching the stop band frequency. This enables an increase of the magnetization precession lifetime up to 6 ns. The magnetization precession is driven into resonance $f_{\mathrm{M}} = f_{\mathrm{Ri}}$ by scanning through the external magnetic field centered around the resonance condition $H_{\mathrm{ext}} = H_{\mathrm{Ri}}$. The resonant driving of magnetization modulation has experimentally been demonstrated for both SL structures providing different resonance frequencies. Following the challenging technological task of efficient control of magnetic excitation at ultrahigh speed the discussed resonant driving phenomenon utilizing picosecond acoustics opens a new direction outperforming disadvantages of traditional methods in the research field of magnetization resonance phenomena. Further development of the reported experimental approach addresses an ardent topic in ultrafast ferromagnetism: The generation of LA and TA strain pulses from magnetization precession dynamics. Formally, the idea describes the inversion of the reported magnetization modulation experiments based on the Villari effect thus, speaking of a magnetostriction effect. By exciting magnetization in a ferromagnetic layer it is possible to yield magneto-elastic waves from the coupling of magnetic excitation and acoustic phonons as it has been shown for microwave application [106]. In contrast, this method reported here does not require any external resonators, it can be scaled down to the nanometers and thus, it belongs to the important issues in the field of nanomagnetism.

8 Conclusion

In conclusion, the effective modulation of the magnetization induced by picosecond strain pulses in a ferromagnetic nanometer Galfenol layer has been successfully demonstrated. Among the group of recently developed giant magnetostrictive materials Galfenol provides outstanding physical and technical properties making it suitable for ultrafast magnetization control experiments. In this work, this material is combined with the method of picosecond acoustics, a powerful tool to manipulate magnetic properties. The principle of strain induced magnetization modulation is based on the inverse magnetostriction or Villari effect. The equilibrium direction of magnetization oriented along the effective field $\vec{H}_{\text{eff}}$ in a ferromagnetic layer subject to an external magnetic field is governed by the direction and orientation of the applied $\vec{H}_{\text{ext}}$ and the magnetic anisotropy parameters. The picosecond strain pulse generated by femtosecond light pulses couples to the magneto-crystalline anisotropy of the ferromagnetic layer changing the orientation of $\vec{H}_{\text{eff}}$. The magnetization is tilted out of the equilibrium direction and remains precessing around $\vec{H}_{\text{eff}}$.
In preliminary studies discussed in chapter 5 the propagation and detection characteristics of picosecond strain pulses in a low symmetry GaAs substrate has been analyzed. The strain pulse contains qLA and qTA phonons modes segregating in time due to their different sound velocities. The separated detection of qLA and qTA pulses is realized in intensity modulation and polarization rotation measurements [45, 85].
Various magnetization modulation experiments performed in different geometries and sample structures have been presented in chapter 6. The first obervation of strain induced precession signals $\Delta M_z/M_0$ monitored by means of the polar MOKE has been realized in high symmetry [001]-Galfenol samples at cryogenic temperatures. Precession decay times up to 3 ns and precession frequencies in the GHz range are in very good agreement with results from ferromagnetic-resonance experiments in Galfenol. This first part demonstrates the efficient conversion of picosecond strain into magnetization control in Galfenol. Moreover, the detection of several spin wave modes in the frequency domain of the $\Delta M_z(t)/M_0$ signals has opened the way for future detailed investigation in this direction. The excitation of a single spin wave mode at a specific frequency may find application in spin current control in spintronic devices, for example [107]. Common techniques such as the microwave excitation of single spin waves are limited to ns timescales and sub-micrometer dimensions [108]. The experiments reported in this work show that these issues may be improved by ultrafast magnetization manipulation in Galfenol structures scaled down to nanome-

ter sizes.
Extending the experiment to qTA strain pulses by the use of a high index [311]-Galfenol structure reveals higher magnetization precession amplitudes at values assuming to reach 2 % of the saturation magnetization for the in-plane magnetization component. This relates to 40 mT which is higher than tilting amplitudes reported so far from similar experiments [22, 23]. The highest precession frequencies reach 40 GHz for magnetization signals induced by qTA strain pulses at in-plane orientation of the external magnetic field. It has been shown that the precession amplitude induced by qTA pulses is only limited by technical issues as the applied laser power. Overcoming technical limitations may lead to the ultrafast complete switching of magnetic states required in spin logic devices for example. Due to the high Curie temperature of Galfenol, magnetization dynamics have also been investigated at ambient temperatures. The observed results are very similar to the previous findings at cryogenic temperatures.
The magnetization modulation in Galfenol is significantly enhanced, by inserting the ferromagnetic layer into a an acoustic Fabry-Perot resonator. This experimental study has been the topic of chapter 7. A Galfenol layer is deposited on a system of two superlattices serving as acoustic Bragg mirrors. The second mirror is given by the open Galfenol surface. Phonons with frequencies corresponding to the superlattice stop bands are confined in the acoustic cavity. Tuning the magnetization precession frequency by the external field into resonance with the localized cavity modes reveals high amplitude precession signals with enormously increased decay times up to 6 ns. This resonant driving phenomenon may supersede traditional methods of microwave radiation [93, 94]. Since the optical generation of coherent monochromatic phonons may be extended to THz frequencies [109] the resonant driving of magnetization displaying resonances at higher frequencies for example in antiferromagnetic structures may be realized.

9 Bibliography

[1] D.A. Porter, M.A. Smith, Journal of Biomedical Engineering **10**, 562 (1988).

[2] M. Pasquale, Sensors and Actuators A: Physical **106**, 142 (2003), proceedings of the 4th European Magnetic Sensors and Actuators Conference.

[3] I. Karaman, B. Basaran, H. E. Karaca, A. I. Karsilayan, Y. I. Chumlyakov, Applied Physics Letters **90**, 172505 (2007).

[4] R. A. Kellogg, *Dissertation: Development and modeling of iron-gallium alloys* (Iowa State University, Iowa, 2003).

[5] J. Atulasimha, *Dissertation: Characterization and modeling of the magnetomechanical behaviour of iron-gallium alloys* (University of Maryland, Maryland, 2006).

[6] B. Bhattacharya, *Terfenol and galfenol: Smart magnetostrictive met- als for intelligent transduction* (Technical report, Indian Institute of Technology Kanpur, India, 2005).

[7] E. Clark, *Ferromagnetic Materials, A handbook on the properties of magnetically ordered substances* (North Holland, 1980).

[8] Y. Hashimoto, S. Kobayashi, H. Munekata, Phys. Rev. Lett. **100**, 067202 (2008).

[9] J. Qi, Y. Xu, N. H. Tolk, X. Liu, J. K. Furdyna, I. E. Perakis, Applied Physics Letters **91**, 112506 (2007).

[10] E. Rozkotová, P. Nemec, P. Horodyská, D. Sprinzl, F. Trojánek, P. Malý, V. Novak, K. Olejnik, M. Cukr, T. Jungwirth, Applied Physics Letters **92**, 122507 (2008).

[11] G. V. Astakhov, A. V. Kimel, G. M. Schott, A. A. Tsvetkov, A. Kirilyuk, D. R. Yakovlev, G. Karczewski, W. Ossau, G. Schmidt, L. W. Molenkamp, Th. Rasing, Applied Physics Letters **86**, 152506 (2005).

[12] E. Beaurepaire, J.-C. Merle, A. Daunois, J.-Y. Bigot, Phys. Rev. Lett. **76**, 4250 (1996).

[13] P. Balestriere, T. Devolder, J. Wunderlich, C. Chappert, Applied Physics Letters **96**, 142504 (2010).

[14] C. Thomsen, J. Strait, Z. Vardeny, H. J. Maris, J. Tauc, J. J. Hauser, Phys. Rev. Lett. **53**, 989 (1984).

[15] C. Thomsen, H.J. Maris, J. Tauc, Thin Solid Films **154**, 217 (1987).

[16] L. J. Shelton, F. Yang, W. K. Ford, H. J. Maris, physica status solidi (b) **242**, 1379 (2005).

[17] A. S. Salasyuk, A. V. Scherbakov, D. R. Yakovlev, A. V. Akimov, A. A. Kaplyanskii, S. F. Kaplan, S. A. Grudinkin, A. V. Nashchekin, A. B. Pevtsov, V. G. Golubev, T. Berstermann, C. Brüggemann, M. Bombeck, M. Bayer, Nano Letters **10**, 1319 (2010).

[18] C. Brüggemann, A. V. Akimov, A. V. Scherbakov, M. Bombeck, C. Schneider, S. Hofling, A. Forchel, D. R. Yakovlev, M. Bayer, Nature Photonics **6**, 30 (2012).

[19] T. Czerniuk, C. Brüggemann, J. Tepper, S. Brodbeck, C. Schneider, M. Kamp, S. Höfling, B. A. Glavin, D. R. Yakovlev, A. V. Akimov, M. Bayer, Nature Communications **5** (2014).

[20] C. Brüggemann, A. V. Akimov, B. A. Glavin, V. I. Belotelov, I. A. Akimov, J. Jäger, S. Kasture, A. V. Gopal, A. S. Vengurlekar, D. R. Yakovlev, A. J. Kent, M. Bayer, Phys. Rev. B **86**, 121401 (2012).

[21] A. V. Scherbakov, P. J. S. van Capel, A. V. Akimov, J. I. Dijkhuis, D. R. Yakovlev, T. Berstermann, M. Bayer, Phys. Rev. Lett. **99**, 057402 (2007).

[22] A. V. Scherbakov, A. S. Salasyuk, A. V. A ov, X. Liu, M. Bombeck, C. Brüggemann, D. R. Yakovlev, V. F. Sapega, J. K. Furdyna, M. Bayer, Phys. Rev. Lett. **105**, 117204 (2010).

[23] M. Bombeck, J. V. Jäger, A. V. Scherbakov, T. Linnik, D. R. Yakovlev, X. Liu, J. K. Furdyna, A. V. Akimov, M. Bayer, Phys. Rev. B **87**, 060302 (2013).

[24] Ji-Wan Kim, Mircea Vomir, Jean-Yves Bigot, Phys. Rev. Lett. **109**, 166601 (2012).

[25] Yanning Zhang, Ruqian Wu, Magnetics, IEEE Transactions on **47**, 4044 (2011).

[26] M. Farle, Reports on Progress in Physics **61**, 755 (1998).

[27] K. Honda, S. Kaya, Sci. Rep. Tohoku Univ. **15**, 721 (1926).

[28] E. C. Stoner, E. P. Wohlfarth, Philosophical Transactions of the Royal Society of London A: Mathematical, Physical and Engineering Sciences **240**, 599 (1948).

[29] T. L. Linnik, A. V. Scherbakov, D. R. Yakovlev, X. Liu, J. K. Furdyna, M. Bayer, Phys. Rev. B **84**, 214432 (2011).

[30] B. D. Cullity, *Introduction to magneitc materials* (Addison Wesley Pub., 1972).

[31] Sadia Rafique, James R. Cullen, Manfred Wuttig, Jun Cui, Journal of Applied Physics **95** (2004).

[32] J. V. Jäger, A. V. Scherbakov, T. L. Linnik, D. R. Yakovlev, M. Wang, P. Wadley, V. Holy, S. A. Cavill, A. V. Akimov, A. W. Rushforth, M. Bayer, Applied Physics Letters **103**, 032409 (2013).

[33] Xinyu Liu, Jacek K Furdyna, Journal of Physics: Condensed Matter **18**, R245 (2006).

[34] Charles Kittel, Rev. Mod. Phys. **21**, 541 (1949).

[35] A.E. Clark, M. Wun-Fogle, J.B. Restorff, T.A. Lograsso, James R. Cullen, IEEE Transactions on Magnetics **37**, 2678 (2001).

[36] Eiji Tatsumoto, Tetsuhiko Okamoto, Journal of the Physical Society of Japan **14**, 1588 (1959).

[37] H. Wang, Y. N. Zhang, R. Q. Wu, L. Z. Sun, D. S Xu, Z. D. Zhang, Scientific Reports **3**, 448 (2013).

[38] B. P. Yan, C. M. Zhang, L. Y. Li, Z.F. Tang, F. Z. Lü, Yang K. J., Chinese Physics B **23**, 127504 (2014).

[39] F. T. Calkins, A. B. Flatau, *Terfenol-D Sensor Design and Optimization*, vol. 14 (1997).

[40] A. E. Clark, M. Wun-Fogle, J. B. Restorff, T. A. Lograsso, Materials Transactions **43**, 881 (2002).

[41] E.M. Summers, T.A. Lograsso, M. Wun-Fogle, Journal of Materials Science **42**, 9582 (2007).

[42] H. Cao, P. M. Gehring, C. P. Devreugd, J. A. Rodriguez-Rivera, J. Li, D. Viehland, Phys. Rev. Lett. **102**, 127201 (2009).

[43] Eric M. Summers, Thomas A. Lograsso, Jonathan D. Snodgrass, Julie C. Slaughter, Proc. SPIE **5387**, 448 (2004).

[44] A.Y. Cho, J.R. Arthur, Progress in Solid State Chemistry **10, Part 3**, 157 (1975).

[45] D. E. Parkes, L. R. Shelford, P. Wadley, V. Holý, M. Wang, A. T. Hindmarch, G. van der Laan, R. P. Campion, K. W. Edmonds, S. A. Cavill, A. W. Rushforth, Scientific Reports **3**, 6939 (2013).

[46] T.A. Lograsso, E.M. Summers, Materials Science and Engineering: A **416**, 240 (2006).

[47] D. E. Parkes, S. A. Cavill, A. T. Hindmarch, P. Wadley, F. McGee, C. R. Staddon, K. W. Edmonds, R. P. Campion, B. L. Gallagher, A. W. Rushforth, Applied Physics Letters **101**, 072402 (2012).

[48] S. A. Cavill, D. E. Parkes, J. Miguel, S. S. Dhesi, K. W. Edmonds, R. P. Campion, A. W. Rushforth, Applied Physics Letters **102**, 032405 (2013).

[49] C. Thomsen, H. T. Grahn, H. J. Maris, J. Tauc, Phys. Rev. B **34**, 4129 (1986).

[50] O. Yu. Belyaeva, N. Karpachev, L. K. Zarembo, Soviet Physics Uspekhi **35**, 106 (1992).

[51] B. A. Auld, *Acoustic fields and waves in solids* (R. E. Krieger, 1990).

[52] G. Czycholl, *Theoretische Festkörperphysik* (Springer, 2007).

[53] T. Saito, O. Matsuda, O. B. Wright, Phys. Rev. B **67**, 205421 (2003).

[54] O. B. Wright, Phys. Rev. B **49**, 9985 (1994).

[55] Guray Tas, Humphrey J. Maris, Phys. Rev. B **49**, 15046 (1994).

[56] A V Akimov, A V Scherbakov, P J S van Capel, J I Dijkhuis, T Berstermann, D R Yakovlev, M Bayer, Journal of Physics: Conference Series **92**, 012002 (2007).

[57] H.-Y. Hao, H. J. Maris, Phys. Rev. B **64**, 064302 (2001).

[58] Otto L. Muskens, Jaap I. Dijkhuis, Phys. Rev. Lett. **89**, 285504 (2002).

[59] B. C. Daly, T. B. Norris, J. Chen, J. B. Khurgin, Phys. Rev. B **70**, 214307 (2004).

[60] M. Overby, A. Chernyshov, L. P. Rokhinson, X. Liu, J. K. Furdyna, Applied Physics Letters **92**, 192501 (2008).

[61] A. W. Rushforth, E. De Ranieri, J. Zemen, J. Wunderlich, K. W. Edmonds, C. S. King, E. Ahmad, R. P. Campion, C. T. Foxon, B. L. Gallagher, K. Výborný, J. Kucera, T. Jungwirth, Phys. Rev. B **78**, 085314 (2008).

[62] C. Bihler, M. Althammer, A. Brandlmaier, S. Geprägs, M. Weiler, M. Opel, W. Schoch, W. Limmer, R. Gross, M. S. Brandt, S. T. B. Goennenwein, Phys. Rev. B **78**, 045203 (2008).

[63] S. Chung, H. C. Kim, S. Lee, X Liu, J. K. Furdyna, Solid State Communications **149**, 1739 (2009).

[64] E. M. Lifshitz, L.P. Pitaevski, *Statistical Physics* (Pergamon, London, 1980).

[65] C. Kittel, *Einführung in die Festkörperphysik* (Oldenbourg, 2006).

[66] R. Hubert, A. Schäfer, *Magnetic Domains - The Analysis of Magnetic Microstructures* (Springer, 2000).

[67] J. Zak, E.R. Moog, C. Liu, S.D. Bader, Journal of Magnetism and Magnetic Materials **89**, 107 (1990).

[68] G. H. O. Daalderop, F. M. Mueller, R. C. Albers, A. M. Boring, Applied Physics Letters **52**, 1636 (1988).

[69] T. Pezeril, P. Ruello, S. Gougeon, N. Chigarev, D. Mounier, J.-M. Breteau, P. Picart, V. Gusev, Phys. Rev. B **75**, 174307 (2007).

[70] O. B. Wright, Journal of Applied Physics **71** (1992).

[71] H. N. Lin, R. J. Stoner, H. J. Maris, J. Tauc, Journal of Applied Physics **69** (1991).

[72] O. Matsuda, O. B. Wright, D. H. Hurley, V. Gusev, K. Shimizu, Phys. Rev. B **77**, 224110 (2008).

[73] X Liu, J K Furdyna, M Dobrowolska, W L Lim, C Xie, Y J Cho, Journal of Physics: Condensed Matter **19**, 165205 (2007).

[74] P. Babilotte, P. Ruello, D. Mounier, T. Pezeril, G. Vaudel, M. Edely, J-M. Breteau, V. Gusev, K. Blary, Phys. Rev. B **81**, 245207 (2010).

[75] A. V. Scherbakov, M. Bombeck, J. V. Jäger, A. S. Salasyuk, T. L. Linnik, V. E. Gusev, D. R. Yakovlev, A. V. Akimov, M. Bayer, Opt. Express **21**, 16473 (2013).

[76] A. V. Akimov, A. V. Scherbakov, D. R. Yakovlev, C. T. Foxon, M. Bayer, Phys. Rev. Lett. **97**, 037401 (2006).

[77] Z. V. Popovic, J. Spitzer, T. Ruf, M. Cardona, R. Nötzel, K. Ploog, Phys. Rev. B **48**, 1659 (1993).

[78] Thomas Dehoux, Nikolay Chigarev, Clément Rossignol, Bertrand Audoin, Phys. Rev. B **76**, 024311 (2007).

[79] J. F. Nye, *Physical Properties of Crystals: Their Representation by Tensors and Matrices* (Oxford Science Publications, 1985).

[80] S. Adachi, Journal of Applied Physics **58** (1985).

[81] M. Zoelfl, M. Brockmann, M. Koehler, S. Kreuzer, T. Schweinboeck, S. Miethaner, F. Bensch, G. Bayreuther, Journal of Magnetism and Magnetic Materials **175**, 16 (1997), proceedings of the First Toyota Workshop on Magnetism and Magnetic Materials for High Density Information Storage.

[82] E. M. Kneedler, B. T. Jonker, P. M. Thibado, R. J. Wagner, B. V. Shanabrook, L. J. Whitman, Phys. Rev. B **56**, 8163 (1997).

[83] P.K. Muduli, J. Herfort, H.-P. Schönherr, L. Däweritz, K.H. Ploog, Applied Physics A **81**, 901 (2005).

[84] O. Wright, K. Kawashima, Phys. Rev. Lett. **69**, 1668 (1992).

[85] Bijoy K. Kuanr, R. E. Camley, Z. Celinski, Adam McClure, Yves Idzerda, Journal of Applied Physics **115**, 17 (2014).

[86] B. Perrin, E. Péronne, L. Belliard, Ultrasonics **44, Supplement**, 1277 (2006), proceedings of Ultrasonics International (UI 05) and World Congress on Ultrasonics (WCU).

[87] M. Bombeck, A. S. Salasyuk, B. A. Glavin, A. V. Scherbakov, C. Brüggemann, D. R. Yakovlev, V. F. Sapega, X. Liu, J. K. Furdyna, A. V. Akimov, M. Bayer, Phys. Rev. B **85**, 195324 (2012).

[88] C. Vittoria, *Microwave Properties of Magnetic Films* (World Scientific, Singapore, 1993).

[89] Wei Chen, Humphrey J. Maris, Zbigniew R. Wasilewski, Shin-Ichiro Tamura, Philosophical Magazine Part B **70**, 687 (1994).

[90] Peter Hess, Alexey M. Lomonosov, Ultrasonics **50**, 167 (2010), selected Papers from ICU 2009.

[91] Paul Glover, Sir Peter Mansfield, Reports on Progress in Physics **65**, 1489 (2002).

[92] L. M. K. Vandersypen, M. Steffen, G. Breyta, C. S. Yannoni, M. H. Sherwood, I. L. Chuang, Nature **414**, 883 (2001).

[93] J. R. Maze, P. L. Stanwix, J. S. Hodges, S. Hong, J. M. Taylor, P. Cappellaro, L. Jiang, M. V. G. Dutt, E. Togan, A. S. Zibrov, A. Yacoby, R. L. Walsworth, M. D. Lukin, Nature **455**, 644 (2008).

[94] Georg Woltersdorf, Christian H. Back, Phys. Rev. Lett. **99**, 227207 (2007).

[95] L. Brillouin, *Wave Propagation in Periodic Structures* (McQraw Hill, New York, 1946).

[96] V. Narayanamurti, H. L. Störmer, M. A. Chin, A. C. Gossard, W. Wiegmann, Phys. Rev. Lett. **43**, 2012 (1979).

[97] S. Tamura, D. C. Hurley, J. P. Wolfe, Phys. Rev. B **38**, 1427 (1988).

[98] C. Colvard, R. Merlin, M. V. Klein, A. C. Gossard, Phys. Rev. Lett. **45**, 298 (1980).

[99] T. Gorishnyy, C. K. Ullal, M. Maldovan, G. Fytas, E. L. Thomas, Phys. Rev. Lett. **94**, 115501 (2005).

[100] Wei Chen, Yu Lu, Humphrey J. Maris, Gang Xiao, Phys. Rev. B **50**, 14506 (1994).

[101] Seiji Mizuno, Shin-Ichiro Tamura, Phys. Rev. B **45**, 734 (1992).

[102] M S Skolnick, T A Fisher, D M Whittaker, Semiconductor Science and Technology **13**, 645 (1998).

[103] N D Lanzillotti-Kimura, A Fainstein, A Huynh, B Perrin, B Jusserand, A Miard, A Lemaître, Journal of Physics: Conference Series **92**, 012016 (2007).

[104] H. B. Zhao, D. Talbayev, Q. G. Yang, G. Lüpke, A. T. Hanbicki, C. H. Li, O. M. J. van't Erve, G. Kioseoglou, B. T. Jonker, Applied Physics Letters **86**, 152512 (2005).

[105] J. V. Jäger, A. V. Scherbakov, B. A. Glavin, A. S. Salasyuk, R. P. Campion, A. W. Rushforth, D. R. Yakovlev, A. V. Akimov, M. Bayer, to be published .

[106] J. W. Tucker, V. W. Rampton, *Microwave Ultrasonics in Solid State Physics* (North-Holland, 1972).

[107] V. E. Demidov, S. Urazhdin, H. Ulrichs, V. Tiberkevich, A. Slavin, D. Baither, G. Schmitz, S. O. Demokritov, Nature Materials **11**, 1028 (2012).

[108] X. Liu, Y. Y. Zhou, J. K. Furdyna, Phys. Rev. B **75**, 195220 (2007).

[109] A. Huynh, B. Perrin, A. Lemaître, Ultrasonics **56**, 66 (2015).

10 List of publications

"Resonant driving of magnetization precession in a ferromagnetic layer by coherent monochromatic phonons"
J. V. Jäger, A. V. Scherbakov, B. A. Glavin, A. S. Salasyuk, R. P. Campion, A. W. Rushforth, D. R. Yakovlev, A. V. Akimov, and M. Bayer, *to be published* (2015)

"Hypersonic properties of monodisperse spherical mesoporous silica particles"
D. A. Eurov, D. A. Kurdyukov, E. Yu. Stovpiaga, A. S. Salasyuk, **J. V. Jäger**, A. V. Scherbakov, A. V. Akimov, A. J. Kent, D. R. Yakovlev, M. Bayer, and V. G. Golubev, *Journal of Physics D: Applied Physics* **47**, 335303 (2014)

"Picosecond inverse magnetostriction in galfenol thin films"
J. V. Jäger, A. V. Scherbakov, T. L. Linnik, D. R. Yakovlev, M. Wang, P. Wadley, V. Holy, S. A. Cavill, A. V. Akimov, A. W. Rushforth, and M. Bayer, *Applied Physics Letters* **103**, 032409 (2013)

"Magnetization precession induced by quasitransverse picosecond strain pulses in (311) ferromagnetic (Ga,Mn)As"
M. Bombeck, **J. V. Jäger**, A. V. Scherbakov, T. Linnik, D. R. Yakovlev, X. Liu, J. K. Furdyna, A. V. Akimov, and M. Bayer, *Phys. Rev. B* **87**, 060302 (2013)

"Picosecond opto-acoustic interferometry and polarimetry in high-index GaAs"
A. V. Scherbakov, M. Bombeck, **J. V. Jäger**, A. S. Salasyuk, T. L. Linnik, V. E. Gusev, D. R. Yakovlev, A. V. Akimov, and M. Bayer, *Opt. Express* **21**, 16473 (2013)

"Studying periodic nanostructures by probing the in-sample optical far-field using coherent phonons"
C. Brüggemann, **J. V. Jäger**, B. A. Glavin, V. I. Belotelov, I. A. Akimov, S. Kasture, A. V. Gopal, A. S. Vengurlekar, D. R. Yakovlev, A. V. Akimov, and M. Bayer, *Applied Physics Letters*, **101**, 243117 (2012)

"Modulation of a surface plasmon-polariton resonance by subterahertz diffracted coherent phonons"
C. Brüggemann, A. V. Akimov, B. A. Glavin, V. I. Belotelov, I. A. Akimov, **J. V. Jäger**, S. Kasture, A. V. Gopal, A. S. Vengurlekar, D. R. Yakovlev, A. J. Kent, and M. Bayer, *Phys. Rev. B* **86**, 121401 (2012)

11 Acknowledgments

First and foremost I would like to thank Prof. Dr. Manfred Bayer for the opportunity to perform these studies and for his excellent supervision and guidance. I am also greatly thankful to Dr. Alexey Scherbakov for his outstanding support and assistance during the experimental research and paper works. Moreover, I would like to thank Prof. Dr. Andrey Akimov for his supervision and support in both, experimental and theoretical issues.
My sincere thanks also goes to Michaela Wäscher for her excellent administrative work and for all the encouragement, especially during the final phase of these studies. I would like to acknowledge Lars Wieschollek and Klaus Wiegers for their great help in technical lab issues.
Dr. Jörg Debus, Dr. Johannes Schmutzler, Dr. Michael Bombeck and Thomas Czerniuk deserve a special Thank You for proof-reading this work. Last but not least, I would like to thank all E2-members for a great working atmosphere.